UNIVERSITY OF CALIFORNIA
Los Angeles

Insights into Exoplanetary Rock Compositions from Polluted White Dwarfs

A dissertation submitted in partial satisfaction
of the requirements for the degree
Doctor of Philosophy in Astronomy and Astrophysics

by

Isabella Trierweiler

2024

ABSTRACT OF THE DISSERTATION

Insights into Exoplanetary Rock Compositions from Polluted White Dwarfs

by

Isabella Trierweiler
Doctor of Philosophy in Astronomy and Astrophysics
University of California, Los Angeles, 2024
Professor Edward Donald Young, Co-Chair
Professor Bradley M. Hansen, Co-Chair

Polluted white dwarfs offer the rare chance to directly measure the bulk compositions of exoplanetary material. These stellar remnants are actively accreting exoplanetary debris, whose chemical abundances can be extrapolated from excess metal lines in white dwarf spectra. In this dissertation I leverage the growing sample of observed polluted white dwarfs to conduct statistical comparisons between exoplanetary rock compositions and objects in our solar system. My work combines data compiled from the literature along with analytical models for accretion and settling in white dwarf atmospheres to test the elemental abundances of white dwarf pollution, while placing constraints on how to best leverage white dwarf data given uncertainties in different accretion processes. I first validate exomoons as a potential source of white dwarf pollution, and show that the bulk objects causing pollution need to be massive, on the order of Vesta or Ceres, the largest objects in our asteroid belt. I then argue that the white dwarf sample is evidence that most nearby exoplanets form from compositional building blocks similar to CI chondrites, the assumed primitive material in our own solar system. I support this conclusion by showing that the relative abundances of rock-forming

elements in nearby stars are similarly consistent with chondrites, and demonstrate that on very large scales, the chemical evolution of our galaxy may be encoded in planet compositions. Finally, I show that the oxygen abundances in polluted white dwarfs are consistent with water contents ranging from dry, Earth-like bodies to water-rich objects akin to icy moons in the solar system. These results place important constraints on the compositions of exoplanets, suggest that solar system compositions are not unique compared to our nearest neighbors, and provide the foundation for future studies on the formation and diversity of exoplanets in the Milky Way.

The dissertation of Isabella Trierweiler is approved.

Carl Melis

Smadar Naoz

Hilke Elisabet Schlichting

Bradley M. Hansen, Committee Co-Chair

Edward Donald Young, Committee Co-Chair

University of California, Los Angeles

2024

To the students and teachers braving the fight for a better world

TABLE OF CONTENTS

LIST OF FIGURES

LIST OF TABLES

ACKNOWLEDGMENTS

I am forever grateful to my advisor, Edward Young, for his mentorship over the past several years. His enthusiasm and depth of knowledge in so many topics made it a joy to work on this research and I am extremely thankful that I had the opportunity to work in such a friendly and interdisciplinary research group.

I would also like to thank all of the individuals who helped make this work possible:

The other members of my thesis committee: Hilke Schlichting for guiding me through the first few years of grad school. Carl Melis, who taught me all about white dwarf observations. Smadar Naoz and Brad Hansen, whose feedback and career advice I have really appreciated over the years, and whose courses set the foundations for so many of my research skills.

My research group: My fantastic office-mates Lauren Tafla and Sarah Marcum, who made it so much fun to come to work every day. Allie Doyle, who provided lots of helpful advice when I was first getting started in white dwarfs, and whose research paved the way for much of this thesis. Beth Klein and Ben Zuckerman, who welcomed me into their research group and provided mentorship and many valuable discussions on white dwarfs.

The Astronomy and EPSS graduate students; completing graduate school over the course of a pandemic and two strikes was not easy, and I always appreciated having such a fun and welcoming environment to come back to. And special thanks to my cohort, Rory Bentley, Evan Jones, Briley Lewis, and Mason MacDougall, for going through it all with me.

The Astrobites collaboration, for providing a supportive community of graduate students and for teaching me to be a better science writer and communicator.

My undergraduate advisors: Yuanyuan Su and Greg Laughlin, who helped me become a better researcher and prepared me for graduate school, and especially Louise Edwards, who

was my very first astronomy professor and who continues to inspire me to this day.

And last, but not least, my family and friends: My parents, for encouraging my interest in astronomy. Anja, for cheering me on and supporting my emotional well-being with plenty of cat videos. Muffin and Pippi for eternal moral support. Dylan Young, Yerin Kim, Hannah Yang, Luke Emmoth, and Irene Jiang for all the adventuring and shenanigans. Gabrielle Roberts, Sarah Schlick, Nasim Mirzajani, Nealie Ngo, and the rest of the “glom", my found family whose friendship I will always treasure. And of course Pratik Gandhi, my better half who has been with me every step of the way.

This work was made possible by the generous support of Dr. Martha Jura through the Michael A. Jura Memorial Fellowship, and by the NASA FINESST fellowship. I acknowledge that results presented in this thesis are based on published works with additional coauthors. Chapter 2 is a version of Trierweiler et al. (2022), chapter 3 is a version of Trierweiler et al. (2023), and chapter 5 is a version of Trierweiler & Schlichting (2022). Chapter 4 is a version of a paper in preparation for publication with additional coauthors.

VITA

2014–2018 B.S., Astronomy & Astrophysics, Department of Astronomy
Yale University

2018–2020 M.S., Astronomy & Astrophysics, Department of Physics & Astronomy
University of California, Los Angeles

PUBLICATIONS

Trierweiler, I. L., Doyle, A. E., and Young, E. D. (2023), A Chondritic Solar Neighborhood, The Planetary Science Journal, 4, 136

Doyle, A. E., Klein, B. L., Dufour, P., Melis, C., Zuckerman, B., Xu, S., Weinberger, A. J., Trierweiler, I. L., Monson, N. N., Jura, M. A., and Young, E. D. (2023), New Chondritic Bodies Identified in Eight Oxygen-bearing White Dwarfs, The Astrophysical Journal, 950, 93.

Trierweiler, I. L., Doyle, A. E., Melis, C., Walsh, K. J., and Young, E. D. (2022), Exomoons as Sources of White Dwarf Pollution, The Astrophysical Journal, 936, 30.

Trierweiler, I. L., and Schlichting, H. E. (2022), Atmosphere loss by aerial bursts, Monthly Notices of the Royal Astronomical Society, 514, 3650.

Sarkar, A., Su, Y., Randall, S., Gastaldello, F., Trierweiler, I. L., White, R., Kraft, R., and Miller, E. (2021), Joint Suzaku and Chandra observations of the MKW4 galaxy group out

to the virial radius, Monthly Notices of the Royal Astronomical Society, 501, 3767.

Edwards, L. O. V., Salinas, M., Stanley, S., Holguin West, P. E., Trierweiler, I. L., Alpert, H., Coelho, P., Koppaka, S., Tremblay, G. R., Martel, H., and Li, Y. (2020), Clocking the formation of today's largest galaxies: wide field integral spectroscopy of brightest cluster galaxies and their surroundings, Monthly Notices of the Royal Astronomical Society, 491, 2617.

Edwards, L. O. V., Alpert, H. S., Trierweiler, I. L., Abraham, T., and Beizer, V. G. (2016), Stellar populations of BCGs, close companions and intracluster light in Abell 85, Abell 2457 and IIZw108, Monthly Notices of the Royal Astronomical Society, 461, 230.

CHAPTER 1

Introduction

Characterizing the bulk compositions of exoplanetary material is crucial to building an accurate theory of planet formation, understanding the prevalence of rocky exoplanets, and making comparisons to Earth-like geology. As the end results of the post-main sequence evolution of planetary systems, white dwarf (WD) systems are crucial for studying the formation and evolution of exoplanets, with detailed views of planets and minor bodies that are not accessible in main sequences studies. WDs are the end states of medium-mass stars ($\lesssim 8M_{\odot}$), and nearly all detected exoplanet systems have host stars that will eventually evolve into WDs. These remnants have strong gravity, causing rapid sinking of elements heavier than H or He, which should generally leave the spectra of WDs devoid of metal features. Nevertheless, over a thousand WDs have been observed to be 'polluted' with heavy elements (Coutu et al., 2019), with estimates that up to half of all WDs are polluted (Koester et al., 2014). The observed pollution is due to the accretion of exoplanetary material, and depending on the type of WD, material can stay in the stellar atmosphere for days to years before sinking out of sight (Koester, 2009). Because WDs allow us direct access to bulk compositions, polluted WDs provide an important insight into the building blocks of exoplanet compositions, in the same way that meteorite samples record the history of the solar system and formation of the terrestrial planets (e.g., Dauphas, 2017; Young et al., 2023).

The material polluting WDs is believed to be remnants of planetary systems that remained stable throughout the star's main sequence lifetime (Jura et al., 2009), but were perturbed

during the star's post-main sequence evolution and mass loss, and were eventually tidally disrupted and accreted by the WD (Debes & Sigurdsson, 2002; Jura, 2003). This picture of WD pollution is supported by observations of major and minor planets around WDs in various stages of decay (Vanderburg et al., 2015; Gänsicke et al., 2019), along with a variety of gas and dust disk structures (Manser et al., 2016).

To date, over a thousand polluted WDs have been observed, and a few dozen have spectroscopic measurements for the multiple rock-forming elements needed to carry out geochemical studies. The vast majority of the bodies polluting WDs are rocky (Doyle et al., 2020) while a few appear icy (Farihi et al., 2013; Hoskin et al., 2020), and it is typically assumed that the parents bodies are asteroid belt or Kuiper belt analogs, with potential inclusion of exomoons (Payne et al., 2017; Klein et al., 2021; Doyle et al., 2021). Numerical simulations support these various scenarios and have show that long-term perturbations between a large variety of planet and polluter masses can provide a steady stream of debris over billion-year timescales (e.g., Mustill et al., 2018; O'Connor et al., 2022; Veras & Rosengren, 2023).

Using the relative abundances of elements recovered from polluted WD spectra, studies have proposed a range of compositions for exoplanetary material, including bulk Earth analogs, core or crust-only fragments, and entirely new rock types (e.g., Jura & Young, 2014; Melis & Dufour, 2017; Hollands et al., 2018; Harrison et al., 2018; Doyle et al., 2019; Putirka & Xu, 2021; Putirka & Rarick, 2019). The goal of this thesis is to take a more statistical approach to studying polluted WDs, and to use samples of highly polluted WDs to test variations in exoplanetary rock compositions on a larger scale.

This thesis is comprised of four projects. Chapters 2, 3, and 5 are from published papers (Trierweiler et al. 2022, 2023; Trierweiler & Schlichting 2022, respectively), and the work in Chapter 4 is in prep. A summary of each chapter is as follows. I describe future research plans inspired by these works in Chapter 6.

In Chapter 2 I test the probability of exomoon accretion on WDs. This study is motivated by the discovery of beryllium in two WDs, which was attributed to the accretion of a moon, since Be in such high quantities is most likely due to spallation on icy bodies forming within the magnetic field of giant planets. To assess whether moons are a likely contributor to WD pollution, I first used an exponential model for the accretion and settling of material within a WD atmosphere to show that most highly-polluted WDs require massive parent bodies to explain current pollution levels, with most inferred parent bodies being about the mass of Ceres or Vesta. I then ran N-body simulations to estimate rates of moon accretion onto WDs, and applied the accretion and settling model to compare the likelihood of observing the accretion of a single massive object, like a moon, versus the long-term accretion of debris belts, the more commonly assumed source of WD pollution. Based on this analysis, I showed that a few percent of WDs could be accreting moons, a fraction consistent with the number of WDs that are most highly polluted. This study theoretically validated the hypothesis that polluted WDs could be sampling exomoons, and emphasized the need to consider more massive parent bodies as WD polluters.

Chapter 3 is a statistical study of the compositions of WD pollution, with the goal of understanding whether the exoplanetary material observed in these systems requires compositions or rock types that are unusual compared to our solar system. I collected abundances from the literature for 31 WDs and compared their abundances to different solar system rocks. I found that about half of the pollution has compositions consistent with chondrites when considering all observed elements. Importantly, I showed that current uncertainties in abundance determinations for WDs do allow us to distinguish between samples that could be core or crust-like, but do not allow for more specific characterization on the level of different types of meteorites or Earth versus Mars. Given that the WDs indicated solar system-like material is fairly common, I then carried out a similar analysis using the elemental abundances of local stars in the Hypatia Catalog as an independent way to confirm that solar system-like compositions would be expected around most of our stellar neighbors. This work shows

that exotic compositions are likely not needed to explain the bulk of nearby exoplanets and drew connections for how the chemical evolution of the galaxy might trickle down to planet compositions.

Chapter 4 is also a statistical study of WD pollution compositions, this time focusing on inferred water mass fractions from observed elemental abundances. This study used a sample of 42 WDs collected from the literature, as well as data for a new H-dominated WD. I calculate water fractions from excess O abundances, relative to other rock-forming elements. I also test the impact of accretion and settling on the inferred water, as connecting observed WD abundances to a parent body requires making assumptions about what phase of accretion the WD is in, in order to alter the abundance ratios accordingly. This study uses one of the largest samples of polluted WDs, providing a good opportunity to test different accretion assumptions in systematic way. I explore the effects of accretion in two ways, first by manually applying different phases to each WD and measuring the variation in inferred water, and second by using an MCMC to recover the posterior distribution of accretion phases for each WD on the assumption that the true parent body had a chondritic composition. I find that abundance ratios and inferred water content are actually relatively immune to different accretion phases, and that the sample overall has a median water mass fraction of about 25%, similar to estimates for water in icy moons in our solar system.

Finally, Chapter 5 describes a different aspect of my work building towards a holistic picture of planet formation and evolution: the atmosphere loss in exoplanets due to small impactor. This study was motivated by periods of accretion and bombardment being important components of planet formation, with the power to alter atmosphere composition through removing mass and/or depositing material on young planets. I expanded an analytical model for atmosphere loss (Schlichting et al., 2015) to account for aerial bursts, or impactors which would break apart in the atmosphere before reaching the planet surface, and derived mass loss estimates for isothermal and adiabatic atmospheres. I showed that aerial bursts are most

effective on planets with thicker atmospheres, such as sub-Neptunes, and that each impactor could remove up to $\sim 10\%$ of its own mass in atmosphere.

CHAPTER 2

Exomoons as Source of White Dwarf Pollution

2.1 Introduction

White dwarfs (WDs) are the end-states of medium mass stars ($M_* \lesssim 8M_\odot$), and their high gravity leads to rapid sinking of any elements heavier than helium. This sinking occurs on the timescales of days to millions of years (Koester, 2009; Blouin et al., 2018), and generally leaves the spectra of white dwarfs devoid of metal features. Nevertheless, over a thousand white dwarfs have been observed to be 'polluted' with heavy elements (Coutu et al., 2019), with estimates that up to half of all white dwarfs are polluted (Koester et al., 2014). The source of the pollution is believed to be the remains of rocky parent bodies, which survived the post-main sequence evolution of the host star. Surviving planets can scatter these bodies onto highly eccentric orbits, such that the objects approach the white dwarf and are tidally disrupted and subsequently accreted by the star (e.g., Debes & Sigurdsson, 2002; Jura, 2003).

The majority of WD polluters appear rocky (Doyle et al., 2020; Swan et al., 2019) and a few appear icy (Hoskin et al., 2020; Farihi et al., 2013). Many accreted bodies are chondritic in composition, and based on this and their apparent masses, it has been often assumed that these parent bodies were small rocky bodies analogous to the asteroids, or Kuiper Belt objects (Xu et al., 2017), in the solar system. Here we attempt to quantify the fraction of polluting bodies that are exomoons rather than asteroids based on the parent body masses required for observed WDs and numerical simulations of the frequency of each population's

accretion. We are motivated by the recent discovery of beryllium in a polluted white dwarf (Klein et al., 2021) and the interpretation that the observed large excess in Be relative to other rock-forming elements is a tell-tale indicator that the parent body accreted by the WD was an icy moon. In this interpretation, the excess Be is the result of irradiation of the icy moon in the radiation belt of its host giant planet (Doyle et al., 2021). Payne et al. (2016) and Payne et al. (2017) showed that moons can be liberated by close encounters between planets and that liberated moons could be accreted by a white dwarf. Here we examine this proposal in greater detail using a statistical analysis and N-body simulations of the liberation and accretion of moons.

The probability of observing a moon versus an asteroid depends on the frequency and duration of the respective accretion events relative to the detectable amount of pollution on a typical WD. Based on occurence rates of dust around A-type stars, debris belts are expected to be ubiquitous amongst polluted white dwarf progenitors (Melis, 2016). Accordingly, assuming that any planetary systems with moons available for accretion would also have a debris belt available, the probability of observing moon versus asteroid accretion in a given WD system is

$$\frac{P_{\text{moon accretion}}}{P_{\text{asteroid accretion}}} = \frac{T_{\text{moons}}}{T_{\text{asteroids}}}, \tag{2.1}$$

where T is the fraction of time that the associated population provides observable pollution. Because we are interested in cumulative times, T is dependent on the accretion rate of each population ($T = T(\text{accretion rate})$).

Because asteroids are expected to accrete much more frequently than moons due to their sheer number, $P_{\text{moon accretion}}/P_{\text{asteroid accretion}}$ will depend on whether the accumulation of successive asteroid accretions is sufficient to sustain high masses of WD pollution, compared to the single accretion events of relatively larger-mass moons.

In this paper we estimate the parameters of Equation 2.1 for a system of three super-Earth to Neptune mass planets. A number of planetary architectures are capable of becoming unstable and aiding to feed meterial to the white dwarf (e.g., Maldonado et al., 2022; Stephan et al., 2017; Veras & Gänsicke, 2015), however, we focus on this particular system because existing studies of asteroid (debris) belts in this architecture provide a baseline against which to compare moon accretions.

Our paper is organized around Equation 2.1. In Section 2.2 we introduce an analytical model for masses of polluting elements in the WD convection zone, which we apply to all accretion events throughout this work. We show that this model implies that observed polluted WDs require masses much larger than one would expect for typical asteroid belt objects, emphasizing the need to understand moon accretions. In Section 2.3 we use observations of polluted WDs to put limits on the levels of pollution required for the accreter to be detectable. Section 2.4 finds $T_{\text{asteroids}}$, the cumulative timescale of detectability of asteroid pollution, using extrapolated asteroid accretion frequencies from previous studies. We present the results from our own N-body simulations for moon accretions in Section 2.4.2, and find T_{moons}. Finally, we summarize all quantities and discuss the implications of Equation 2.1 in Section 2.5.

2.2 Analytical Model for Convection Zone Masses

To determine the duration and pollution levels associated with an accretion event, we make use of the model by Jura et al. (2009) for the buildup of accreted material in a white dwarf atmosphere. Throughout this work we will refer to the model as J09. The model describes the time-dependent mass of the polluter currently observable in the convection zone of a white dwarf as a function of polluting parent body mass, element settling times through the WD atmosphere, and the duration of the accretion event. The model assumes the accretion disk, and therefore accretion rate, decays exponentially as one might expect from dissipative

forces that depend on mass. Under this assumption, the mass of element Z that is observed to be in the convection zone of the white dwarf at the time of observation t after the start of the accretion event, $M_{CV}(Z,t)$, is:

$$M_{\rm CV}(Z,t) = \frac{M_{\rm PB}(Z)\tau_{\rm set}(Z)}{\tau_{\rm disk} - \tau_{\rm set}(Z)} \left(e^{-t/\tau_{\rm disk}} - e^{-t/\tau_{\rm set}(Z)}\right), \tag{2.2}$$

where $M_{\rm PB}(Z)$ is the mass of element Z in the parent body, $\tau_{set}(Z)$ is the e-folding settling time of element Z, and $\tau_{\rm disk}$ is the characteristic lifetime of the accretion disk.

The observable pollution mass $M_{\rm CV}(Z,t)$ in J09 depends on the settling timescale, which in turn depends on the properties of the host star. Therefore, variations in white dwarf temperature and composition have significant impacts on the maximum accumulations of pollution in the WD atmosphere and the timescales during which pollution levels are sufficiently high to be observable. In Figure 2.1 we show the pollution masses for a representative element and parent body in a DA (top) and a DB (bottom) white dwarf in order to illustrate these differences. Defined spectroscopically, DAs have atmospheres dominated by hydrogen, while those of DB white dwarfs are helium-dominated. While white dwarf classifications extend well beyond these two categories, for simplicity we will restrict our discussion to these two broad categories, using the terms DA and DB to mean hydrogen and helium-dominated in what follows. The primary difference between the two types of WDs in the present context is that DAs generally have settling timescales for the heavy elements of days to thousands of years while the DBs have settling timescales of 10^5 to 10^6 yr for these elements. Additionally, because hot DAs will have minimal, if any, convection zones, we consider $M_{\rm CV}$ to more generally represent the mass of observable pollution in the WD atmosphere for these cases.

The maximum heavy element mass in the convection zone for each WD type occurs where settling times are approached. In other words, the maximum is the amount of accreted material that can build up in the atmosphere before sinking exerts an influence on the

abundances. In the example to follow, we assume a settling time of 10^2 yr for the DA and 10^6 yr for the DB. Both cases are assigned an accretion disk e-folding lifetime of 10^5 yr.

In Figure 2.1, we show the fraction of the parent body mass that is currently observable in the convection zone as a function of time since the start of accretion, for an exemplary heavy element. Both cases illustrate the three phases of pollution: while accretion is ongoing and before settling begins, the mass of the element builds up in the atmosphere (increasing phase). When the settling and accretion rates equalize (the blue point in Figure 2.1), the mass stays relatively constant (steady state). Once settling dominates as accretion wanes, the mass of the pollution decreases rapidly (decreasing phase). Note that, in this model, the majority of a single accretion event is in a decreasing phase.

Because settling in the DBs begins after the majority of the parent body has been accreted onto the white dwarf, DBs can exhibit much larger fractions of the polluting metals than DAs, for the same parent body mass. The DA steady state phase occurs earlier and therefore at relatively higher settling and accretion rates than the DB phase, and the two DA rates conspire to cause very small fractions of the parent body to be observable at any given time.

Estimates for $\tau_{\rm disk}$ generally range from 10^4 to 10^6 yr (e.g., Girven et al., 2012). In Figure 2.2 we show how varying the disk timescale changes the pollution curves for the theoretical DA and DB stars shown in Figure 2.1. In particular, note that the maximum of the DA pollution decreases much more rapidly with increasing disk lifetimes than in the case of DBs.

We employ J09 in two ways. First, we estimate the parent body masses responsible for observed pollution in a sample of 21 white dwarfs and compare these masses with the distribution of asteroid and moon masses in our own solar system (Section 2.2.1). Secondly, we use the model in conjunction with the average masses of asteroids and moons to determine the timescales of observability for both populations (Section 2.3).

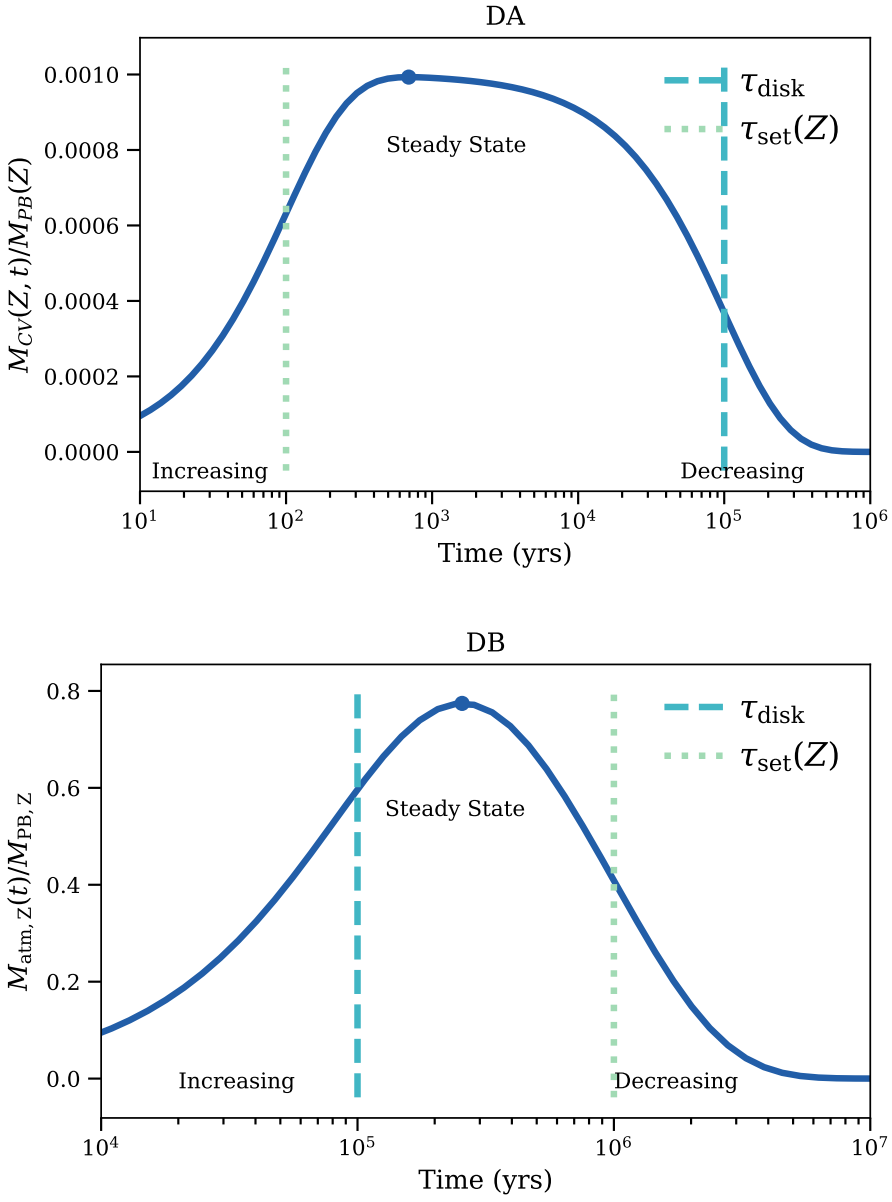

Figure 2.1: Examples of the fraction of parent body masses of a particular element that are predicted to be in the convection zone of a WD as a function of time, according to the J09 model (Equation 2.2). We assume an accretion disk lifetime of 10^5 yr and settling times of 10^2yr for the DA (top) and 10^6yr for the DB (bottom). Note the three phases of accretion: increasing, steady state, and decreasing. While analogous phases occur both for the DA and DB, the timescales defining the boundaries of each phase are swapped due to the longer DB settling times.

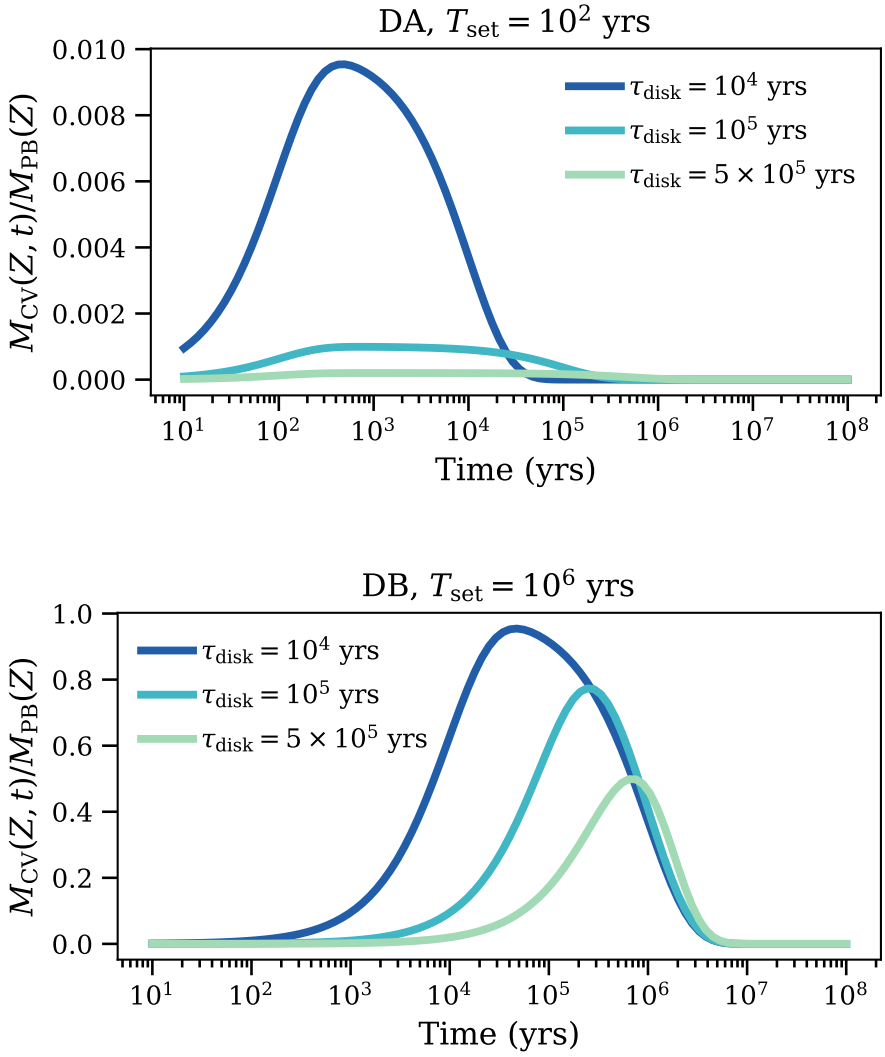

Figure 2.2: Fraction of parent body mass for a typical rock-forming element in the convection zone of a WD as a function of time, for three different accretion disk lifetimes. The DA pollution curves decrease by nearly a factor of ten with increasing disk times, while the DB curves decrease less significantly. The peaks of both curves shift to later times as the disk accretion time increases, reflecting changes in the time where steady state between accretion and settling is achieved.

2.2.1 Steady-State Parent Body Masses

In order to calculate parent body masses for polluted white dwarfs, observed pollution masses ($M_{\rm CV}(Z)$) and settling times were collected from the references in Table 2.1. The total masses of heavy elements in each white dwarfs are shown in Figure 2.3. For an assumed disk timescale we then solve Equation 2.2 for the parent body mass at a range of possible elapsed accretion times for each observed element in the white dwarf. This gives an expression for the mass of element Z in the parent body for an assumed elapsed accretion time $t_{\rm elapse}$ and an observed metal mass of $M_{\rm CV}(Z)$:

$$M_{\rm PB}(Z, t_{\rm elapse}) = \frac{M_{\rm CV}(Z)(\tau_{\rm disk} - \tau_{\rm set})}{\tau_{\rm set}\left(e^{-t_{\rm elapse}/\tau_{\rm disk}} - e^{-t_{\rm elapse}/\tau_{\rm set}}\right)}. \tag{2.3}$$

Note that we change the time variable to $t_{\rm elapse}$ to emphasize the difference in the meaning of time between Equations 2.2 and 2.3. Equation 2.2 solved for the variation in polluting element mass with time since accretion for a single parent body mass. Equation 2.3 instead takes an observed heavy metal mass and provides a range of parent body solutions that depend on the time at which one assumes the observation was taken. To obtain the total parent body mass solution, we sum over all observed elements at a given elapsed accretion time, such that $M_{\rm PB}(t_{\rm elapse}) = \sum M_{\rm PB}(Z, t_{\rm elapse})$.

As an example, Figure 2.4 shows the application of Equation 2.3 to the DA G149-28, and DB WD 2207+121. The vertical lines show the settling times for each element associated with each WD and the assumed disk lifetimes of 10^5yr. Note that the shape of the parent body solution is roughly the inverse of the pollution mass curve, reaching a minimum during the steady state phase of accretion, when the pollution mass is at a maximum. Equation 2.3 shows that the steady state point, $dM_{\rm PB}(Z, t_{\rm elapse})/dt_{\rm elapse} = 0$, coinciding with the minimum estimate for the parent body mass, will occur at time:

$$t_{\rm min} = \frac{\tau_{\rm disk}\tau_{\rm set}}{\tau_{\rm disk} - \tau_{\rm set}} \ln\left(\frac{\tau_{\rm disk}}{\tau_{\rm set}}\right). \tag{2.4}$$

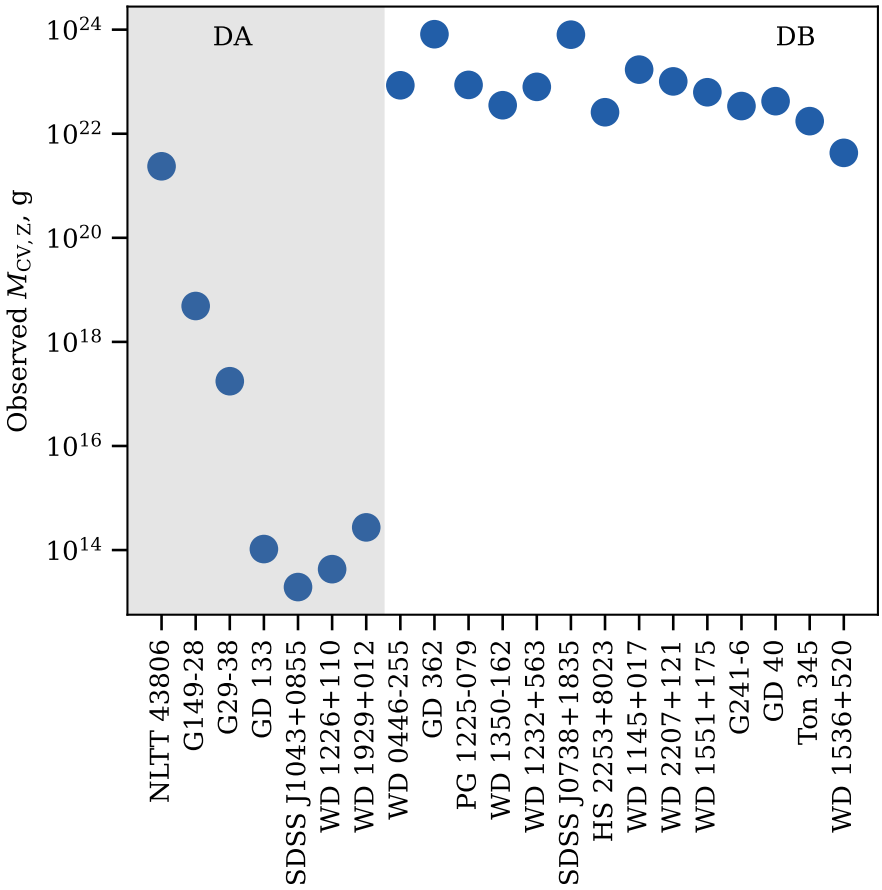

Figure 2.3: Total masses of heavy metals observed for the white dwarfs in Table 2.1, sorted by type. The DAs tend to have lower observed masses of polluting elements compared to the DBs.

Table 2.1: All white dwarf parameters are collected from the references listed in the table. Any values not reported by the paper have been supplemented using the Montreal White Dwarf Database (Dufour et al., 2017). Throughout this work we group white dwarfs by their primary classification type (DA or DB only).

White Dwarf	Type	$T_{\rm eff}$ (K)	log(g)	M$_*$ ($M_\odot$)	log(q)	Disk†	Reference
NLTT 43806	DA	5830	8.00	0.587	-6.661	N	Zuckerman et al. (2011)
G149-28	DA	8600	8.10	0.657	-9.224	N	Zuckerman et al. (2011)
G29-38	DA	11820	8.40	0.858	-12.61	Y	Xu et al. (2014)
GD 133	DA	12600	8.10	0.667	-15.434	Y	Xu et al. (2014)
SDSS J1043+0855	DA	18330	8.05	0.649	-16.645	Y	Melis & Dufour (2017)
WD 1226+110	DA	20900	8.15	0.714	-16.663	Y	Gänsicke et al. (2012)
WD 1929+012	DA	21200	7.91	0.578	-16.283	Y	Gänsicke et al. (2012)
WD 0446-255	DB	10120	8.00	0.581	-5.242	N	Swan et al. (2019)
GD 362	DB	10540	8.24	0.732	-5.789	Y	Xu et al. (2013)
PG 1225-079	DB	10800	8.00	0.582	-5.235	Y	Xu et al. (2013)
WD 1350-162	DB	11640	8.02	0.596	-5.273	N	Swan et al. (2019)
WD 1232+563	DB	11787	8.30	0.773	-5.924	N	Xu et al. (2019)
SDSS J0738+1835	DB	13950	8.40	0.842	-6.324	Y	Dufour et al. (2012)
HS 2253+8023	DB	14400	8.40	0.842	-6.408	N	Klein et al. (2011)
WD 2207+121	DB	14752	7.97	0.572	-5.591	Y	Xu et al. (2019)
WD 1551+175	DB	14756	8.02	0.601	-5.691	Y	Xu et al. (2019)
WD 1145+017	DB	14500	8.11	0.655	-5.819	Y	Fortin-Archambault et al. (2020a)
GD 40	DB	15300	8.00	0.591	-5.805	Y	Jura et al. (2012)
G241-6	DB	15300	8.00	0.591	-5.805	N	Jura et al. (2012)
Ton 345	DB	19780	8.18	0.706	-7.883	Y	Wilson et al. (2015)
WD 1536+520	DB	20800	7.96	0.578	-8.938	N	Farihi et al. (2016)

* q is the fraction of stellar mass in the stellar envelope. Note that the DA WDs have much smaller stellar envelopes.

† Debris disks indicated for WDs with detected infrared excesses.

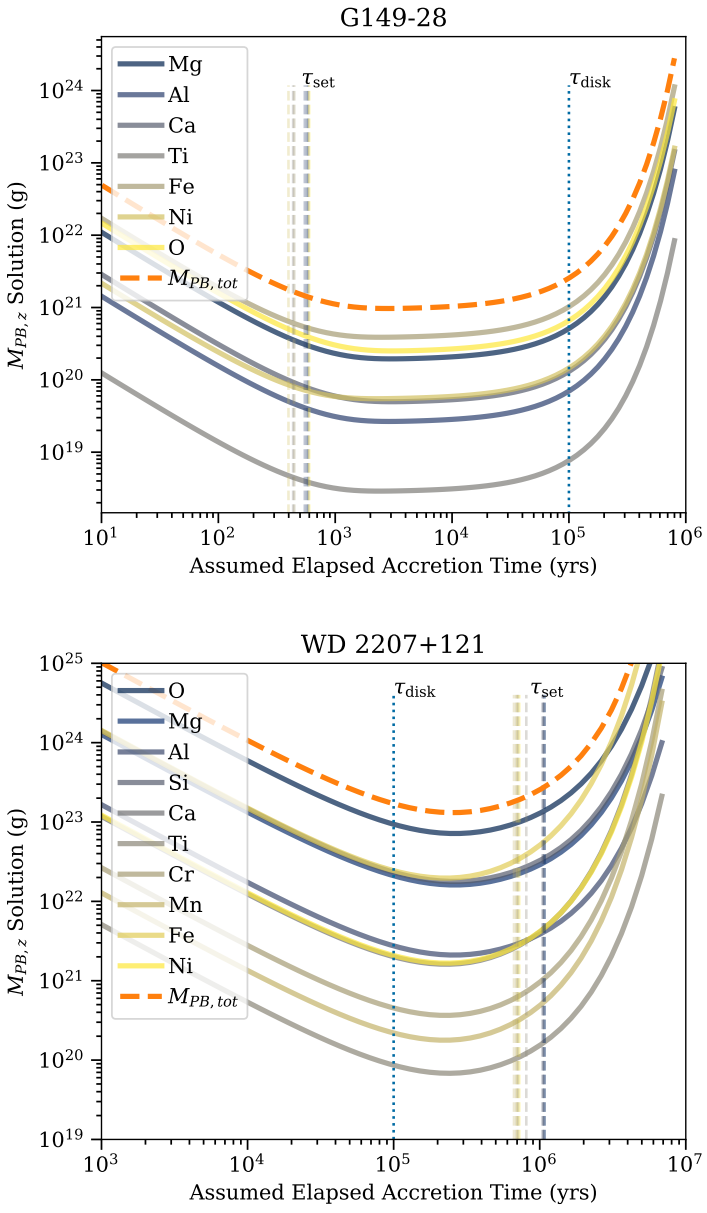

Figure 2.4: An example plot of the parent body mass calculated from Equation 2.3 as a function of assumed elapsed accretion time for the DA G149-28 (top) and DB WD 2207+121 (bottom). We assume an accretion disk lifetime of 10^5 years (dotted line). Settling timescales for the DB are approximately 10^6 years, those for the DA are $\sim$ 400 yr, and both are marked in dashed lines for each element. The parent body solution derived from Equation 2.2 is plotted for each element, and the dashed orange line shows the sum of all parent body elements at each assumed elapsed accretion time.

In practice, when summing over multiple elements as in Figure 2.4, each element would reach the steady state point at slightly different times, due to the variations in settling times. Nonetheless, as long as the range of settling times are well above or below the disk lifetime, solving for elemental abundances at the time corresponding to steady state will give a minimum estimate for the total parent body mass. Thus, for the remainder of this work one can think of the 'minimum parent body mass' to be analogous to the 'parent body solution assuming steady state.' Note that this does not necessarily mean we are assuming all white dwarfs are in steady state, but rather that any other phase of accretion would require a more massive parent body than the steady state solution to explain the observed metal pollution.

We calculate parent body masses for the white dwarfs in Table 2.1 using the effective temperature and log g values reported in the references to obtain the WD convection zone masses and elemental settling times from the Montreal White Dwarf Database (MWDD) (Dufour et al., 2017). We then derive $M_{\rm CV}(Z)$ values from the relative abundances reported in the references, using the MWDD settling times and white dwarf envelope mass fractions. For comparison, we also considered the models provided by Koester et al. (2020), which calculate settling times that include the lack of convection zones in hot, hydrogen dominated white dwarfs. We find that the settling timescales derived in the Koester models are generally comparable to those reported by the MWDD, and therefore do not significantly change the resulting parent body masses.

Additionally, while we use all stellar parameters from the MWDD instead of those reported in each reference, we find that in most cases the values are in agreement, to within a factor of a few.

Minimum parent body solutions for the observed white dwarfs are shown in Figure 2.5, for a range of disk timescales. Because of the marked dependence on disk lifetime (Figure 2.2), we expect variations in assumed disk lifetime to change the minimum parent body estimates

for DAs much more than for DBs. This expectation is realized, as shown in Figure 2.5.

We find that the majority of parent body estimates for DB WDs are between roughly 10^{23}-10^{24} g regardless of the disk timescale chosen. DA estimates are generally lower unless we increase the disk timescale to 10^7 yr. This is beyond current estimates for disk lifetimes given in the literature, but does provide a more satisfactory agreement between parent body masses for DA and DB white dwarfs. Despite that effect, we will adopt a disk timescale of 10^5 yr for the remainder of our analysis as that value is more generally accepted in the literature and results in lower parent body masses that we can take as minimum estimates.

Figure 2.6 shows the elapsed accretion times corresponding to the minimum parent body solution for each WD in the sample, using the stellar parameters from MWDD, and with a disk lifetime of 10^5 years. The upper and lower limits show the range of accretion times for which the parent body solution is within a factor of two of the minimum.

In Figure 2.7 we show how the distribution of calculated parent body masses (assuming a disk lifetime of 10^5 yr) compares to the distributions of moon masses in the solar system as well as to the approximate distribution of asteroid masses. Moon masses and radii are from the JPL Solar System Dynamics group [1]. We calculate the asteroid masses assuming the distribution of asteroid radii is $dN \propto r^{-3.5}dr$ (Dohnanyi, 1969), and that all bodies have the same density of 3 g/cm^3. In reality, the majority of asteroids have lower densities ($\sim$ 2.5g/cm^3), so we can consider the asteroid masses as upper limits. We assume that the range of asteroid diameters is 1-1000 km, corresponding with a range of masses of approximately $10^{15} - 10^{24}$ g. The WD pollution parent body masses are generally far larger than those defined by the asteroid distribution. While the DA parent body masses and the majority of the DB masses reside in the range of the largest bodies in our asteroid belt, such as Ceres ($\sim 10^{24}$ g) or Vesta ($\sim 10^{23}$ g), they are well above the bulk of the asteroid mass distribution. From our sample, for a disk timescale of 10^5 yr, we consider a mean DA parent body to be $\sim 10^{21}$ g

[1] https://ssd.jpl.nasa.gov/ (Giorgini et al., 1996) data taken 2021 August

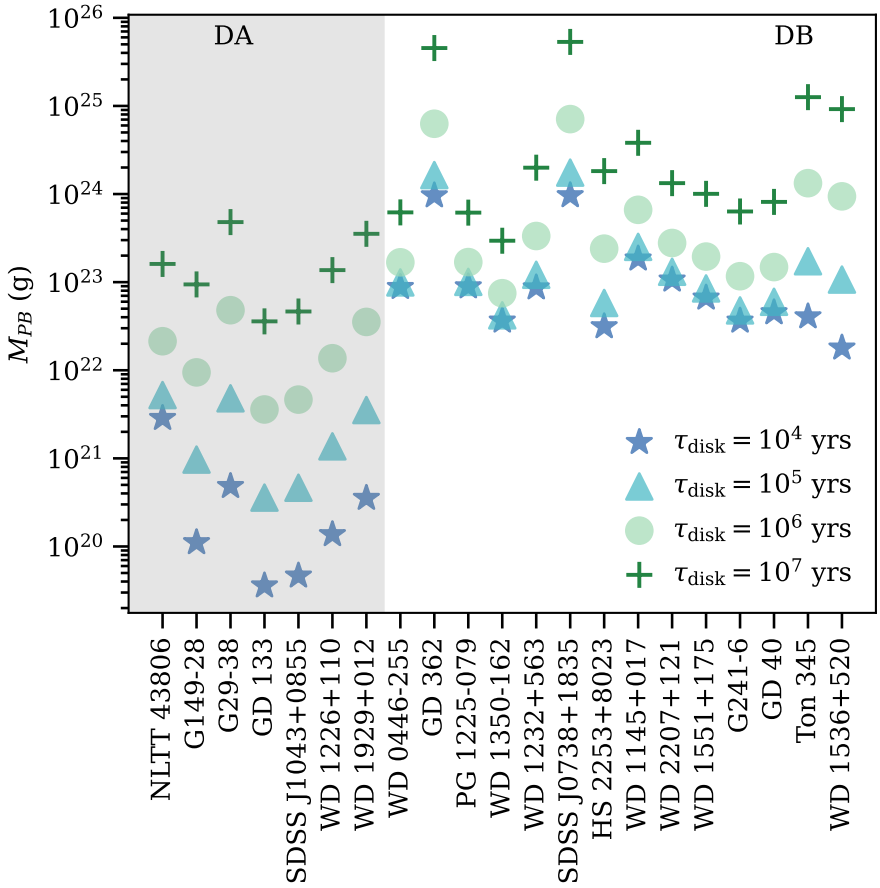

Figure 2.5: Parent body masses calculated assuming the white dwarf is in steady state, with four different assumed accretion disk timescales. DA parent body solutions tend to vary more dramatically with disk timescale than the DBs. Most DB parent body mass solutions are close to $\sim 10^{23}$,and while the DA solutions are somewhat lower, the two begin to converge as disk timescales increase. Note that the 10^7 yr timescale is longer than most estimates for disk timescales.

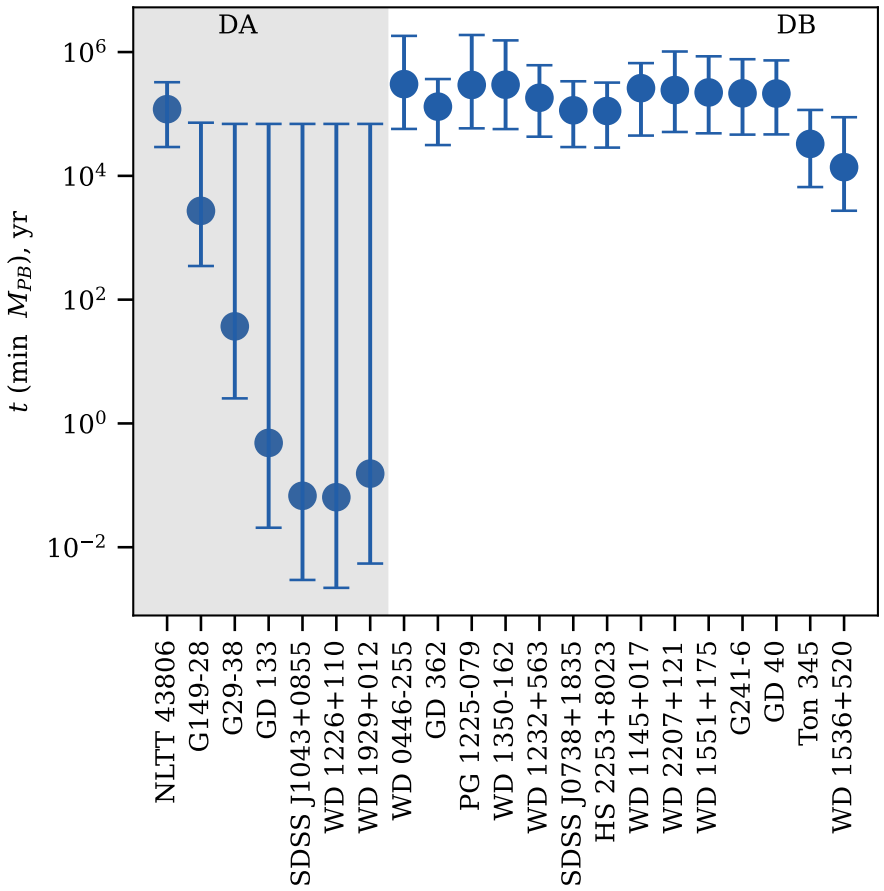

Figure 2.6: Elapsed accretion times at which we calculate the minimum parent body mass solution, or equivalently the times where accretion and settling rates are equal. The upper and lower limits for each WD show the range of elapsed accretion times for which the parent body mass is within a factor of two of the minimum.

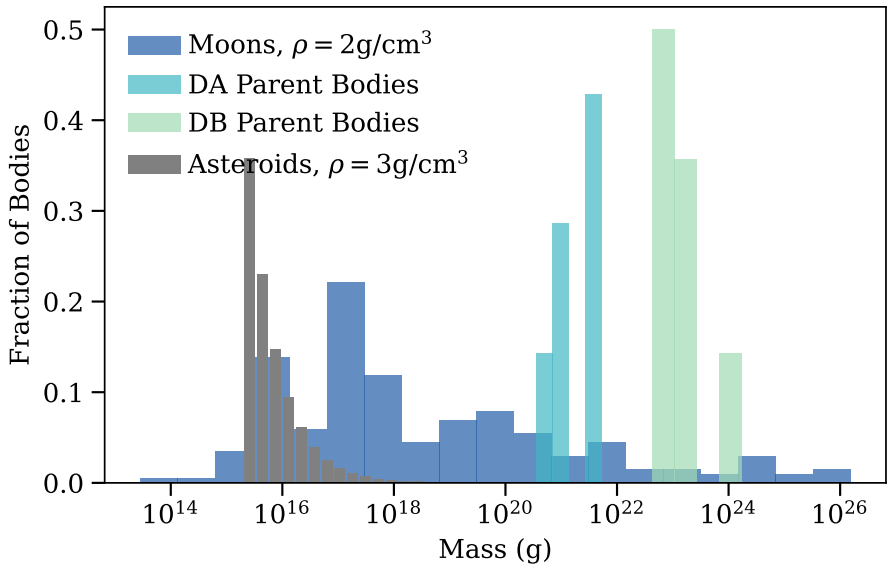

Figure 2.7: Fraction of bodies in each population with a given mass. Densities of 2.5 and 2 g/cm^3 are assumed to calculate masses for asteroids and moons, respectively. The asteroid curve is derived from Dohnanyi (1969) and the moon data are from the JPL Solar System Dynamics group. The parent body masses are split into DA and DB populations and assume a disk lifetime of 10^5 yr. The DBs tend to have larger parent body mass solutions, though the masses for both the DAs and DBs are situated towards the tail end of asteroid masses and mid-to-high moon masses. Note that the parent body masses shown are lower limit solutions.

and a mean DB to be $\sim 10^{23}$ g. In our solar system, there are about 30 and 15 moons that fall above these DA and DB masses, respectively.

The large calculated parent body masses compared to minor solar system bodies implicates an observational bias. This may be partially due to the large masses required to detect pollution, which we outline in the next section.

2.3 Pollution Detection Limits

In Section 2.2.1, we showed that in the context of the J09 model, most observed WD pollution requires parent body masses consistent with the more massive moons of the solar system,

and the extremely rare most massive asteroids. We now turn to observations to determine a lower limit of observable pollution in a WD atmosphere to place further constraints on the differences between moon and asteroid pollution.

Lower limits for observable masses of pollution in white dwarf atmospheres are obtained from measurements of calcium masses in polluted WDs. We choose calcium because there is a large sample of observations for Ca available in the literature with which we can assess minimum masses. We collect Ca masses for DA WDs from the SPY Survey (Koester et al., 2005) and masses for the DBs from Zuckerman et al. (2010). We first approximate a line to the lowest calcium masses in the SPY survey to derive an expression for minimum mass as a function of effective temperature (equation 2.5). We then use the DB data to renormalize the line for the DB WDs. Because the data are expressed by number relative to hydrogen/helium, the relation between the minimum masses and temperature is dependent on the mass of the convection zone (mass of hydrogen for DAs or helium for DBs). Our expressions for the minimum masses of Ca that are observable in the polluted WDs are

$$\begin{aligned} M_{\text{min Ca, DA}} &= 10^{\frac{4\ T_{eff}(K)}{15000}-12.6} \times \frac{m_{Ca}}{m_H} \times M_{CV} \\ M_{\text{min Ca, DB}} &= 10^{\frac{4\ T_{eff}(K)}{15000}-14.2} \times \frac{m_{Ca}}{m_{He}} \times M_{CV}, \end{aligned} \tag{2.5}$$

where m_{Ca} is the mass of calcium, m_{H} is the mass of hydrogen, m_{He} is the mass of helium, and M_{CV} is the mass of the WD convection zone or WD atmosphere. As the atmospheres of DAs tend to be relatively small (see Table 2.1), their limits of detectable calcium mass are much lower than that of DBs.

Applying Equation 2.5 to the white dwarfs in Table 2.1, we obtain the minimum detectable calcium mass in the observable layers for each WD. The DBs have detection limits of $\sim 10^{18}$ g Ca, while the DA limits extend to orders of magnitude lower. The lower limit for calcium detection in the DAs is consistent with their lower observed $M_{\text{CV},Z}$ values, as described

above.

Taking the minimum observable calcium masses for each of the observed WDs, we now use the J09 model to calculate the parent body mass associated with each calcium mass limit. For each WD, we first apply the J09 model to the minimum detectable calcium mass to find the minimum mass of calcium in the parent body. We then calculate the total parent body mass by assuming chondritic composition ($\sim 1\%$ calcium by mass), an accretion disk e-folding time of 10^5 years, and settling times provided by the MWDD based on the effective temperature of each WD. Figure 2.8 shows the resulting parent body masses associated with the extrapolated minimum observed calcium mass for each WD in our sample. These bodies would provide just enough calcium pollution to be detected with current technology.

While the instantaneous minimum observable pollution masses derived from equation 2.5 require much higher masses for the DBs, we find that DAs and DBs require similar overall parent body masses to produce observable pollution. This is due to the difference in fractions of parent body that can build up in each type of atmosphere (Figure 2.1). Assuming each parent body is accreting as a single event, the resulting minimum parent body masses required for observable pollution for both types of WDs are generally larger than the mean for solar system asteroids, and closer to the masses of solar system moons, suggesting an observational bias against “typical" asteroids.

In the following sections we will examine how moons and asteroids compare when we allow for continuous accretion of material. This approach is particularly necessary for asteroids, which are thought to reach accretion rates that require material from multiple objects to be present in the WD atmosphere at any one time. Going forward, we will adopt the instantaneous minimum observable mass limits of 5.3×10^{16} and 1.3×10^{20} g of total heavy elements for a typical DA ($T_{\rm eff}$ = 10000 K) and DB ($T_{\rm eff}$ = 14000 K), respectively. For single chondritic accretions, these limits correspond to minimum observable total parent body masses of 1.3×10^{19} g for the DA and 1.7×10^{20} g for the DB. Note that because

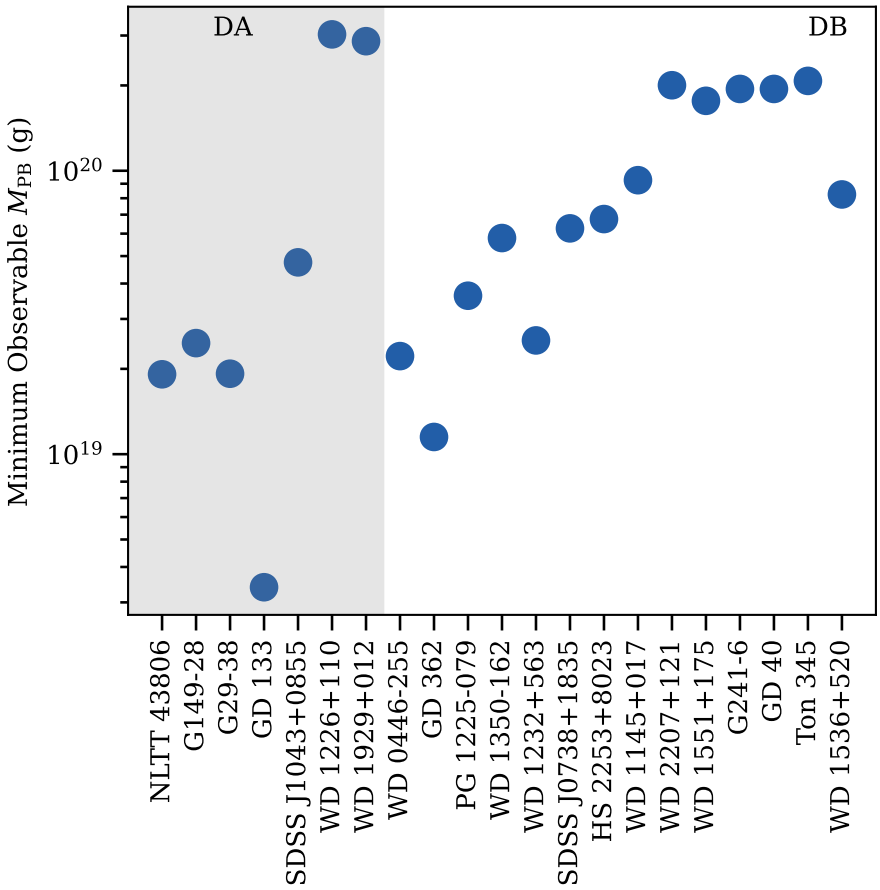

Figure 2.8: Calculated minimum detectable parent body masses associated with the detection limit for Ca, assuming chondritic parent body compositions. To obtain these masses, we solve the J09 model for the minimum mass of calcium in the parent body, assuming an $M_{\mathrm{CV},Ca}$ according to Equation 2.5. We then calculate the minimum parent body mass solution by assuming chondritic composition, settling timescales from MWDD corresponding to the effective temperature of each WD, and a disk timescale of 10^5yr.

DAs accumulate much smaller fractions of parent body in their atmospheres at steady state, the minimum observable parent body masses for DAs and DBs are similar, despite orders of magnitude differences in their instantaneous limits.

2.4 Continuous accretion models for asteroids and moons

While describing the J09 model in Section 2.2, we considered the increasing, steady state, and decreasing phases for a single accreting body. However, it is possible that pollution in the WD atmosphere could be from multiple parent bodies. In particular, Mustill et al. (2018) find that asteroids can accrete onto WDs continuously for up to billions of years. To assess how much of the pollution from continuous accretion could fall within observable limits, we consider populations of potential polluters based on mass frequency distributions of asteroids and moons in the solar system as guides. We then use total accretion rates determined previously from N-body simulations to construct synthetic pollution curves by applying the J09 model (Equation 2.2) to each event.

We currently restrict the comparison of moon and asteroid accretion to a three-planet system of super-Earths and Neptunes, a system that has previously been shown to result in high rates of asteroid accretion by Mustill et al. (2018). Additionally, we focus on the first 200 Myr past WD formation, the time frame in which asteroid pollution levels are expected to be at their maximum.

2.4.1 Asteroid Accretion

Mustill's simulations show that in the first few million years after WD formation, a debris belt can reach a peak accretion rate of $\sim 10^{-4} N_{\rm AB}/\rm{Myr}$, where $N_{\rm AB}$ is the number of asteroid belt objects. Because the 200 Myr time span is relatively short compared to the full length of time considered in the Mustill simulations, we consider the accretion rate to be approximately constant in our calculations. We therefore use the accretion rate to constrain

the total number of accretions that can occur within the 200 Myr period, and then pick the specific accretion event times randomly from a uniform distribution, such that each point in time is equally likely to be the start of an accretion event.

The masses of accreting bodies for each event are chosen at random, without replacement, from the distribution of masses representing the solar system asteroid belt. We assume a range of radii of $0.5 - 500$ km and a total mass of the asteroid belt of 3×10^{24} g. Dohnanyi (1969) found the radius distribution for a collisionally-generated debris belt to be $dN \propto r^{-3.5}dr$. Translating this distribution into masses, we have an asteroid mass range of $1.6 \times 10^{15} - 1.6 \times 10^{24}$ g and $dN \propto \rho^{5/6} m^{-11/6} dm$. The total mass of the belt is then $M_{\rm belt} \propto \int m dN$, which we constrain to be the mass of the asteroid belt. Assuming that all bodies are spherical, we obtain $M_{\rm belt} = A \int \rho \frac{4\pi}{3} r^3 r^{-3.5} dr$, where A is a constant, and ρ is the density of the asteroids. Assuming a constant density of 3 g/cm^3 and our adopted radius range of $0.5 - 500$ km, we find $dN = 1.7 \times 10^{19} r^{-3.5} dr$. This gives a total of about 12 million objects in the debris belt, for an accretion rate of approximately 1200 events/Myr. We therefore will only accrete a fraction of the total number of bodies in the full 200 Myr time period.

To sample this distribution, we split the range of asteroid masses into 12 bins, spaced logarithmically in mass, a choice which leaves one object in the Ceres-mass bin. We assign each object in the belt a mass bin according to the distribution described previously, again assuming a constant asteroid density of 3 g/cm^3. For each accretion event, we pick an object at random, identify its mass bin, and select a mass at random from the range of masses associated with that bin. We obtain masses of individual elements in the parent body by assuming chondritic composition, and then evolve these masses through the J09 model (Equation 2.2) to track the total masses of polluting elements in the WD atmosphere. The number of bodies in the selected bin is then decreased by one.

The upper panels of Figure 2.9 show the results of this calculation assuming a disk e-folding time of 10^5 yr and settling times for a 10000 K hydrogen-dominated WD and 14000 K

helium-dominated WD. Each peak in the figure corresponds with an accretion event, and is followed by a tail during which mass sinks out of the atmosphere. The colored curves show the mass of individual elements comprising the polluting debris in the convection zone as a function of time and the black dashed curve shows the total mass of heavy elements in the convection zone. Note that because asteroid accretions are very frequent compared to the settling timescales, material from at least one body can be found in the mixing layer for the majority of the 200 Myr time interval.

In Section 2.3 we found that the minimum convection zone pollution mass that is observable is about 5.3×10^{16} g for a typical DA WD and 1.3×10^{20} g for a typical DB, as derived from observed calcium masses. The horizontal lines in Figure 2.9 show the detectability threshold, and any peaks in pollution that exceed these limits are considered detectable periods of accretion.

In both the DA and DB cases, a long-term mass of pollution is sustained in the atmosphere, with peaks when more massive asteroids accrete. The sustained background pollution is generally not enough to exceed detection limits, but the more massive asteroid accretions are observable. This suggests that while multiple debris belt objects may be contributing to observed pollution, it is likely that the majority of the observed mass is due to a single, more massive body. We find that asteroid accretions onto the DA can exceed the pollution detection limit for a total of ~ 29 Myr, resulting in a cumulative fraction of observable time of $T_{\mathrm{asteroids,DA}} = 0.145$

All else equal, pollution levels are higher for the DB case than the DA case as more mass can build up in the DB WD atmosphere due to slow settling times. Overall, in the DB simulation, the pollution is at an observable level for a total of ~ 72 Myr out of the 200 Myr interval, such that $T_{\mathrm{asteroids,DB}} = 0.360$.

We note that in the asteroid accretion scenarios, the maximum masses of heavy elements

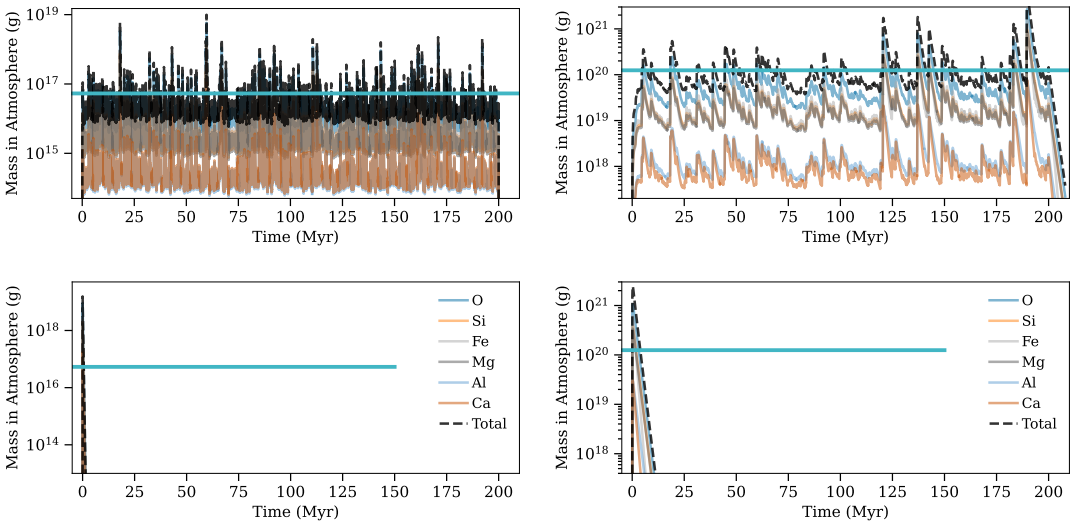

Figure 2.9: Synthetic pollution mass curve for an asteroid belt (top) and a single moon event (bottom) as a function of time post WD formation. The black dashed line shows the total mass of pollution in the convection zone, the colored lines show the pollution mass per element. The horizontal line shows the minimum detectable mass of heavy elements. The left column shows accretion onto a DA WD while the right shows pollution of a DB. Top row: Continuous accretion of an asteroid-mass debris belt, based on the mean accretion rate of Mustill et al. (2018) and assuming the distribution of masses follows that of the solar system asteroid belt. Bottom row: Accretion of a single moon of mass $\sim 10^{20}$ g onto a typical DA (left) and a moon of mass $\sim 10^{21}$ g onto a typical DB (right). These masses represent the median mass of the subset of solar system moons that satisfy the criteria for being liberated from their host planets and providing observable levels of metal pollution.

that accumulate in the WD atmosphere are $\sim 5 \times 10^{16}$ g for the DA and $\sim 10^{20}$ g for the DB. From Figure 2.3, we see that the WDs in the observed sample have total masses of heavy metals that can exceed the maxima reached by our continuous asteroid accretion simulation by factors of up to $\sim 10^3$. In addition to the expected vicissitudes of extrasolar asteroid belt masses, we consider that the higher observed masses could be due accretion of moons.

2.4.2 Moon Accretion Simulations

We carried out the same calculations for moons around WDs as we did for the asteroids in order to compare the expected detectability of accretion events for the two sources. For this purpose we require an accretion rate for moons. This rate comes from the efficacy of liberating moons from host planets, and the accretion rate of the liberated moons onto the WD.

We simulate the separation of moons from their host planets during the stellar mass loss event that produces the WDs in order to estimate $f_{\rm moons}$, the frequency of moon accretions by WDs. Because moon orbital periods require very short time steps for integration, we break down $f_{\rm moons}$ into two parts to accommodate computational limits. We define $f_{\rm moons}$ as $N_{\rm moons} \times f_{\rm accrete}$, where $N_{\rm moons}$ is the number of moons in the system that can be liberated from their host planets and are able to provide detectable levels of pollution on a WD and $f_{\rm accrete}$ is how frequently a moon from this population reaches the white dwarf.

We use the N-body code REBOUND (Rein & Liu, 2012) to model three planets each with two moons. The IAS15 adaptive time-step integrator (Rein & Spiegel, 2015) allows time-steps to be shortened or lengthened according to the occurrence of close encounters between particles. Due to computational limits, we set the smallest allowable timestep to be 0.1 days. Following the approach described in Payne et al. (2017) for moon liberations, we start each simulation with a three-planet system (no moons) and integrate the planet orbits during stellar mass loss. The mass loss excites the planetary orbits, eventually leading to orbit crossings. We

halt this portion of the simulation at the first orbit crossing, when the periapsis of any planet falls below the apoapsis of the adjacent interior planet, or, alternatively, when the apoapsis exceeds the periapsis of the adjacent exterior planet. At this point we insert two test particle moons around each planet (6 moons in total). The simulation is then resumed, including stellar mass loss if it is still ongoing.

During the moon and planet portion of the simulation, we consider a moon to be accreted by the white dwarf if it passes within the Roche limit of the white dwarf ($\sim$ 0.005 AU). However, we note that it is possible that bodies farther away than 0.005 AU could still be accreted by the white dwarf, for example through Alfven wave drag (Zhang et al., 2021). Averaging the frequency of moon accretions across all simulation trials gives $f_{\rm accrete}$.

2.4.3 Initial Conditions for Moon Simulations

While Payne et al. use planetary architectures as simulated by Veras & Gänsicke (2015) and Veras et al. (2016) to assess moon accretion, we carry out our tests using the same three-planet system simulated by Mustill et al. (2018) (Section 2.4) in order to compare our results for moon accretions to those of debris belt accretions.

Each of our simulations begins with three planets around a $3M_{\odot}$ main sequence host star that evolves into a $0.75M_{\odot}$ white dwarf. The planets have masses of 1.3, 30.6, and 7.8 $M_{\oplus}$ and initial semi-major axes of 10, 11.6, and 13.07 AU, respectively, as prescribed by the Mustill simulations. We focus on this particular set of planets as they resulted in the largest fractions of asteroids engulfed by the white dwarf in the Mustill study. We choose random initial inclinations in the range $[0°, 1°]$, initial eccentricities of zero, and random values between 0° and 360° for all other orbital angles.

Stellar mass loss is incorporated by updating the stellar mass according to the analytical formulae for single-star evolution by Hurley et al. (2000). This code calculates stellar properties over 1 Gyr. For simplicity each of our simulations begins at the start of stellar mass

loss such that white dwarf formation occurs ~ 100 Myr after the start of the simulation.

For the three-planet systems, the first orbit crossing usually occurs before the end of the stellar mass loss event. Because mass loss speeds up significantly towards the end of the 100 Myr interval, the stellar mass is usually still close to $\sim 3M_{\odot}$, and the semi-major axes of the planets have generally not increased dramatically, when the simulation is paused for moon insertion.

We follow the prescription for moon insertion described by Payne et al. (2017). The semi-major axis of each moon relative to the planet is chosen randomly in the range $r_{\rm min} < a_{\rm moon}/R_H < 0.4$, where R_H is the instantaneous Hill radius of the planet at the moment of the first orbit crossing. We considered two $r_{\rm min}$ values of 0.004 and 0.04. This range results in numerically manageable, stable orbits. Payne et al. found that once moons are liberated from their host planet, the initial conditions of the moons cease to matter due to the intense scattering each moon experiences. The initial inclination of each moon is randomly chosen to be within 1° of the plane of planetary orbits, the eccentricity is set to zero, and all other angles are randomly chosen.

For comparison with our initial conditions, Figure 2.10 shows the distributions of semi-major axes relative to the host planet Hill radii for solar system moons. Data are gathered from the JPL Solar System Dynamics group, and we assume a uniform density of 2 g/cm^3 for all bodies. The top panel shows the distribution of semi-major axes of moons by planet, and the lower panel shows the masses for the solar system moons. The range in $a_{\rm moon}/R_H$ in our simulations is seen to coincide with the upper third of the values exhibited by solar system moons; semi-major axes of $a/R_H = [0.04, 0.4]$ includes most of Jupiter's and Saturn's moons, but not the majority of Uranus' or Neptune's moons (Figure 2.10).

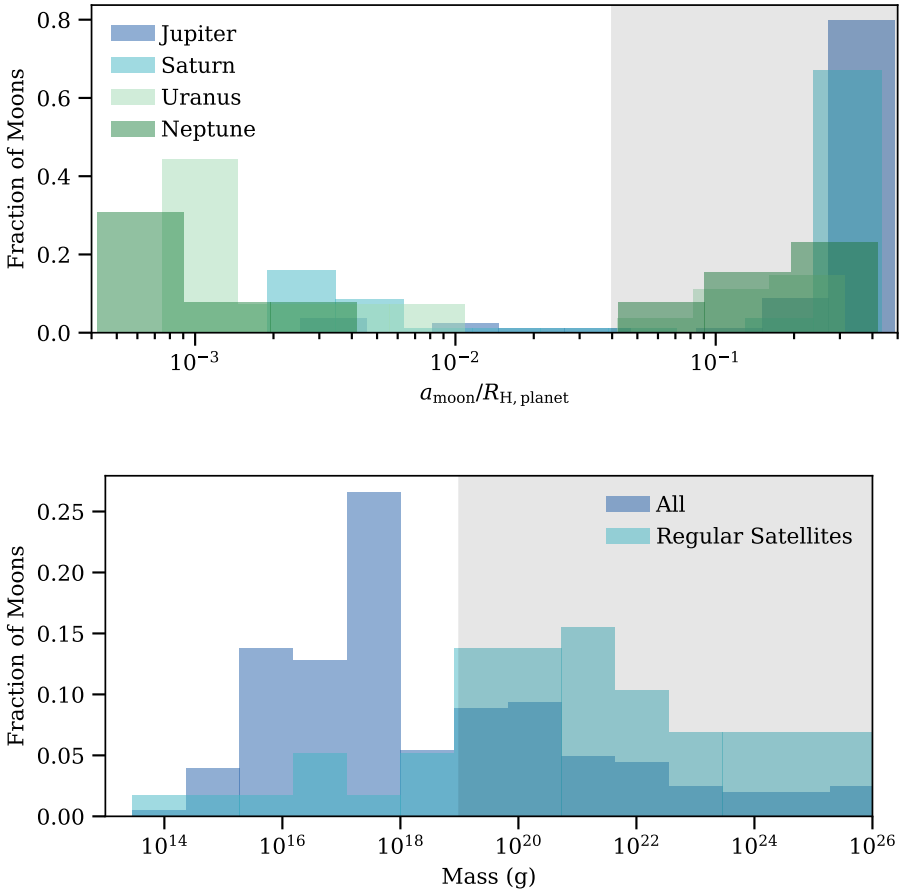

Figure 2.10: Top: Distribution of moon semi-major axes relative to the planet hill radius, for each of the giant planets. Bottom: Distribution of moon masses, including and excluding the irregular satellites. Regular satellites tend to have smaller semi-major axes and larger masses than the irregulars. The shaded portions of each graph show the approximate range of initial semi-major axes that can result in liberated moons (top) and the range of moon masses that can produce observable levels of pollution (bottom), according to our model.

2.4.4 Accretion Rates of Liberated Moons

Figure 2.11 shows an example of the results from one simulation. The lower plot shows the instantaneous periapse of each moon, while the upper figures show snapshots of the orbital configurations. In this simulation, the closest approach of a moon to the WD is ~ 0.007 AU. Table 2.2 lists the closest approaches of each of the moon test particles across all simulations, as well as the initial conditions for each moon's orbit, relative to its host planet.

Of the 60 moons comprising 10 simulations, one enters the Roche limit ($\lesssim$0.005 AU) of the white dwarf within the first 200 Myr after white dwarf formation. We therefore set the accretion rate of liberated moons at 1/60 per 200 Myr after the formation of the host WD. Note that like the asteroid N-body results, the moon accretion rates are dependent on the number of bodies available in the system. Our result should be taken as the fraction of liberated moons that accrete.

In our simulations, all moons are liberated from their host planets. Consistent with Payne et al. (2017), as a conservative estimate, we assume that any objects outside of $0.04R_{\rm H}$ of their planet will be liberated. We therefore take the population of solar system moons with semi-major axes in this range as the population of potential moon parent bodies that could pollute a WD. In our solar system, out of a total of about 200 moons, 145 are situated at more than 0.04 $R_{\rm H}$, including the irregular satellites.

Because moon accretions are single events, we can use the J09 accretion model to set a lower limit on the mass of a moon that can provide the minimum observable mass. For the DA of 10000 K, the least massive observable parent body is 1.3×10^{19} g and for the 14000 K DB the limit is 1.7×10^{20} g. For the population of solar system moons exterior to our limit for liberation of $0.04R_{\rm H}$, this gives a total of 22 moons that can provide observable pollution on a DA and 10 that can do so on a DB.

We now return to our expression for the frequency of moon accretions, $f_{\rm moons}$ as $N_{\rm moons} \times$

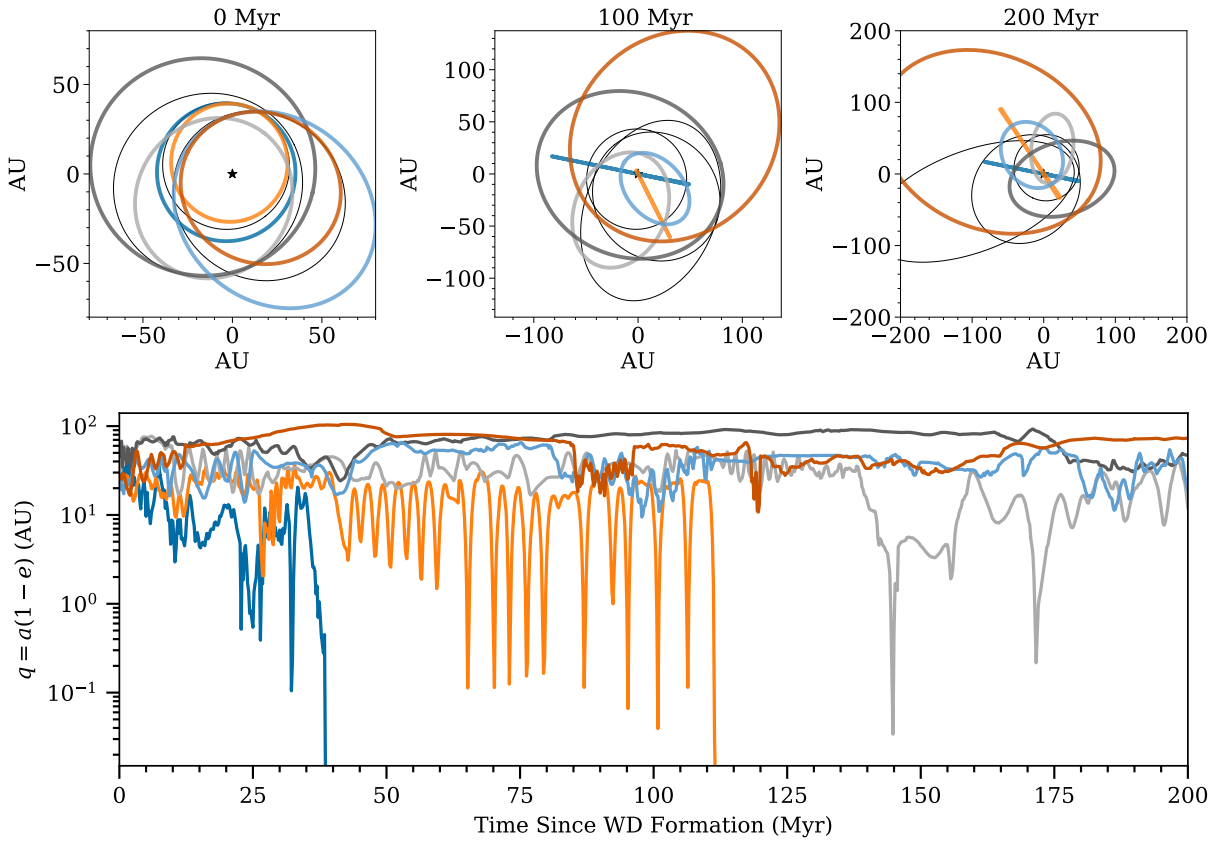

Figure 2.11: Top: Snapshots of orbits from simulation, for planets (thin black lines) and moons (colors). The times indicate the time since the WD formed, and the WD is shown as a black star at 0 AU. Bottom: Periapse versus time for the moons, in the same simulation as show in the top plot. Each curve corresponds with the orbits of the same color in the top plot. Two moons are scattered onto hyperbolic orbits following a close approach to the WD.

Table 2.2: Minimum periapse (q) reached by each moon, in AU, and the parameters used to initialize the moon orbits. $a_{\rm moon}$ is given relative to the Hill radius of the planet. Two moons were inserted around each planet. The WD Roche limit is at 0.005 AU.

Run	$a_{\rm moon}/R_{\rm H}$ range	$q1_{\rm min}$ (AU)	$q2_{\rm min}$	$q3_{\rm min}$	$q4_{\rm min}$	$q5_{\rm min}$	$q6_{\rm min}$
1	0.004-0.4	0.0612	0.0148	0.0060	20.1982	0.0018	0.0568
2	0.04-0.4	0.6077	4.7049	0.0619	6.6298	7.5362	2.4578
3	0.004-0.4	0.2180	0.1425	0.4133	1.5700	0.0328	0.8134
4	0.004-0.4	0.0078	0.0081	7.9765	0.6881	0.0187	0.0066
5	0.004-0.4	0.9560	1.8188	0.8765	0.0097	3.7238	0.0070
6	0.04-0.4	23.2735	22.1167	15.3154	4.8946	18.0538	17.4935
7	0.04-0.4	19.7743	33.2792	28.4050	19.1263	7.7563	31.6862
8	0.04-0.4	15.2427	11.6404	8.7045	20.0703	7.2406	26.1100
9	0.04-0.4	0.0069	0.0071	0.0341	24.2026	9.4522	10.7774
10	0.04-0.4	8.4775	21.0213	8.5416	0.0065	44.6118	27.5651

$f_{\rm accrete}$. We found that 1/60 of moons liberated from their host planets are expected to find their way to the WD. Inserting the accretion rate from the N-body simulations, and considering the number of moons that can both be accreted and observed on the surface of the WD based on the solar system population of moons, gives $f_{{\rm moons},DA} = 22 \times 0.017/200{\rm Myr} = 0.0019{\rm Myr}^{-1}$ and $f_{{\rm moons},DB} = 10 \times 0.017/200{\rm Myr} = 0.0009{\rm Myr}^{-1}$.

2.4.5 J09 Model for Moons

Applying the accretion rates of $f_{{\rm moons},DA} = 0.0019{\rm Myr}^{-1}$ and $f_{{\rm moons},DB} = 0.0009{\rm Myr}^{-1}$ results in 0.38 and 0.17 accretions in the first 200 Myr past WD formation, for the DA and DB WDs, respectively. One concludes that moons are expected to be visible as single accretion events, with no build up of pollution from multiple objects, unlike the case for asteroids.

We use solar system moons as a guide for computing the median mass expected for accretion events with moons as parent bodies. In the previous section, we showed that only moons with total masses greater than 1.3×10^{19} g and 1.7×10^{20} g can be detected on the surface of a DA and DB, respectively. In order to obtain the population of observable moons, we therefore select the solar system moons that are above these mass limits, and are situated outside of our assumed liberation limit of $0.04R_{\rm H}$. We assume the resulting moons represent the population of bodies that could both be liberated from their host planets and provide a detectable amount of pollution if they were to be accreted by their host WD. Recall that we found that 22 solar system moons meet these requirements for the DA accretion events and 10 solar system moons for the DB accretion events. Assuming any of these moons would be equally likely to accrete, we used the median mass moon of each population to represent the median mass moon expected to be observed accreting onto each WD type. This results in a median mass for an observed accreted moon on a DA of 1.2×10^{20} g and 3.7×10^{21} g for a DB.

In the lower panels of Figure 2.9, we show the pollution curve due to accretions of these median mass objects on the same time axis as the asteroid accretions to illustrate how the single events compare with the continuous accretions. We assume that each moon has chondritic composition. Because these are single events, they follow the same phases of accretion as shown in Figure 2.1, however we now also show the variation in the abundances of individual elements. The heavy metal limit outlined in Section 2.3 is shown as a horizontal line in each plot.

For a single moon accretion, the DA case exceeds the mass limit for 0.57Myr while the DB is observable for 3.89Myr. Note that these timescales far exceed the duration of observability for a single asteroid on either WD type. However, because asteroid pollution accumulates from multiple bodies, the continuous asteroid calculations result in greater cumulative timescales of observability.

For a mean fraction of observable time for the moons we multiply these numbers by the expected number of moon accretions in the 200 Myr time period for each case, obtaining $T_{\mathrm{moons},DA} = 0.38$ accretions $\times$ 0.57Myr/200Myr $= 0.001$ and $T_{\mathrm{moons},DB} = 0.17$ accretions $\times$ 3.89Myr/200Myr $= 0.003$.

We can now use our results to evaluate the relative probabilities of detecting asteroids from a debris belt and moons in polluted WDs.

Returning to Equation 2.1, we now fill in the values derived for the DA and DB cases to find the relative probability of observing accretion of moons and asteroids, yielding

$$\left(\frac{P_{\text{moon accretion}}}{P_{\text{asteroid accretion}}}\right)_{\text{DA}} = \frac{0.001}{0.145} = 0.007 \tag{2.6}$$

and

$$\left(\frac{P_{\text{moon accretion}}}{P_{\text{asteroid accretion}}}\right)_{\text{DB}} = \frac{0.003}{0.360} = 0.008. \tag{2.7}$$

Therefore, for three-planet Super-Earth/Neptune systems with both moons and asteroids available for accretion, we would only expect up to 1% of polluted DAs and DBs to currently have observable amounts of pollution due to moon accretion.

2.5 Discussion

Over 1000 white dwarfs have observations of at least one polluting element in the atmosphere (Coutu et al., 2019). Around 20 are considered strongly polluted, with multiple rock-forming elements detected. Therefore, $\sim 2\%$ of all polluted WDs can be considered 'highly polluted'. The large, moon-like mass solutions calculated in Section 2.2 represent the parent bodies associated with this highly polluted sample. Assuming that all of these high-mass parent bodies are indeed moons, this suggests that $\sim 2\%$ of polluted white dwarfs are accreting moons. Of course, as shown by the pollution masses in Figure 2.9, accretion of the most

massive asteroids may also result in high masses of pollution, so the population of the most highly polluted white dwarfs may also include the most massive debris belt members. Nonetheless, this statistic is consistent with our results derived from N-body accretion rates, that $\sim 1\%$ of overall pollution is expected to come from moons as opposed to less massive debris belt objects.

Uncertainties in this study include the timescales assumed in the J09 model, observational constraints beyond what has been considered in our minimum detectable mass method, exoplanet moon and asteroid populations, and the effects of planetary architectures beyond the three-planet system considered as our test case. We now explore these various possibilities and their effects on the parent body solutions or numerical accretion models.

2.5.1 Disk e-folding timescale

The e-folding lifetime of the debris disks around the WDs, $\tau_{\rm disk}$, determines how quickly pollution accretes onto the WD and, in conjunction with the settling times, limits the maximum mass of any given element that can accumulate in the WD atmosphere (Figure 2.2). Throughout the asteroid and moon comparison in this paper we assume $\tau_{\rm disk} = 10^5$yr, as an accommodation for estimates that span from 10^4 to 10^6yr.

In Section 2.2 we derived $t_{\rm min}$, the assumed elapsed accretion time which recovers a minimum solution for the parent body mass, or equivalently the steady state point in the J09 model. Plugging in $t_{\rm min}$ to the J09 model, we can therefore write the general solution for the minimum parent body mass solution relative to the observed mass in the atmosphere as a function of the ratio of the disk and settling timescales, for an arbitrary element:

$$\frac{M_{\rm PB}(Z, t_{\rm min})}{M_{\rm CV}(Z)} = \frac{\frac{\tau_{\rm disk}}{\tau_{\rm set}} - 1}{\left(\frac{\tau_{\rm disk}}{\tau_{\rm set}}\right)^{\frac{1}{1-\tau_{\rm disk}/\tau_{\rm set}}} - \left(\frac{\tau_{\rm disk}}{\tau_{\rm set}}\right)^{\frac{1}{\tau_{\rm set}/\tau_{\rm disk}-1}}}, \tag{2.8}$$

where $M_{\rm PB}(Z, t_{\rm min})$ is the parent body solution assuming steady state for the element Z and

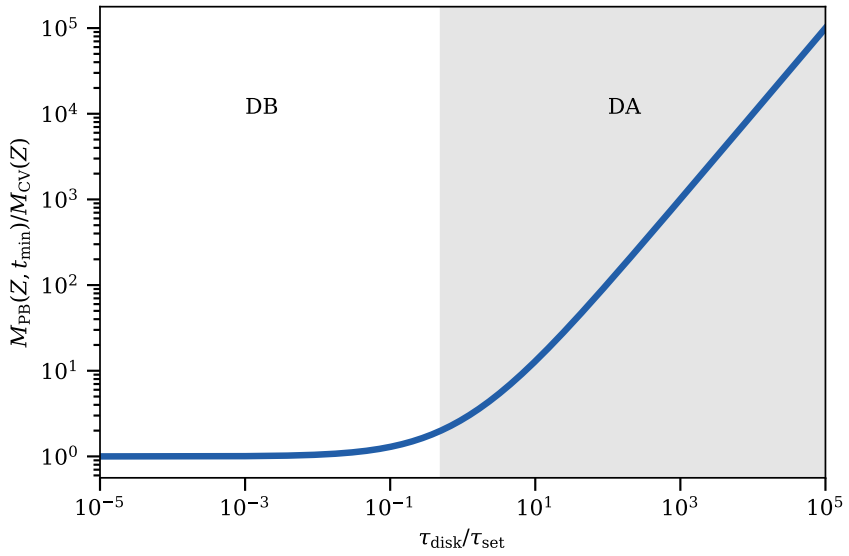

Figure 2.12: Minimum parent body mass solution relative to the observed mass of pollution in the atmosphere, as a function of the ratio of the disk timescale to the settling time. DAs would be found towards the right, so that the steady-state parent body mass is several times the observed mass in the atmosphere. DBs would be towards the left, where the parent body solution approaches the mass of the polluting metals.

$M_{\rm CV}(Z)$ is the observed mass of the heavy metal. Figure 2.12 shows Equation 2.8 applied to a range of disk-to-settling time ratios.

Writing the parent body mass expression in terms of the ratio of characteristic timescales shows why DAs and DBs have different sensitivities to changes in $\tau_{\rm disk}$ (outlined in Section 2.2) by illustrating the two limits of the parent body mass calculation. If disk timescales far exceed settling times, as they would for DAs, the minimum parent body solution will increase rapidly. For $\tau_{\rm disk} = 10^5$ yr and a DA settling time of days, parent body solutions can reach factors of 10^7 times the observed metal mass. On the other hand, if settling times exceed disk timescales, as they may for DBs, $\tau_{\rm disk}/\tau_{\rm set}$ approaches 1, so that the minimum parent body mass is equal to current mass of metal in the WD atmosphere.

Increasing the assumed disk timescale would shift parent body mass solutions to the right

in Figure 2.12. While DB WDs with very long settling times would not be strongly affected (parent body solutions would still be roughly equivalent to the mass of metal in the atmosphere), minimum parent body solutions trend approximately linearly with $\tau_{\rm disk}/\tau_{\rm set}$ when the disk timescale exceeds the settling time (DAs). Decreasing the assumed disk timescale would similarly not strongly affect the DBs but would decrease the parent body solutions of the DAs proportionally. Note that WDs with settling times within the range of disk timescale estimates will have non-linear dependencies on disk timescale. These effects can be seen in the parent body solutions calculated for the observed WDs (Figure 2.5).

We now return to our parameters $T_{\rm moons}$ and $T_{\rm asteroids}$, the timescales during which pollution exceeds detectable levels. For simplicity, we start by considering a single accretion with a generic observability timescale T. For a single event, T depends on the peak mass of pollution ($M_{\rm CV}$) that can build up in the atmosphere, the duration for which a high mass of pollution can be sustained, and the detection limit associated with the WD.

The maximum mass of pollution deposited by a given parent body mass is the inverse of Equation 2.8. Therefore, pollution accumulation for DAs varies inversely with changing disk timescales while peak masses of pollution in DBs remain roughly constant. The amount of time that relatively large masses of pollution can be sustained in the WD atmosphere can be approximated as the difference between $\tau_{\rm disk}$ and $\tau_{\rm set}$. As seen in Figure 2.4, these timescales are on either side of $t_{\rm min}$, where the maximum $M_{\rm CV}$ is reached. For simplicity, we will consider DA settling times well below, and DB settling times well above, the range of possible disk timescales, so that $|\tau_{\rm disk} - \tau_{\rm set}|$ will be approximately equal to the longest of the two timescales.

Based on this approximation, for DBs $|\tau_{\rm disk} - \tau_{\rm set}| \sim \tau_{\rm set}$, and to a reasonable approximation, changing $\tau_{\rm disk}$ should not affect T for the DBs. Therefore, and we anticipate $T_{\rm moons}$ and $T_{\rm asteroids}$ to be robust against disk timescales for DBs of sufficiently long settling times.

DA settling times are short, so $|\tau_{\rm disk} - \tau_{\rm set}| \sim \tau_{\rm disk}$, and increasing the disk timescale will lengthen the amount of time that peak pollution levels can be sustained. However, increasing $\tau_{\rm disk}$ decreases the maximum mass of pollution that can be accumulated. If the decreased pollution masses still exceed the detection limit, then T would increase, but if the new pollution masses do not exceed detection limits, T would fall to zero. The overall effect on $T_{\rm moons}$ and $T_{\rm asteroids}$ will therefore depend on the detection limits and distribution of debris belt masses considered. For our distributions of moons and asteroids, generally only the most massive bodies are contributing towards observable pollution, so assuming that most pollution would remain above the detection threshold, we would expect $T_{\rm moons}$ and $T_{\rm asteroids}$ to increase with increases in disk timescale.

2.5.2 Asteroid belt mass and size distribution

The accretion rate extrapolated from N-body simulations depends on the number of objects in the asteroid belt, which in turn depends on the total mass and assumed distribution of radii for the population of asteroids. Furthermore, the number of bodies contributing to heavy element pollution at any given time, and therefore the median mass of heavy elements in the WD convection zone, varies directly with the accretion rate. In this work, we assumed a solar system mass asteroid belt, with radii spanning $0.5 - 500$ km following a distribution of $dN \propto r^{-3.5} dr$.

Due to the continuous nature of asteroid accretion, pollution remains at a relatively stable minimum for the duration of accretion ($\sim 10^{16}$ g total in the DA, $\sim 10^{20}$ g for the DB), with short spikes to greater, observable masses when a particularly massive asteroid accretes. Whether asteroid accretion is observable for long time periods is therefore an 'all or nothing' issue, and is very sensitive to how a typical amount of accumulated heavy elements compares to the detection limit. If the limit is just above the typical mass that can build up from multiple accretions, we will observe only the peaks of the most massive asteroid accretions. However, if the detectability limit is just below the typical mass of accumulated metals,

accretion is observable for the entire time period.

Given that many polluted white dwarf progenitors are estimated to be more massive than the Sun (Coutu et al., 2019), it is reasonable to assume that many of these systems may have had debris belts more massive than the asteroid belt. If the debris in these more massive belts follows the same collisionally-produced power-law distribution as described for the asteroid belt, there would be correspondingly more objects of any given mass. Assuming the accretion rates per number of available bodies is unchanged, a larger debris belt would increase the total number of accretion events, and therefore increase the typical pollution mass at every point in time, resulting in a larger $T_{\rm asteroids}$. If the moon accretions remain unchanged, this increase in $T_{\rm asteroids}$ would decrease the fraction of pollution that would be due to moons.

2.5.3 The impact of planet spacing on moon liberation

Because moon liberations depend on close encounters between planets, and planet separations determine how quickly systems can become unpacked during stellar evolution, we expect the frequency of moon liberations to vary with planetary system architectures. The three-planet system used throughout Section 2.4 has spacings of 5-7 mutual Hill radii, with the innermost planet situated at 10 AU. This arrangement of planets is somewhat more tightly packed than most observed systems. Separations for systems detected by the *Kepler* satellite generally peak around 14-20 mutual Hill radii (Pu & Wu, 2015; Weiss et al., 2018), however these observed planets are all on orbits interior to ~ 2 AU, and it is unclear if this trend would directly apply to outer planets.

One constraint on outer planet spacings is HR 8799 (Marois et al., 2008, 2010), which hosts four giant planets ($> 5M_{\rm Jup}$) exterior to 10 AU, and is a likely candidate for a future polluted white dwarf system (Veras & Hinkley, 2021). Considering the most stable configuration for these planets (Goździewski & Migaszewski, 2020), separations are approximately 2-3

mutual $R_{\rm H}$. From the sample of directly-imaged exoplanets, Nielsen et al. (2019) found that approximately 9% of stars more massive than $1.5 M_{\odot}$ could host such massive planets outside of 10 AU.

In Figure 2.13 we show the orbital crossings that result in simulations with initial planet spacings of 5-10, 10-20 and 20-30 mutual Hill radii. Planet masses for all three simulations are 1.3, 30.6, and 7.8 $M_{\oplus}$, the same as used in Section 2.4. These simulations result in 502, 148, and 173 crossings for the 5-10, 10-20, and 20-30 cases, respectively. We find that while the number of crossings varies with planet spacings, crossings do still occur even at spacings more consistent with the majority of observed systems. From this simple comparison we do not anticipate that orbital crossings, and consequently moon liberations, would be entirely eliminated for more widely separated systems. Further study is necessary for more detailed connections between liberations and accretions and planetary architectures.

2.5.4 Populations of exomoons

In this paper, we assumed that moon populations would be similar to those in the solar system. It is possible that moon populations in exoplanet systems do not resemble the solar system. However, as there are no confirmed detections of rocky or icy exomoons, it is difficult to determine how many such moons a typical exoplanet system might have. Additionally, if exomoons in general are not found in all planetary systems, the probabilities of moon accretions derived in this work should be multiplied by the fraction of polluted white dwarf systems that do host exomoons.

A first-order limit on the number of moons in a given WD system should be the placement of moon-hosting planets. Dobos et al. (2021) found that whether exomoons can survive in a stable orbit around a given planet depends on the proximity of the planet to the host star. They conclude that planets on very short period orbits (< 100 days) are most limited in the fraction of moons they can retain, while planets with longer periods could retain at

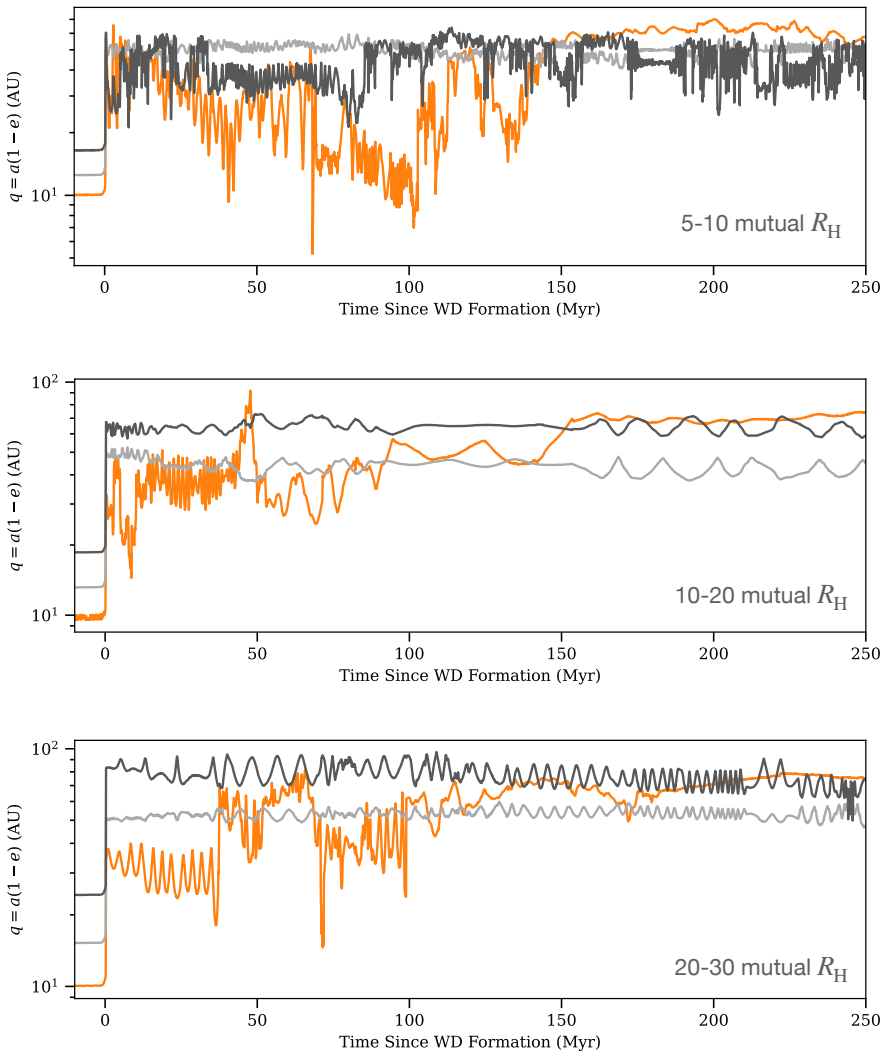

Figure 2.13: The periapse evolution of three-planet systems for three different ranges of planet spacings in terms of mutual Hill radii: 5-10 (top), 10-20 (middle), and 20-30 (bottom). In each system, the innermost planet is at 10 AU and the spacings between each consecutive planet are randomly chosen from the stated ranges. Planet masses for all three simulations are 1.3, 30.6, and 7.8 $M_\oplus$. While the most closely packed system experiences the most orbital crossings between planets, crossings still occur in the more widely spaced systems.

least 60% of their original moons. For the purposes of determining the populations of moons available to accrete onto a WD, the longer-period planets are likely more relevant, as the inner planets risk being engulfed by the star in its red giant phase.

In our three-planet system, planets were originally located 10-13 AU around a $3M_{\odot}$ star, with periods of $18-27$ years. According to the Dobos et al. study, these planets could retain about 70% of their moons. The giant planets of the solar system have orbital periods of about 11 to 160 years, and have a similar moon retention fraction of $60-80\%$. This suggests that whether or not the distributions in mass and semi-major axis of moons in our theoretical three-planet system match those for our solar system's moons, systems resembling our three-planet system should have a large portion of their moons intact and bound to planets when the white dwarf forms. Further constraints on exomoon populations could be made as Transit Timing Variation searches for exomoons progress (e.g., Teachey & Kipping, 2021; Kipping, 2021).

2.6 Conclusions

Motivated by the large parent body masses required to explain observed levels of white dwarf pollution, and the recent discovery of beryllium in a white dwarf atmosphere, we have used N-body simulations and the Jura et al. (2009) accretion model to assess the likelihood that a WD will be polluted by a moon. We focus this study on the first 200 Myr past WD formation for a planetary system containing three Super-Earth/Neptune-class planets. Extrapolating from asteroid N-body simulations, we find that such a planetary system could sustain an asteroid accretion rate of approximately 1200 objects per Myr. Assuming that the system had a population of moons similar to the regular solar system moons, we find from N-body simulations that we could expect up to about 0.4 moon accretions per 200 Myr.

Using the population of observed white dwarfs with calcium detections, we find that the pollution must have a calcium mass component of at least 5.8×10^{14} g to be observable in a

DA atmosphere, and 1.4×10^{18} g to be detected in a DB. We use these limits to determine the cumulative fractions of time that moons and asteroids can produce observable levels of pollution. Based on our numerical accretion model, we expect $\sim 1\%$ of white dwarf pollution to come from moons as opposed to asteroids. If we consider, as a first-order approximation, that all of the most highly polluted WDs (requiring the most massive parent bodies) are polluted by moons, our parent body mass approach returns a similar statistic, of moons making up about 2% of polluters.

CHAPTER 3

A Chondritic Solar Neighborhood

3.1 Introduction

The growing sample of exoplanets has inspired many studies detailing their compositions and interiors. Analyses of exoplanet compositions using mass and radius relationships or through extrapolating stellar abundances have led to a wide range of possible exoplanet compositions (Bond et al., 2010), including Earth-like compositions, but also carbon-rich planets (e.g. Dorn et al., 2019), coreless super-Earths (e.g. Madhusudhan et al., 2012), and mineralogies with no Earth-rock counterparts (Putirka & Xu, 2021). This hypothesized diversity of exoplanet compositions motivates us to benchmark the variety of putative non-Earth like planets against the compositions of exoplanetary rocks accreted by polluted white dwarfs (WDs). The metal pollution on WDs is caused by accretion of exoplanetary debris and provides direct measurements of bulk compositions of extrasolar rocks that are not susceptible to the same degeneracies as the mass/radius approach (e.g. Dorn et al., 2015). The vast majority of WD pollutants are rocky, with some fragments identified as specifically core or crust-like (e.g. Doyle et al., 2019; Harrison et al., 2018; Hollands et al., 2018; Melis & Dufour, 2017; Jura & Young, 2014). Some water-rich objects have also been identified, with possible parent bodies including Kuiper Belt analogs or exomoons (e.g. Doyle et al., 2021; Klein et al., 2021; Hoskin et al., 2020; Xu et al., 2017; Raddi et al., 2015).

We analyze the abundances from 31 oxygen-bearing polluted WDs. The presence of O,

along with other major rock-forming elements such as Si, Mg, and Fe indicate that these WDs are accreting rocky material. We compare the abundances of the WD pollution to rocks throughout the solar system, an approach motivated by previous WD studies (e.g. Doyle et al., 2023; Swan et al., 2019; Xu et al., 2013). We also carry out the same analysis for local stars, as a proxy for protostellar disk environments and as a broad representation of the system's rocky planet compositions (e.g. Schulze et al., 2021). For this purpose, we use the Hypatia catalog of stars, which includes elemental abundances for thousands of stars within ~ 500 pc of the Sun (Hinkel et al., 2014). Throughout, we compare WD and stellar compositions to solar system rocks using a reduced chi-squared goodness-of-fit test.

While individual stars may show unusual amounts of particular elements, we find in this work that the majority of WD pollution is indistinguishable from chondrites in composition, when accounting for uncertainties in the measured abundances. The whole-rock compositions of CI chondrites are considered a proxy for the relative abundances of rock-forming elements of the solar system, as they are the best compositional match to the Sun (e.g. Lodders et al., 2009; Anders & Grevesse, 1989), and we use them here as representative of chondrites in general.

This paper is organized as follows. In Section 3.2 we outline the χ^2 calculation used to test the goodness of fit of each set of abundances to CI chondrite. To demonstrate the method, we apply the χ^2 test to solar system rocks in Section 3.3. We then carry out fits for the WD polluters in Section 3.4 and for the Hypatia catalog stars in Section 3.5. We discuss the impact of galactic chemical evolution on polluted WD and Hypatia compositions in Section 3.6 and present our conclusions in Section 3.7.

3.2 Methods

Throughout this work we compare observed abundances to the CI chondritic composition (Lodders, 2019) by computing reduced χ^2 values (χ^2_ν). Measurement uncertainties for the

WDs are propagated using a Monte Carlo approach. Uncertainties for the Hypatia catalog stars are gathered from the catalog (Hinkel et al., 2014). For each star, we use the relative concentrations of Si, Fe, Al, Ca, Ni, and Cr, where available, all normalized to Mg. We do not include more volatile elements such as C, N, or O in the comparisons as we are primarily concerned with rock compositions in this work. Because a very diverse range of physical processes can vary volatile abundances during planet formation (e.g. Bonsor et al., 2021), volatile abundances are not necessarily related to rock compositions. Excluding these elements therefore allows for more direct comparison of the underlying rock to solar system samples. Additionally, while O is a major element in rocks, its abundance is correlated with the other included rock-forming elements in oxides, providing further motivation to exclude it from the χ^2_ν calculations.

Starting with log abundances for each star and WD, we construct a random sample of abundances for each element assuming a normal distribution based on the reported logarithmic abundance ratios and their uncertainties. We then transform the distribution of logarithmic relative abundances to a distribution of number ratios for each element relative to Mg. The reported symmetric errors in the logs lead to asymmetric distributions in number ratios, so we select our assumed abundance ratios and uncertainties as the median, 16.5, and 83.5 percentiles from the distributions. Errors in ratios of elements are obtained by propagation of uncertainties in the individual elements using Monte Carlo sampling. To address the asymmetric uncertainties in the ratios of elements arising from reported symmetric errors in logs of the ratios for both the WDs and Hypatia catalog stars, we use the following equation to calculate the χ^2 goodness of fit for each element i relative to Mg:

$$\chi^2_i = \left(\frac{\delta_i}{\sigma_i}\right)^2 \left(1 - 2A\frac{\delta_i}{\sigma_i} + 5A^2\left(\frac{\delta_i}{\sigma_i}\right)^2\right), \tag{3.1}$$

where δ_i is the difference between the observed and expected element ratio, σ_i is the average of the upper and lower errors, and A describes the asymmetry in the errors as $A = (\sigma_+ -$

$\sigma_-)/(\sigma_+ + \sigma_-)$, where σ_+ and σ_- are the asymmetrical measurement uncertainties for element i (Barlow, 2003). To find the reduced χ^2, we sum over all elements and divide by the degrees of freedom, taken to be the number of elements (excluding Mg) measured for the given star.

We define the passing conditions (accepting the alternative hypothesis H_a that the rocks are chondritic) for the χ^2_ν tests using the parameter α, the probability of randomly obtaining a χ^2_ν value greater than the one calculated for the observed abundances (e.g. the probability of incorrectly rejecting the null hypothesis, H_0, that the rocks are not chondritic). Following convention, we place the α limit at 0.05, so that any stars identified as chondritic compositions must have a χ^2_ν with an $\alpha < 0.05$, implying a $H_\mathrm{a} = 1 - \alpha$ probability that the correspondence with chondrite is not due to random chance.

Because our sample sizes are very small, we must account for errors in the χ^2_ν values. The error in χ^2_ν can be approximated as $\sigma = \sqrt{2/n}$ (Andrae et al., 2010), where n is the number of data points for a given star's composition. We therefore define the critical reduced chi-square values as $\chi^2_{\nu,\mathrm{crit}} = \chi^2_\nu(\alpha = 0.05) + 2\sqrt{2/n}$, allowing for a 2σ error in χ^2_ν. These constraints give critical χ^2_ν values of ~ 3 to 4, for n from $3-6$ (excluding Mg), varying inversely with the number of elements observed for each star. For a given star, if the elements available define $\chi^2_\nu \lesssim 3$ to 4, the data are taken as evidence for chondritic rocky parent bodies or planets.

In order to identify outliers in the elemental abundances for each WD and Hypatia star, we apply a Dixon's Q test (Dean & Dixon, 1951) with a confidence level of 95% ($p = 0.05$). We choose this test as it is best suited for small sample sizes. For this test we convert abundances to $(n_\mathrm{Z}/n_\mathrm{Mg})/(n_\mathrm{Z}/n_\mathrm{Mg})_\mathrm{CI}$ such that 1 represents a perfect fit to chondrite. Outlier elements are therefore the elements with the worst fits to chondrite (other than Mg), and we identify an outlier in six of the WDs. Stars which pass as chondritic when an outlier is ignored are considered "soft passes."

3.3 Solar System Rocks

To test our ability to differentiate between different rock types using the methods of Section 3.2, we first apply our test for chondritic compositions to rocks in the solar system, including bulk Earth (BE) and bulk silicate Earth (BSE, McDonough (2003)), mid-ocean ridge basalt (MORB), continental crust (CC, Rudnick & Gao (2003)), bulk silicate Mars (BSM, Taylor (2013)), and E chondrites (EH, Wasson & Kallemeyn (1988)). For each element, we apply the mean uncertainty calculated from our sample of WDs for that element, with the resulting uncertainties generally ranging from 0.15−0.30 dex.

We find that BE, BSE, BSM, and the E chondrites are indistinguishable from CI chondrites, while MORB and CC are very clearly not good matches to CI chondrite in these tests (Figure 3.1). Bulk Earth being indistinguishable from chondritic is in contrast with the distinction typically drawn between the two rock types in previous studies (e.g., Putirka & Rarick, 2019; Drake & Righter, 2002), and is the result of propagating the large uncertainties associated with the element ratios for the WDs compared with the comparatively small differences in composition among the rock compositions.

Throughout this work, we report compositions as consistent or inconsistent with chondrites, while recognizing that with current measurement uncertainties, chondrites, Earth, and Mars are all indistinguishable. However, this test is able to definitively differentiate between chondrite-like compositions and crust, the latter representing products of igneous differentiation of chondrites.

3.4 White Dwarfs

Our WD sample includes 31 WDs with detections of oxygen together with other rock-forming elements (Table 3.1). The vast majority of the WDs in our sample have atmospheres that are helium-dominated, and a handful are hydrogen-dominated. The WDs are all within

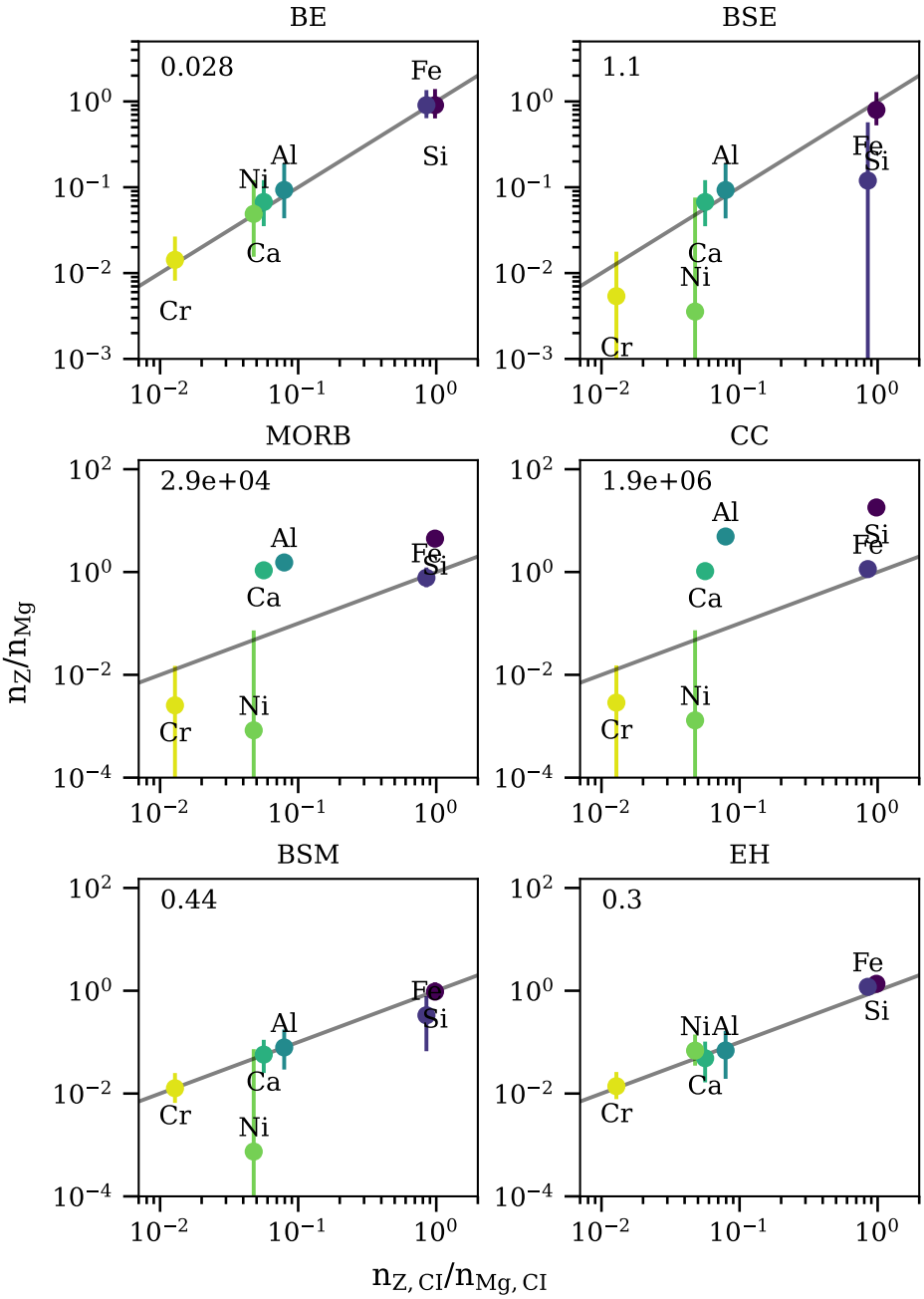

Figure 3.1: Compositions of solar system rocks compared to CI chondrite, for Bulk Earth (BE), Bulk Silicate Earth (BSE), Mid-Ocean Ridge Basalt (MORB), Continental Crust (CC), Bulk Silicate Mars (BSM), and E chondrites (EH). Error bars for each element correspond to the mean uncertainty in the WD abundances for that element. The reduced χ^2 value for each correlation with CI chondrite is indicated in the plots at the upper left. Where $\chi^2_\nu \lesssim 3$ to 4, the data are taken as evidence for chondritic rocky parent bodies or planets.

about 200 pc of the Sun. For each WD, we draw stellar properties, elemental abundances and uncertainties in abundances from the references listed in Table 3.1, supplemented by the Montreal White Dwarf Database (MWDD, Dufour et al. 2017). We use the elements Si, Fe, Al, Ca, Ni, and Cr where available. We ratio all abundances to Mg and propagate uncertainties using a Monte Carlo approach outlined in Section 3.2.

We analyze both the raw and steady-state adjusted abundances for the WD pollution. The steady-state adjustment accounts for differential settling rates for different elements in the atmosphere of a WD. Settling rates also depend on the dominate element in the atmosphere of the WD, and range from days to millions of years (Koester, 2009; Blouin et al., 2018). The steady-state settling factor we use is $(n_Z/n_{\rm Mg})_{SS} = (n_Z/n_{\rm Mg}) \times (\tau_{\rm Mg}/\tau_Z)$, where $\tau_{\rm Mg}$ and $\tau_{\rm Z}$ are the settling timescales for Mg and a given element Z, respectively. Settling timescales for the WDs in our sample are collected from the MWDD, using the WD parameters listed in Table 3.1. These adjustments are clearly necessary for the H-dominated WDs, where settling is generally much more rapid. Suitability of the adjustment to abundances in the He-dominated atmospheres is less clear. We note that the stated steady-state factor is a simplistic approach to account for settling, which does not account for potential effects such as mixing in the WD atmosphere (e.g. Bauer & Bildsten, 2019; Cunningham et al., 2019)

For each WD, we compare the abundances normalized to Mg to the abundances measured in CI chondrites following the method outlined in Section 3.2. Figure 3.2 shows this comparison for all WDs in our sample and for both the raw and 3.2 shows the steady-state adjusted values. Hydrogen-dominated WDs are marked with "H". From left to right on each plot, the element ratios are Cr/Mg, Ni/Mg, Ca/Mg, Al/Mg, Fe/Mg, and Si/Mg. The dark grey panels in Figures 3.2 and 3.3 indicate WDs which do not pass the χ^2_ν test for chondritic composition. The lighter shaded panels show the "soft pass" WDs, where ignoring an identified outlier allows the WD to pass as chondritic (see Section 3.2). Solar system rocks are shown for comparison (see Section 3.3 for discussion of solar system fits).

Table 3.1: All WD parameters are collected from the references listed in the table. Any values not reported by the paper have been supplemented using the Montreal White Dwarf Database (Dufour et al., 2017). Throughout this work we group WDs by the dominant element in their atmospheres (H or He-dominated only).

White Dwarf	Type	$T_{\rm eff}$ (K)	log(g)	D (pc)	M†($M_{\odot}$)	Reference
G29-38	H	11820	8.15	14	0.696	Xu et al. (2014)
SDSSJ1043+0855	H	18330	8.05	169	0.649	Melis & Dufour (2017)
PG1015+161	H	19226	8.04	88	0.645	Gänsicke et al. (2012)
WD1226+110	H	20900	8.15	129	0.714	Gänsicke et al. (2012)
WD1929+012	H	21200	7.91	53	0.578	Gänsicke et al. (2012)
PG0843+516	H	23095	8.17	139	0.730	Gänsicke et al. (2012)
WD0446-255	He	10120	8.00	91	0.581	Swan et al. (2019)
WD1350-162	He	11640	8.02	108	0.596	Swan et al. (2019)
WD1232+563	He	11787	8.30	172	0.773	Xu et al. (2019)
SDSSJ1242+5226	He	13000	8.00	161	0.587	Raddi et al. (2015)
SDSSJ2339-0424	He	13735	7.93	89	0.548	Klein et al. (2021)
SDSSJ0738+1835	He	13950	8.40	172	0.842	Dufour et al. (2012)
HS2253+8023	He	14000	8.10	72	0.648	Klein et al. (2011)
WD1425+540	He	14490	7.95	52	0.560	Xu et al. (2017)
WD1145+017	He	14500	8.11	146	0.655	Fortin-Archambault et al. (2020b)
GaiaJ0218+3625	He	14691	7.86	116	0.512	Doyle et al. (2023)
EC22211-2525	He	14743	7.90	109	0.534	Doyle et al. (2023)
WD2207+121	He	14752	7.97	164	0.572	Xu et al. (2019)
WD1551+175	He	14756	8.02	162	0.601	Xu et al. (2019)
WD1244+498	He	15150	7.97	164	0.573	Doyle et al. (2023)
WD1248+1004	He	15178	8.11	73	0.656	Doyle et al. (2023)
GD40	He	15300	8.00	120	0.591	Jura et al. (2012)
G241-6	He	15300	8.00	65	0.591	Jura et al. (2012)
GaiaJ1922+4709	He	15497	7.95	127	0.562	Doyle et al. (2023)
GD378	He	15620	7.93	44	0.551	Klein et al. (2021)
SDSSJ1734+6052	He	16340	8.04	150	0.616	Doyle et al. (2023)
GD61	He	17280	8.20	54	0.715	Farihi et al. (2013)
WD1415+234	He	17312	8.17	127	0.696	Doyle et al. (2023)
SDSSJ2248+2632	He	17369	8.02	123	0.606	Doyle et al. (2023)
Ton345	He	19780	8.18	106	0.706	Wilson et al. (2015)
WD1536+520	He	20800	7.96	201	0.578	Farihi et al. (2016)

† Masses are collected from the MWDD using the $T_{\rm eff}$ and $\log(g)$ values in the table.

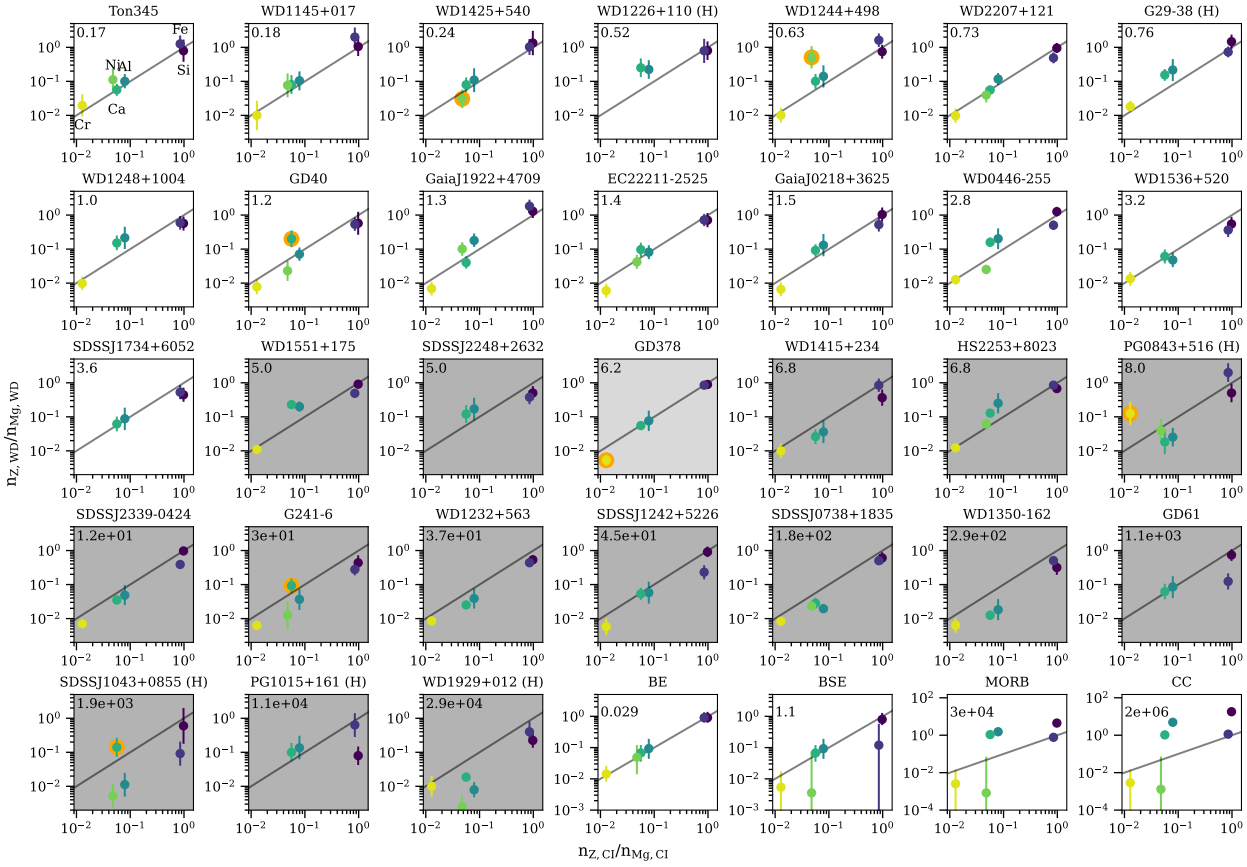

Figure 3.2: Comparison of WD pollution compositions to the CI chondrite composition, for the raw data. The order of elements in each plot, from left to right, is Cr, Ni, Ca, Al, Fe, Si, all ratioed to Mg. The χ^2_ν parameter appears in the upper left of each panel. WDs with white backgrounds are consistent with having accreted a chondritic rock composition. WDs with dark grey backgrounds are not considered a good fit to chondrite, using an α parameter of 0.05 for goodness of fit. WDs with light grey backgrounds have an outlier element that allows the WDs to pass as chondritic when the outlier is removed (outliers highlighted in orange).

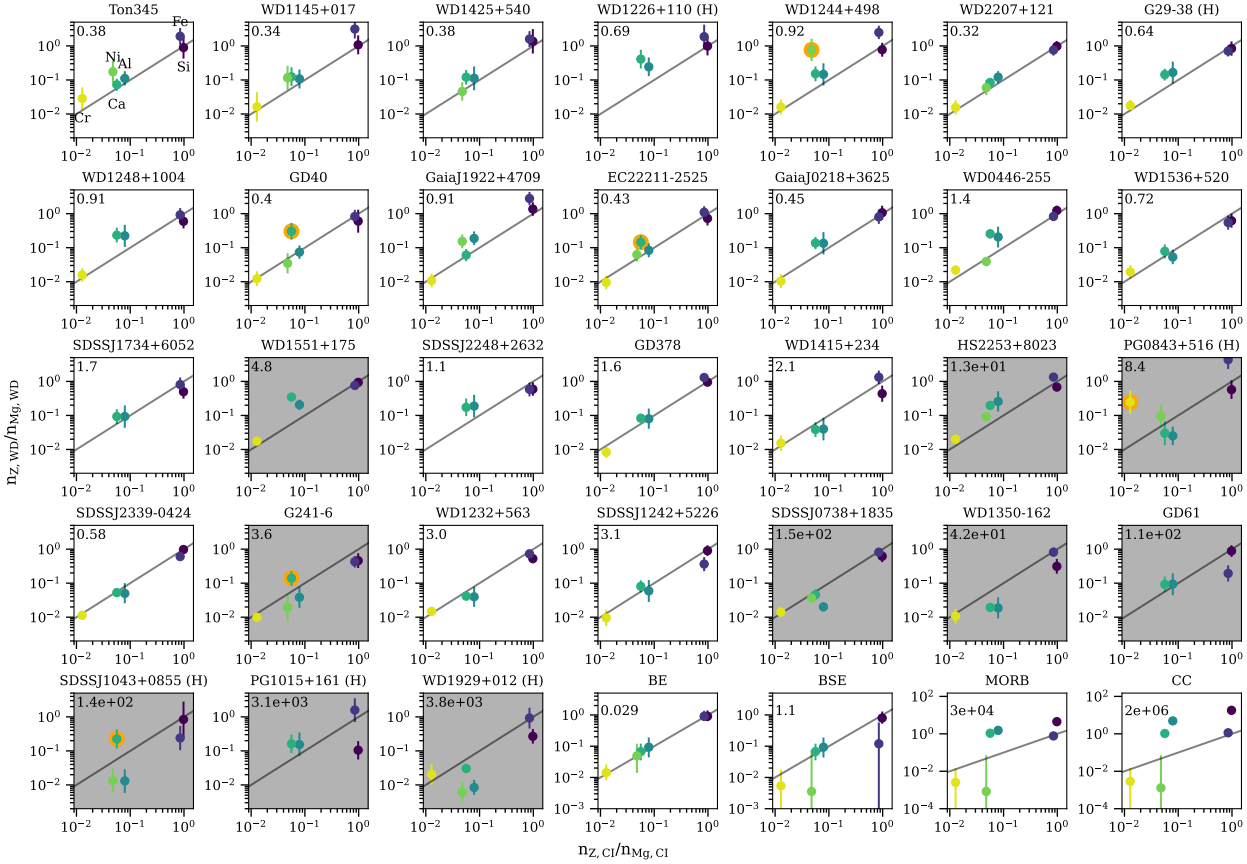

Figure 3.3: Same as Figure 3.2 for the steady-state adjusted abundances. The order of elements in each plot, from left to right, is Cr, Ni, Ca, Al, Fe, Si, all ratioed to Mg. The χ^2_ν parameter appears in the upper left of each panel. WDs with white backgrounds are consistent with having accreted a chondritic rock composition. WDs with dark grey backgrounds are not considered a good fit to chondrite, using an α parameter of 0.05 for goodness of fit. WDs with light grey backgrounds have an outlier element that allows the WDs to pass as chondritic when the outlier is removed (outliers highlighted in orange).

Figure 3.4 shows the χ^2_ν parameters for the WDs for the raw data versus steady-state abundances, separated by the dominant element in the WD atmosphere. We also group the WDs by the number of observed elements considered in the statistical comparison (n), to illustrate the dependence of χ^2_ν on n. Increasing n generally lowers both the calculated and critical χ^2_ν values. The condition for passing as chondritic at $n = 3$ is $\chi^2_\nu \sim 4.2$ and at $n = 6$ is $\chi^2_\nu \sim 3.3$.

We find that 15 of the 31 WDs pass the χ^2_ν test as good matches to chondritic composition when using the raw abundances. One additional WD passes as chondritic when its outlier element is ignored. A larger fraction of pollution passes as chondritic with the steady-state adjustment (21/31 pass). Because the steady-state adjustment does not improve the fits for every WD (Figure 3.4), some WDs that pass as chondritic using the raw data do not pass in the steady-state case. We note that a larger proportion of WDs passing as chondritic in the steady-state case does not *a priori* mean the WDs are most likely to be in the steady state phase of accretion. In any case, over half of the WDs in the sample are consistent with chondritic compositions using either the raw or steady-state compositions.

We find no compelling evidence for basaltic crust (MORB) or continental crust rocks among the polluted WDs. When carrying out the same χ^2_ν calculation for each WD relative to the other solar system rock types considered here (Section 3.3), no WDs are better fit by MORB or continental crust relative to CI chondrite, even those with χ^2_ν values relative to chondrite of 100 and greater.

3.4.1 White Dwarf Mineralogy Classification

In addition to the χ^2_ν test, we also follow the common practice of representing rock chemistries as “normative mineralogies" in which elemental concentrations are converted to volumetric fractions of fictive minerals (Cross et al. 1902, see also Putirka & Xu 2021 Supplement for details). We recast the WD pollution by projecting the observed abundances to a normative mineralogy composed of the relative abundances of Mg-endmember Olivine (OLV), Orthopy-

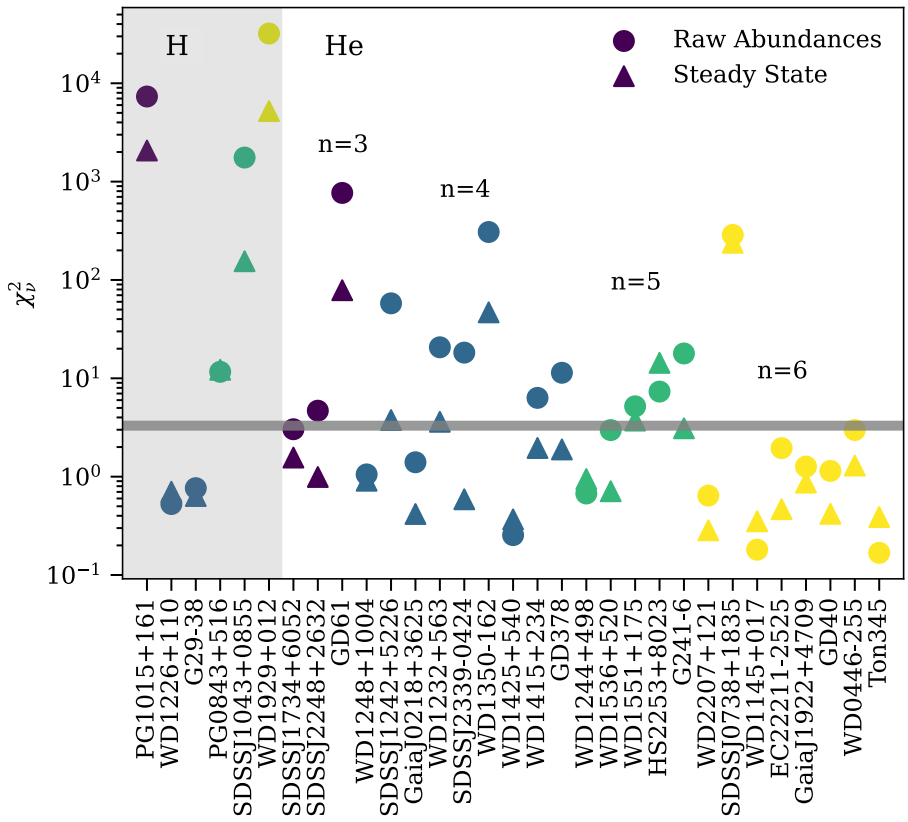

Figure 3.4: χ^2_ν for each WD, relative to CI chondrite, for the raw abundances (circles) and steady-state adjusted values (triangles). The points are colored and grouped by n, the number of elements used to calculate χ^2_ν. The horizontal line shows a typical critical χ^2_ν value ($\chi^2_\nu \sim 3$ to 4, based on the number of observed elements). In most cases, the steady-state values provide a better fit.

roxene (OPX) and Clinopyroxene (CPX). These minerals comprise a reasonable normative mineralogy used to classify ultramafic (e.g., peridotite) rocks, and chondrites are broadly similar to ultramafic rocks. The fractions of these minerals in terms of moles depend on the relative numbers of Mg, Si and Ca atoms comprising the rocks. By inverting the mineral formulae for these reference minerals where OLV = Mg_2SiO_4, OPX = $Mg_2Si_2O_6$, and CPX = $CaMgSi_2O_6$, one obtains the function that transforms relative atomic abundances of Mg, Si, and Ca to the relative molar abundances of the minerals, which in matrix form is

$$\begin{bmatrix} n_{\mathrm{OLV}} \\ n_{\mathrm{OPX}} \\ n_{\mathrm{CPX}} \end{bmatrix} = \begin{bmatrix} 1 & -1 & 1 \\ -1 & 2 & 3 \\ 0 & 0 & 1 \end{bmatrix} \times \begin{bmatrix} n_{\mathrm{Mg}} \\ n_{\mathrm{Si}} \\ n_{\mathrm{Ca}} \end{bmatrix}. \tag{3.2}$$

The molar abundances of the normative minerals are converted to approximate volume fractions (as is common for reporting rock mineralogies) using nominal molar volumes for OLV, OPX, and CPX, or 4.37, 6.26, and 6.60 J/bar (J/bar = 0.1 cm^3/mole). Fe and other less abundant elements are not included in this projection. Including Fe in this projection shifts the positions of the data somewhat, but does not substantially change the results.

Figure 3.5 shows the WD pollution represented as the relative volume fractions of OLV, OPX, and CPX implied by each composition. For each polluted WD, we take Monte Carlo draws of Mg, Si, and Ca using the reported values and corresponding uncertainties as the parent populations, and calculate the resulting normative mineral abundances. CPX is constrained only by the relative amount of Ca in the pollution, and exhibits comparatively little scatter as Ca uncertainties are generally small. We note that the volumetric fractions resulting from this method are not necessarily physical. Because this is a projection, some of the WD abundances result in negative amounts of OLV, OPX, or CPX, leading to scatter beyond the bounds of the positive ternary coordinate system. Putirka & Xu (2021) previously used this method to report exotic mineralogies for WD pollution, however we find that the uncertainties in Si and Mg are sufficiently large as to produce hopelessly large spreads in OLV

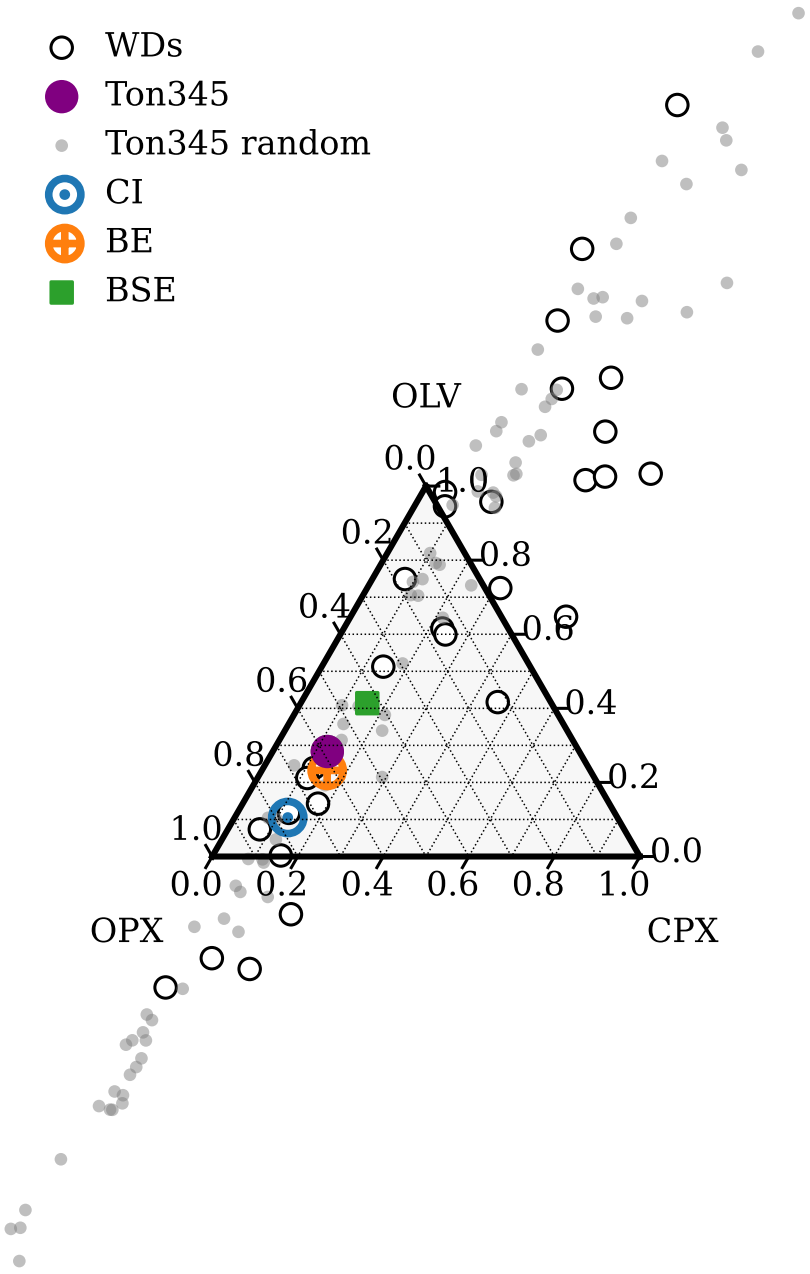

Figure 3.5: Ternary diagram for all of the WD samples, for raw abundances. The white points indicate the OLV, OPX, and CPX quantities derived from the median values of Mg, Ca, and Si for each WD. We also demonstrate the spread in OLV, OPX, and CPX that is due to the uncertainties in the WD abundances by showing the spread from 100 random draws of Mg, Si, and Ca for WD Ton345. The total spread in points is truncated for visibility.

and OPX abundances, so that it is impossible to constrain the mineralogy of the implied rocks (Figure 3.5). A similar spread in mineral abundances is derived from the steady-state data. We therefore conclude that categorizing rock pollution in WDs into rock types based on normative abundances of OLV, OPX, and CPX abundances, or similar normative mineralogies, is not possible.

3.5 Hypatia Catalog Stars

Our solar system exhibits a diversity of rock types originating from the same protoplanetary material, underscoring that samplings of rock can end up with very different compositions relative to the average starting material (e.g., crust vs. chondrites in Section 3.3). To benchmark the "final" exoplanetary rocks sampled by polluted WDs against protoplanetary material, we analyze the abundances of rock-forming elements in nearby stars by applying our compositional fitting method to stars in the Hypatia catalog (Hinkel et al., 2014). These stars should reflect protoplanetary material, to the extent that stellar abundances have been shown to broadly reflect compositions of planets around their stars (e.g. Thiabaud et al., 2015; Bonsor et al., 2021; Schulze et al., 2021). The stellar sample therefore represents a potential average of planet building materials, rather than the final rock compositions of individual rocky parent bodies sampled by the WDs.

We select Hypatia catalog stars with Mg and at least two other elements among Si, Fe, Al, Ca, Ni, or Cr. All uncertainties are obtained directly from the catalog, where they are listed as either the uncertainty reported in the original study or the mean uncertainty of multiple studies, where stars are observed by multiple methods.

Given the range of stars included in the Hypatia catalog, we explore how stellar type and distance may impact overall abundances. About 6500 stars in the catalog are classified as F, G, K, or M stars. In Figure 3.6, we show the range of distances from the Sun in each classification. M stars in the sample tend to be much closer to the Sun ($<\sim$ 50pc) compared

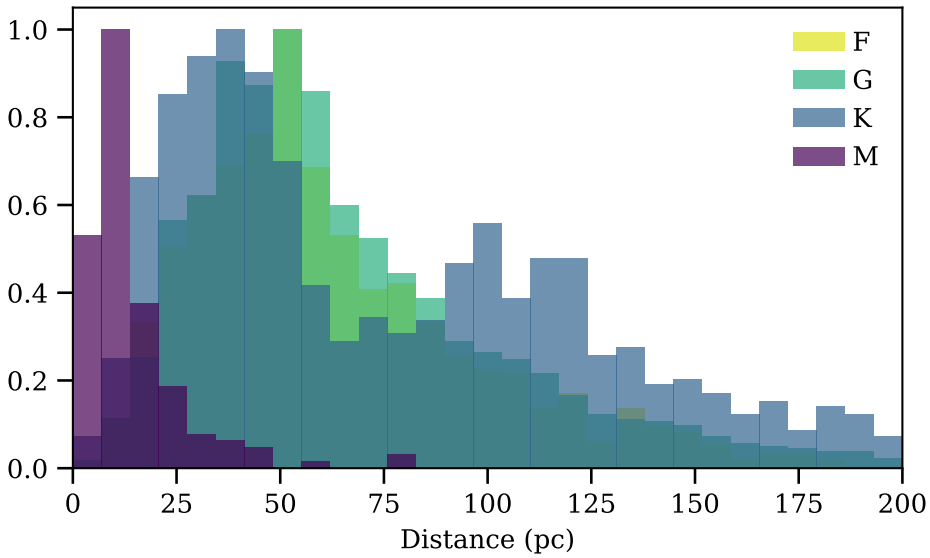

Figure 3.6: Distribution of the distances of Hypatia catalog stars from the Sun (classified by stellar type). M dwarfs in the sample tend to be much closer to the Sun than other stars in the catalog. K stars also appear to have a bimodal distribution in distance.

to the rest of the Hypatia stars.

For the purposes of this work, we do not attempt to fully account for potential biases in the Hypatia catalog stars arising from the number of separate stellar surveys included in the catalog, but instead point out a few factors that are relevant to our compositional tests. First, in Figure 3.7 we plot the distributions of elemental abundances relative to solar abundances, colored by stellar type. In general we find the distributions are centered around solar abundances, however we note a peak in Ca in M stars at lower abundances relative to other stellar types as well as a larger fraction of F stars with low Al than other stellar types. Hinkel et al. (2014) point out potential biases for both of these elements, including a lack of Al abundance measurements at higher metallicities, which may be altering the distribution. Additionally, most of the low [Ca/H] stars were drawn from the same single survey which may be inducing a spurious, non-physical bias in the [Ca/H] abundances.

We also note that abundance uncertainties in the Hypatia catalog are strongly peaked at

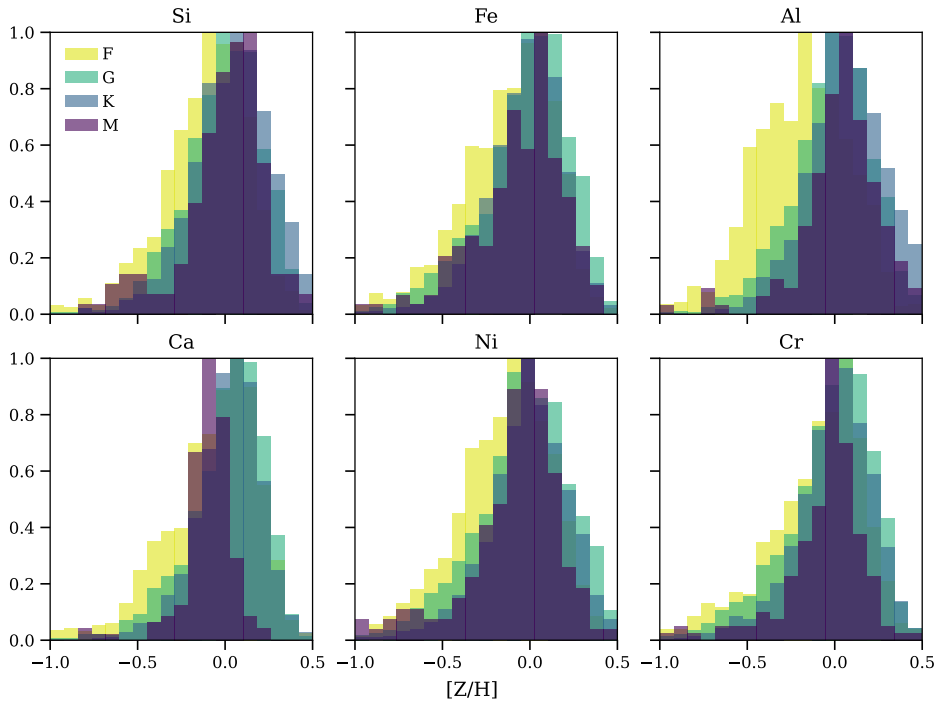

Figure 3.7: Distribution of elemental abundances in Hypatia catalog stars relative to solar abundances, grouped by stellar type. All element distributions are well centered at solar abundances, with the exception of Ca in M stars and Al in F stars.

about 0.05 dex. Distance appears to have a strong influence on the uncertainties, with a larger range of uncertainties for stars closer to the Sun, though it is unclear if this is a physical effect or due to the stellar samples included. Stars within about 500 pc have a large range of uncertainties, up to 1.75 dex, while stars that are farther away have a nearly flat distribution of uncertainties at around 0.05 dex.

From the Hypatia catalog we obtain abundances relative to solar abundances for each element, in the form $[\mathrm{Z/H}] = \log_{10}(\mathrm{Z/H})_* - \log_{10}(\mathrm{Z/H})_\odot$. We convert these relative abundances to molar ratios using the following equation:

$$\frac{\mathrm{n_Z}}{\mathrm{n_{Mg}}} = \frac{10^{[\mathrm{Z/H}]+\log_{10}(\mathrm{Z/H})_\odot}}{10^{[\mathrm{Mg/H}]+\log_{10}(\mathrm{Mg/H})_\odot}} = \frac{10^{[\mathrm{Z/H}]+\mathrm{A(Z)}}}{10^{[\mathrm{Mg/H}]+\mathrm{A(Mg)}}}, \tag{3.3}$$

where $\mathrm{A(Z)} = \log_{10}(\mathrm{Z/H})_\odot + 12$ is the solar abundance of the element Z, as defined in Lodders et al. (2009). Uncertainties in the stellar abundances are propagated through this conversion using a Monte Carlo approach.

We calculate the χ^2_ν goodness of fit parameter for Si, Fe, Al, Ca, Ni, and Cr, where available in each of the Hypatia catalog stars. For the elements considered in this work, we find median uncertainties of ~ 0.05 dex for the raw abundances relative to solar. To avoid invalid values for χ^2_ν, we replace any uncertainties of 0 with the median uncertainty for the corresponding element.

Figure 3.8 shows the abundances for 35 randomly selected Hypatia stars. As with the WDs, white panels indicate stars that pass as chondritic, light grey panels show stars that pass when an outlier is ignored, and dark grey panels do not pass as chondritic even if outliers are ignored. We find that outliers do not make a big difference, and that about 75% of stars pass as chondritic whether or not outliers are ignored. Similar to the WDs, we find that many of the stars that do not pass as chondritic are high in Mg, so that the abundances fall systematically below chondritic values.

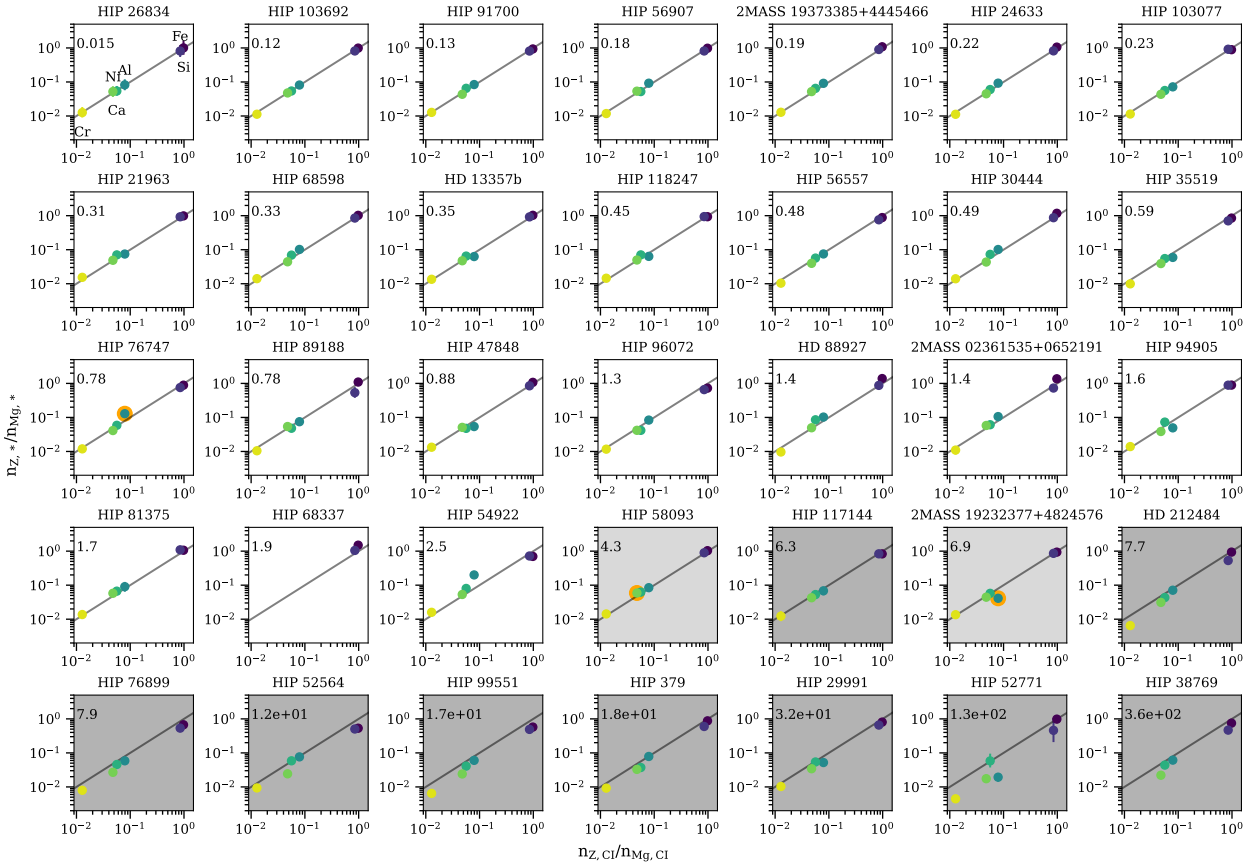

Figure 3.8: Comparison of Hypatia catalog metal abundances to chondritic composition, for the 35 randomly chosen Hypatia catalog stars. The χ^2_ν parameter is listed for each star. The order of elements in each plot, from left to right, is Cr, Ni, Ca, Al, Fe, Si, all ratioed to Mg. Stars with dark grey backgrounds are not considered a good fit to chondrite, using an α parameter of 0.05 for goodness of fit. Stars with light grey backgrounds are not a good fit for chondrite when all elements are used to calculate χ^2_ν, but do pass as chondritic when an outlier element is ignored (outliers highlighted in orange).

Because the uncertainties of the abundances vary strongly with the distance of each Hypatia star, we also compute fractions of chondritic stars considering only stars within 150 pc. We find that the results for the truncated sample are very similar to those for the full sample, with about 74% of stars providing good matches to chondrites.

3.5.1 Hypatia Mineralogy Classification

Projecting the Hypatia catalog stellar abundances into normative mineralogy ternary space, we find, as with the WDs, the uncertainties are too large to constrain the volumetric proportions of minerals in a meaningful way. To illustrate this, Figure 3.8 shows the abundances relative to chondrite for one of the Hypatia catalog samples, HIP 26834, yielding an excellent fit to a chondritic bulk composition. Figure 3.8 shows that the uncertainties in abundances are relatively low for this star, but they nonetheless create a very large spread in OLV and OPX fractions (Figure 3.9). Similar to the WDs, calculating the normative mineralogy for all of the Hypatia catalog stars results in a large spread in OLV and OPX values that reflect only uncertainties. This is consistent with Hinkel & Unterborn (2018), who find that much smaller measurement uncertainties than those of current observations are required to differentiate between unique planetary structures using stellar data.

3.5.2 Abundance Ratio Trends in Hypatia Catalog Stars

The Hypatia catalog stars exhibit some systematic trends in element abundances due to galactic chemical evolution (GCE) (Hinkel et al., 2014). In particular, we note decreasing abundances of α elements relative to iron with increasing [Fe/H], where the latter is a non-linear proxy for time. This trend is well studied in the Milky Way and other galaxies in the local universe, and is broadly due to increased injection of Fe into the interstellar medium (ISM) at later times due to the delayed effects of Type Ia supernovae. The late injection alters the α element-to-Fe ratios established by core-collapse supernovae that dominated the ISM at earlier times (e.g. Hayden et al., 2015; Kobayashi et al., 2020).

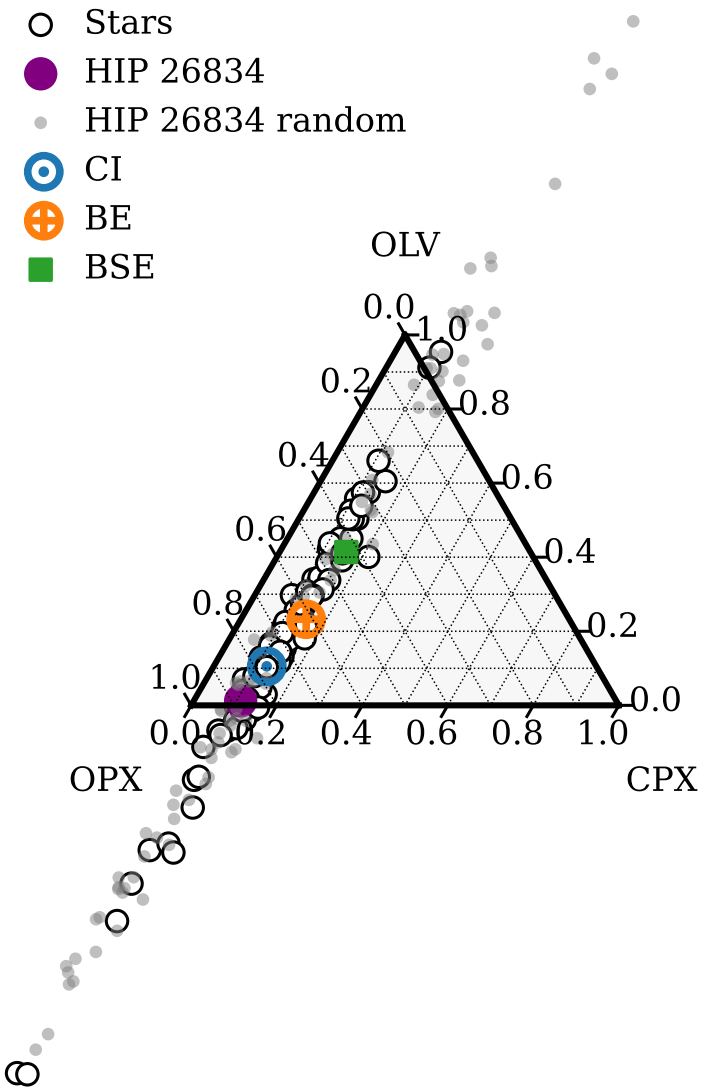

Figure 3.9: Ternary diagram for 100 randomly selected Hypatia stars, and the spread in OLV, OPX, and CPX for one of the best Hypatia fits to chondrite, HIP 26834 ($\chi^2_\nu \sim 0.02$). Despite being statistically indistinguishable from chondritic composition, the uncertainties in the measured abundances lead to huge spread in OLV and OPX quantities. Similar OLX, OPX, and CPX ranges resulting from propagation of uncertainties are found for all of the Hypatia stars.

Of the elements considered in this study, Fe, Cr, and Ni abundances accelerated with time in the Galaxy as a result of late-forming Type Ia supernovae accounting for about half of their overall production. The α elements Mg, Si, and Ca, on the other hand, are produced in Type II core-collapse supernovae, and increase more steadily with time in the Galaxy. Aluminum is somewhat separate from these two groups; it is also produced by Type II supernovae like the α elements, but the yield depends more strongly on the metallicity of progenitor stars (Kobayashi & Nakasato, 2011), and therefore exhibits a relatively small acceleration in abundance with time. The α elements and Al are lithophile elements while Fe, Cr, and Ni are siderophile. We note that the Hypatia catalog contains a few thousand stars in relatively close proximity to the Earth, and that trends in stellar composition therefore don't include the the wide ranges in ages or environmental affects that are observed in larger surveys (e.g. Horta et al., 2022).

We find that the fits to chondrite are influenced by the evolving lithophile/siderophile ratios. In Figure 3.10, we show the fractional difference between the observed abundances and chondrite for the Hypatia stars that do not pass as chondritic. For the chondritic stars, all of these distributions are centered at zero. However, Figure 3.10 shows that Fe, Cr, and Ni abundances relative to chondrite are lower than those of the lithophile elements by about a factor of two. This suggests that Type Ia products are inflating the χ^2_νs of non-chondritic stars relative to the α elements. Quantitatively, we find that of the ~ 2000 Hypatia catalog stars that do not pass as chondritic, 71% have a siderophile element as their worst fitting abundance ratio. Of this subset of stars, 71% pass as chondritic if Fe, Cr, and Ni abundances are ignored, meaning that when stars have anomalous siderophile abundances relative to the chondrite, they typically fail as chondritic because of the siderophiles. Meanwhile, 4% of stars with lithophiles as the worst fitting element pass as chondritic when lithophiles are ignored. In other words, the majority of stars that fail with anomalous lithophile elements are not failing solely because of the lithophile elements. We do not see these same patterns in the WD data. Amongst the WDs, 7/15 of the failures in the raw data and 2/10 of the

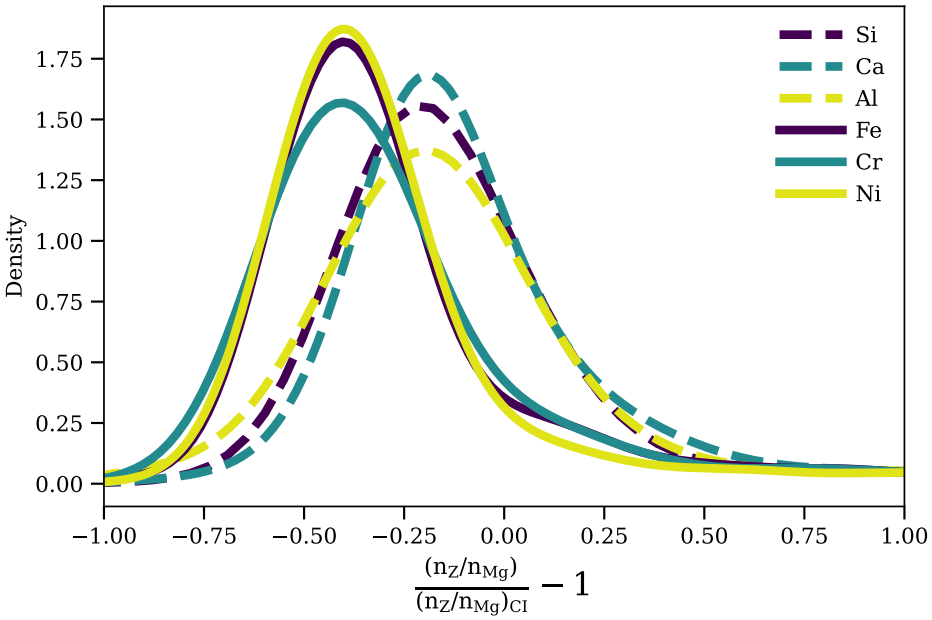

Figure 3.10: The fractional difference between the measured abundances in the Hypatia catalog stars relative to chondrite, for the stars that do not pass as chondritic. For the non-chondritic stars, siderophiles (Fe, Cr, Ni) tend to be the worst fitting elements rather than lithophiles.

failures in the steady-state are due to siderophiles. We do not find higher recovery rates amongst the siderophile failures when removing siderophiles elements.

In Figure 3.11 we show four plots of abundance ratios of the Hypatia stars, illustrating the effect of GCE on the goodness of fit to chondrite. The overall trends in relative abundances of lithophile and siderophile elements are plotted as [Mg/H] (lithophile, α nuclide) against [Fe/H] (siderophile, and a proxy for time) in panel A and the corresponding [Mg/Fe] ratios against [Fe/H] in panel B. As a zero-order approximation of chemical evolution in the local neighborhood, we categorize the trends in the data into two stages of pre- and post injection of Fe, Cr, and Ni by Type Ia supernovae. The break between trends is around [Fe/H] ~ -0.5, corresponding to ~ 8 billion years before present (Bellardini et al., 2022). The pre-Type Ia arrow in Figure 3.11 shows the general trends in α nuclides (lithophiles), represented here by Mg, relative to siderophile abundances at low metallicities prior to the influence of Type Ia supernovae on the ISM. The post-Type Ia arrow shows the influence of Type Ia supernovae

on higher metallicity stars after the influence of Type Ia supernovae on the ISM. The line in panel B shows the induced correlation between [Mg/Fe] and [Fe/H] that would be expected if Mg abundances were completely independent of Fe. At lower metallicity, we find that Mg and Fe abundances increase at very nearly the same rate, resulting in nearly constant [Mg/Fe] with metallicity. The increase in ISM Fe at later times flattens the growth of Mg vs Fe, resulting in a negative slope in [Mg/Fe] with metallicity. In panel A, we fit the low and high metallicity ranges and find a slope of 0.98 for the low end and 0.88 for the high end, with uncertainties in the slopes of less than 0.005. The decrease in slope is a reflection of the influence of the Type Ia supernovae at later times. For panel B, we find slopes of -0.03 and -0.19 for the low and high metallicity ranges, respectively.

We again show the [Mg/Fe] ratio as a function of metallacity in panel C, with points colored by whether the star passes as chondritic in the χ^2_ν tests, as well as the occurrence levels for chondritic and non-chondritic stars. The contours illustrate the somewhat different distributions of the chondritic and non-chondritic stars. We find that stars with very low metallicity, or Fe abundances, are those that are often classified as non-chondritic.

Finally, in lithophile-lithophile space (panel D of Figure 3.11), we find that the Hypatia catalog stars have a range of ratios centered on the Sun (the white star in Figure 3.11D). Consistent with GCE models, no overarching trends in ratios are seen in this case, and we find very little separation between the ratios of the Hypatia catalog stars that are considered chondritic and those of non-chondritic stars.

We conclude that older, lower metallicity stars are less likely to be consistent with a chondritic composition. In the χ^2_ν tests, stars that are statistically distinct from chondritic more often have low Fe, Cr, and Ni compared with solar, indicating that deviations from chondritic compositions are in part attributable to the delayed effects of Type Ia supernovae. The Hypatia catalog stars are all in relative close proximity to the Sun, so while we find that the rock-forming element ratios in most of the stars are consistent with chondrites, it is possible

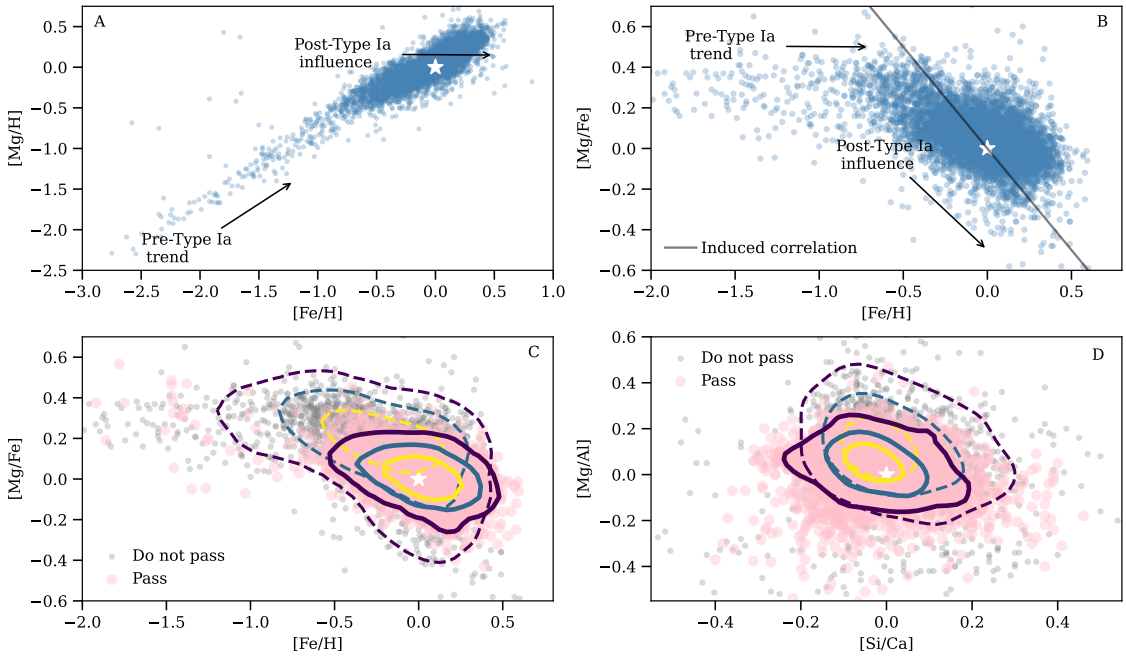

Figure 3.11: Elemental abundance ratios for the Hypatia catalog stars in dex. Throughout, the white star shows solar values. A) [Mg/H] vs. [Fe/H], showing growth of an α nuclide compared with Fe. [Fe/H] is broadly taken as an indicator of time. The influence of Type Ia supernovae on galactic chemical evolution is indicated by the two arrows. B) Same data as [Mg/Fe] vs. [Fe/H]. The solid negatively sloping line shows the effect of induced ratio correlation due to Fe appearing on both axes. C) Same as B) but with contours showing 50, 80 and 95% levels for the chondritic (solid contours) and non-chondritic (dashed contours) populations of stars based on χ^2_ν tests. The larger points indicate stars that pass as chondritic and the smaller points do not pass. The non-chondritic population generally extends to lower metallicities than the chondritic stars. D) Ratios of lithophile elements only, showing no clear trend.

Table 3.2: Percentage of stars in the Hypatia and WDs samples that pass the χ^2_ν test and are considered good fits to chondritic composition, using all available elements of Si, Fe, Mg, Al, Ca, Ni, and Cr. Leave-out-outliers (LOO) percentages are calculated by considering a star to be a good fit to chondrite if removing the outlier element allows the star to pass.

Sample	% Chondritic	% Chondritic, LOO
Hypatia, All	75.0	75.5
Hypatia, <150 pc	74.7	75.0
Hypatia, F	66.5	67.0
Hypatia, G	75.8	75.9
Hypatia, K	76.6	76.7
Hypatia, M	56.1	56.8
WD, raw	48.4	51.6
WD, SS	67.7	67.7

that this conclusion would not apply to older populations of stars or stars located outside of the local disk of the Milky Way due to the effects of GCE on lithophile/siderophile ratios.

3.6 Discussion

A summary of the fractions of bodies that are consistent with chondritic compositions is shown in Table 3.2. The leave-out-outliers ("LOO") column includes samples that pass as chondritic using the χ^2_ν test when an element identified as an outlier is ignored (Section 3.2). We find that outliers do not significantly affect the fractions of stars that are consistent with chondritic composition. Ignoring outliers changes the classification from non-chondritic to chondritic for one WD, and shifts the fraction of Hypatia catalog stars consistent with chondritic composition by less than 1%.

In Figure 3.12 we show the distribution of χ^2_ν values calculated for the Hypatia catalog sample and the raw and steady-state adjusted WD data. The χ^2_ν for all of the populations is

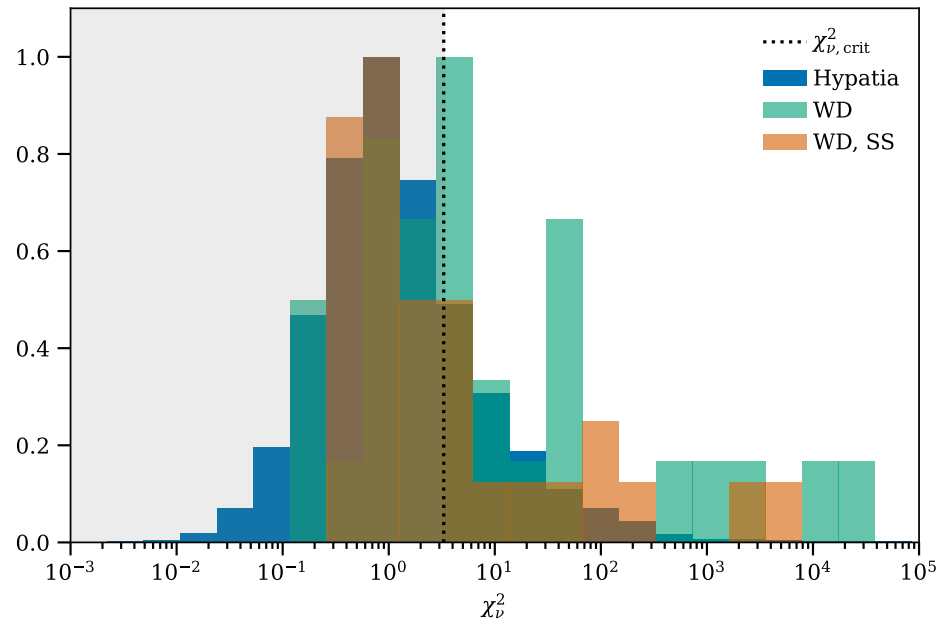

Figure 3.12: Distribution of χ^2_ν for the WDs (raw and steady-state adjusted), compared to the Hypatia catalog stars. The vertical line shows the approximate critical χ^2_ν value ($\chi^2_\nu \sim 3$ to 4, based on the number of observed elements), so that samples within the shaded regions are considered to be consistent with a chondritic composition.

most strongly peaked at low values, consistent with chondritic compositions. This suggests that the majority of extrasolar rocks in the solar neighborhood are built from material similar in composition to that which formed the solar system. The overwhelming fraction of Hypatia stars with chondritic rock-forming element ratios suggests that any deviations from chondrite-like compositions observed in exoplanets are more likely to be a result of the specific processing during planet formation rather than the result of large differences in the initial protoplanetary source material from chondritic. M stars in the Hypatia data set exhibit a tail to higher χ^2_ν values, though the majority of M stars still pass as chondritic. The difference in the M dwarf distribution relative to the others is evidently a result of different treatments of errors at near and far distances (M dwarfs are nearer) and potential systematic offsets in Ca.

Many of the WDs and Hypatia catalog stars that did not pass as chondritic have high

relative Mg concentrations; their abundance ratios in Figures 3.2 and 3.8 (lower panel) all fall below the 1-1 line for chondritic composition due to an excess in the Mg concentration used as the denominator in all ratios. Because we ratio to Mg, high Mg can systematically draw chondritic abundance ratios away from chondrite, inflating the χ^2_ν values. Examples amongst the WDs (raw data) include WD1415+234, SDSSJ2339-0424, SDSSJ1242+5526, WD1232+563, SDSSJ0738+1835, WD1350-162, and WD1929+012. If outliers are ignored, then G241-6 and SDSSJ1043+0855 are also fall into this list. For the WDs, applying the steady-state adjustment brings some, though not all, of the elements from the apparently Mg-rich WDs back to or above chondritic abundances. We find, therefore, that for WDs with excess Mg, deviations from chondritic in these cases is due in no small measure to the effects of settling.

We now explore how this study of local stars and WDs fits in to both the overarching metallicity gradients in the Galaxy and the current landscape of inferred exoplanet compositions.

3.6.1 Galactic Chemical Evolution

The Milky Way experiences spatial and temporal variations in stellar compositions, begging the question of how representative the pervasive chondritic compositions we see in the solar neighborhood are with respect to time and place in the Galaxy. In Section 3.5.2 we showed that galactic chemical evolution (GCE) has implications for the relative lithophile to siderophile ratios in stars over time, though the bulk of the Hypatia catalog stars are still consistent with chondrites. Here we evaluate the significance of chondritic rock-forming element ratios in the context of large scale variability in the Galaxy, outside of the solar neighborhood.

Spatial metallicity gradients in the Milky Way exist both radially and vertically (Galactic latitude) as a result of GCE. The disk midplane tends to have more metal-rich stars than above or below the plane and the disk itself exhibits a negative gradient, with generally higher

metallicities towards the galactic center (e.g. Hayden et al., 2014; Donor et al., 2020). Radial compositional changes may arise as annuli of the Milky Way are differentially enriched by supernovae and stellar feedback. For example, Bellardini et al. (2022) find from cosmological simulations that the older, inner disk receives more material from Type Ia supernovae, leading to lower [Mg/Fe] compared to the outer disk. They also find that some azimuthal scatter in abundances is to be expected, though the scatter is relatively low ($<\sim 0.05 \mathrm{d}ex$). While variations in [Fe/H] of > 1 dex are found across the entire galactic disk, much smaller variations in [Fe/H] of about ± 0.2 dex are found for stars within 2-3 kpc of the Sun (Monson et al., 2017). Radial variations in metallicity may be further damped by radial migration and mixing of stars throughout the disk.

Overall metallicity is expected to rise with time in the Galaxy. For example Timmes et al. (1995) showed that in the solar neighborhood at galactocentric radii of about 8 kpc, changes in [Fe/H] of about 1.5 dex are to be expected over 14 Gyr. However, the majority of this increase in metallicity occurs within the first few Gyr of galactic evolution, with changes of less than 0.5 dex [Fe/H] from about 2 Gyr onwards.

Therefore, while significant compositional changes occurred very early in the Milky Way's evolution, or very close to the galactic center, we do not expect to find demonstrable effects of GCE in rock-forming element ratios among stars in the stellar disk at galactocentric radii between ~ 4 kpc and ~ 10 kpc as seen today.

Given these trends in GCE, we now assess the impact on polluted WDs by estimating their formation times. The polluted WDs in our sample have cooling ages of about $50 - 600$ Myr and masses between $\sim 0.5 - 0.75 M_{\odot}$ (Table 3.1). These WD masses translate to initial stellar masses of $\sim 1 - 3 M_{\odot}$ (Cummings et al., 2018; El-Badry et al., 2018) and stellar lifetimes of $\sim 300\mathrm{Myr} - 10\mathrm{Gyr}$ (Schaller et al., 1992). Meanwhile, radioactive dating has constrained the age of the Milky Way to $\sim 13.8\mathrm{Gyr}$ (e.g. Cayrel et al., 2001; Hill et al., 2002; Cowan et al., 2002). Given overall metallicity changes are most significant in the first few Gyr of

the Galaxy, this suggests that GCE trends could only manifest in the lowest-mass WD in our data set (GaiaJ0218+3625), with progenitor masses approximately that of the Sun, and corresponding lifetimes exceeding 10 Gyr. Within our sample, we do not find evidence that lower mass WDs are worse fits to chondrite, however it is possible that such trends may be evident in future, larger samples of WDs.

We conclude that GCE could significantly alter the relative abundances of rock-forming material available for planet formation at early times and outside of the disk of the Milky Way. We explore a possible implication of this in the next section. We find that the majority of the current population of polluted WDs are derived from sufficiently young progenitors and nearby to the Sun that we do not expect GCE to have a strong affect on their compositions.

3.6.2 Iron core mass fractions

One of the possible consequences of GCE for exoplanets is the resulting core-mass fractions due to variations in lithophile/siderophile ratios. The mass fractions of iron-rich cores of rocky planets have been shown to be related to the iron mass fractions deduced from their host stars (e.g., Adibekyan et al., 2021; Rogers & Owen, 2021). Consistent with these studies, we calculate the iron mass fractions of planets that might have formed from the material polluting WDs or around the Hypatia catalog stars as

$$f_{\rm Fe} = m_{\rm Fe} / \left(m_{\rm Fe} + m_{\rm Mg_2SiO_4} + m_{\rm MgSiO_3} + m_{\rm SiO_2} \right),$$

where m_i is the abundance of the species i relative to H or He multiplied by the formula weight (Santos et al., 2015). The relative abundances by number of the silicate species are obtained from a linear transformation such that $\rm MgSiO_3 = 2Si - Mg$, $\rm Mg_2SiO_4 = Mg - Si$, and $\rm SiO_2$ is any remaining Si. The mass of O in the rock is therefore derived from the Si and Mg abundances, which corrects for any O excesses due to water (for the WD sample) or O production in the Hypatia catalog stars.

The mass fractions of Fe can be equated with the metal core fractions of planets given

the expectation of small concentrations of Fe in the silicate (Doyle et al., 2019). The top panel of Figure 3.13 shows $f_{\rm Fe}$ calculated from the abundances of the raw and steady-state adjusted WD data, and the Hypatia stellar abundances. The bottom panel illustrates the distribution of $f_{\rm Fe}$ resulting for four example WDs when uncertainties in observation are propagated through the transformation.

The Hypatia catalog stars with higher metallicities define a slightly skewed distribution of iron mass fractions, with a well-defined mode of about 32%, indistinguishable from the core mass fraction of the Earth, a tail towards lower values, and an approximate 1σ spread of about $\pm$5%. The lower metallicity Hypatia catalog stars define a peak in the distribution of $f_{\rm Fe} \sim 20 \pm 5\%$ (Figure 3.13). A similar variation in iron mass fractions was calculated by Michel et al. (2020) for stars in the thin and thick disks and halo of the galaxy.

The difference in most probable iron mass fractions obtained from the higher and lower metallicity Hypatia catalog stars suggests the possibility that planets formed in first several billion years in the Milky Way may have tended to have smaller metal cores compared with Earth, while planets formed later are generally similar to Earth in their metal core fractions. This is broadly due to the increase in siderophile elements at later times relative to lithophiles.

The WD sample size is much smaller, and plagued by larger uncertainties. The bottom panel of Figure 3.13 shows the spread in $f_{\rm Fe}$ obtained for each WD after taking 100 random draws of of Si, Mg, and Fe abundances from a parent population defined by the WD medians and uncertainties in each element. The 1σ uncertainty in iron mass fraction ranges from about $4-15\%$, with a median of $\sim 7\%$. In any case, the raw data define iron mass fractions peaking at $20-30\%$ while the steady-state adjusted data yield a peak at $30-40\%$. While we do calculate low ($f_{\rm Fe} < 10\%$) iron mass fractions for some WDs, lacking further information about the ages or initial metallicities of these stars prevents us from identifying whether the low iron is due to the systematic effects of GCE. As a whole, these data suggest the

majority of planets that might have formed from these polluting materials have metal core mass fractions that are not significantly different from an Earth-like planet. Following the discussion in Section 3.6.1, abundance measurements for older WDs (likely lower-mass WDs), or WDs outside of the thin disk of the galaxy could help identify whether the lower core mass fractions are influenced by GCE.

3.7 Conclusions

In this work, we show that about half of polluted WDs, and well over half of the Hypatia catalog stars, have compositions that are consistent with chondrites. We use the χ^2_ν goodness of fit to test the composition of each star, with a threshold of $\alpha = 0.05$ to select matches to chondritic composition, and allow for a 2σ error in the χ^2_ν to account for our small sample size of observed elements.

We use Monte Carlo methods to propagate the uncertainties in the observed abundances of the WDs and Hypatia catalog stars. We find that many solar system rocks, including bulk Earth and bulk silicate Earth, bulk silicate Mars, and E chondrites, are indistinguishable from CI chondrite given current uncertainties in WD pollution measurements. Additionally, we find that we are not able to characterize either Hypatia catalog stellar abundances or WD pollution by normative mineralogies due to the impossibly large uncertainties obtained by propagating measurement uncertainties.

The polluted WD data indicate that the bulk of exo-rocks are consistent with chondritic compositions. This is supported by the compositions of rocks implied by the Hypatia catalog stars, which suggest most material in the solar neighborhood formed in protoplanetary disks with rock-forming element ratios similar to our Sun. The Hypatia catalog stars do suggest, however, that galactic chemical evolution can lead to exoplanet compositions statistically different from the solar system in the first few billion years of the Galaxy or in galactic substructures with considerably different metallicities. One implication of this is that earlier

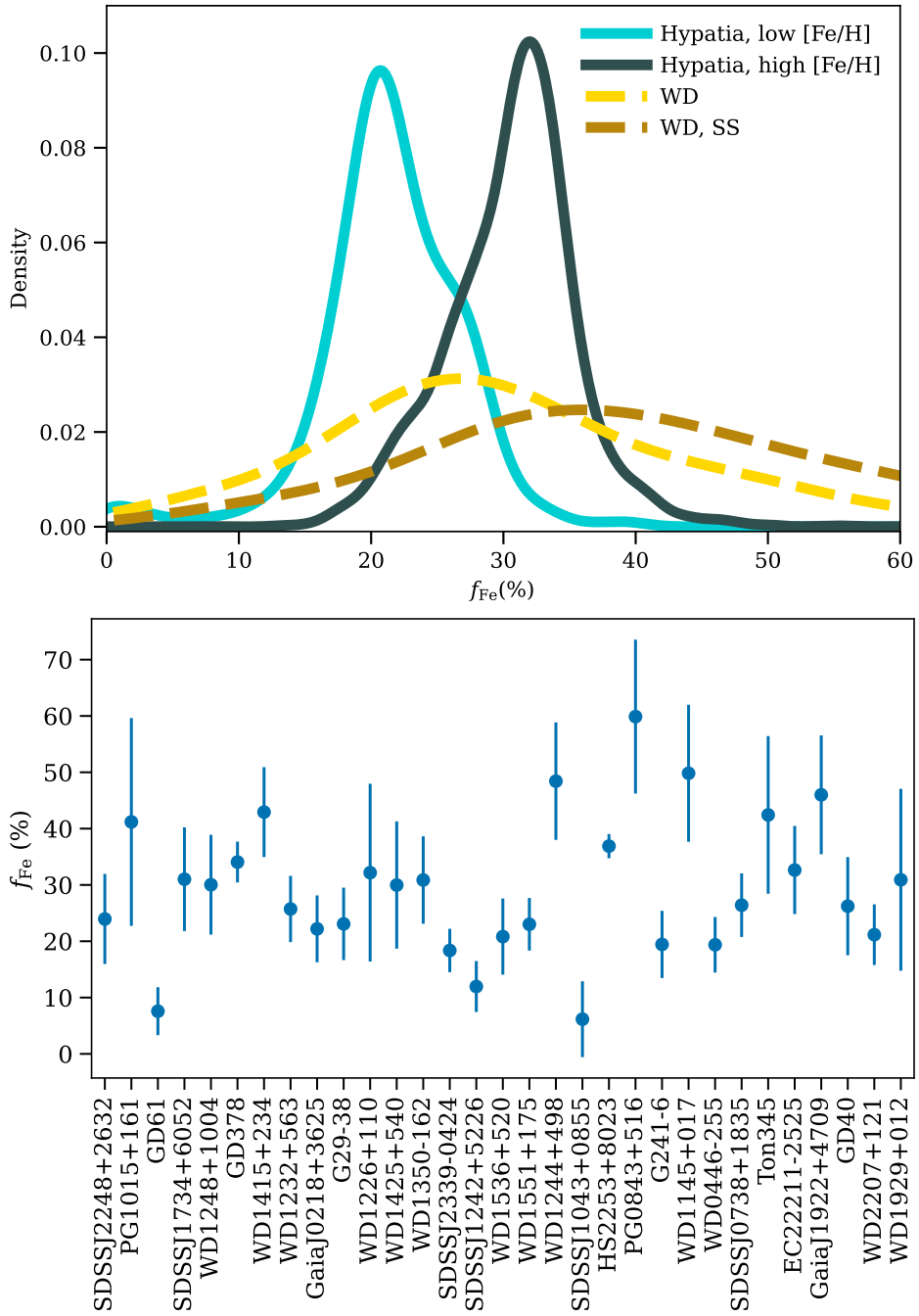

Figure 3.13: Top: Distribution of iron mass fractions ($f_{\rm Fe}$) for the WDs and Hypatia catalog stars. We show both raw and steady-state values for the WDs, and split the Hypatia catalog stars into low ([Fe/H]< -0.5) and high ([Fe/H]> -0.5) metallicity categories. Bottom: Median and 1σ spread in $f_{\rm Fe}$ for the sample of WDs based on 100 random draws from their median and uncertainty in the raw Si, Mg, and Fe abundances. Most WD iron fractions have a range of at least 10% when accounting for uncertainty in their abundances.

in the evolution of the Milky Way, rocky planets may have formed with substantially less massive metal cores than Earth.

Our methods do not suggest any of the WD polluters are composed of crust, either MORB or continental crust. No stars in our sample are better fits to MORB or continental crust than chondrite, even WDs with the largest deviations from chondritic composition ($\chi^2_\nu \gg 10$). We conclude that the relative abundances of rock-forming elements in polluted WDs and local stars are relatively homogeneous, which suggests that the majority of extrasolar rocks in the solar neighborhood originate from chondrite-like compositions.

CHAPTER 4

Do White Dwarfs Sample Water-Rich Planetary Material?

4.1 Introduction

The growing population of super-Earths and sup-Neptunes, and advancements in connecting models of planetary interiors to mass/radius estimates, has sparked an ongoing discussion on the prevalence of water worlds (e.g. Boldog et al., 2024; Piette et al., 2023; Kempton et al., 2023; Chakrabarty & Mulders, 2024; Unterborn et al., 2018). However, degeneracies in modeling bulk densities often make it difficult to distinguish between water-rich planets and planets with light elements stored in their interiors (e.g. Dorn & Lichtenberg, 2021; Schlichting & Young, 2022).

The relative abundances of rock-forming elements evidenced in polluted white dwarfs (WDs) offer an independent method for studying exoplanetary water abundances in extrasolar rocky bodies (e.g., asteroids, comets, or moons). The concentration of water in the parent bodies accreted by WDs is typically inferred from excess abundances of O relative to other rock-forming elements, and a number of WDs have been identified as having accreted icy or watery bodies based on excesses of oxygen (e.g. Farihi et al., 2013; Raddi et al., 2015; Xu et al., 2017; Hoskin et al., 2020; Hollands et al., 2022). Observations of hydrogen persistent in the atmospheres of helium-dominated WDs have also been used to assess water abundances. However, while observations of H are fairly common in He atmospheres, typical accretion

rates are frequently so low that the associated water accrued by accretion would be negligible in comparison Jura & Xu (2012); Gentile Fusillo et al. (2017).

In this work we leverage a large sample of polluted WDs with O abundances to gain a better understanding of the distribution of water concentrations amongst WD polluters. Accurately recovering elemental abundances from polluted WDs is sensitive to assumptions made about the accretion and settling rates in the WD atmosphere (e.g. Doyle et al., 2020), and we therefore also test how different phases of the accretion process influence inferred water abundances. We test accretion phases by assigning intervals of increasing mass with time (mass-buildup phase) decreasing mass with time, (mass-settling phase), and steady-state accretion to each WD and comparing the effects of these processes on calculated elemental abundances and implied water contents. We quantify our comparison using a Markov-chain Monte Carlo (MCMC) sampling to outline the posterior distributions of characteristic timescales in our accretion model and to thereby find the best fit to the observations.

We find that most of the polluters in our sample have significant O excesses that result in a wide range of water concentrations, with a peak in the overall distribution at around $20-30\%$ water by mass. Both elemental abundance ratios and corresponding inferred water abundances tend to be robust with respect to accretion phases, varying drastically only at very late times in the mass-settling phase. In the MCMC tests, we find that if we assume most WD pollution comes from parent bodies with chondritic compositions, then most WDs are in or near a steady-state phase, though the distributions are broad.

This paper is structured as follows. In Section 4.2 we describe the model used for accretion and settling on the WDs and our methods for calculating water abundances from the model. We report our resulting water mass fractions in Section 4.3, and discuss our water results and our model's implications for WD accretion in Section 4.4. We summarize our results in Section 4.5

4.2 Methods

4.2.1 White Dwarf Sample

Our sample consists of 42 previously observed WDs that include the elements O and Mg (for uniform normalization) along with abundances for at least one other element. We also include newly acquired abundances for an H-dominated WD, WD0145+234. The references and stellar parameters for the WDs are listed in Table 4.1. For consistency across the sample set, we draw settling timescales from the Montreal White Dwarf Database (Dufour et al., 2017) based on the effective temperature and log gravity reported by the references in Table 4.1.

Elemental abundances for polluted WDs are typically reported in the literature as the logs of abundances of metal Z to H or He, $\log(\mathrm{Z/H(e)})$. Throughout this work, we propagate uncertainties in the log abundances to simple ratios and water concentrations by taking 1000 random draws of the log abundances, assuming a normal distribution with the reported abundance and uncertainty as the mean and standard deviation. After converting the random draws to the quantity of interest, we report the median, lower, and upper uncertainties of the new quantity as the 50, 16, and 84th percentiles of the converted random draws, respectively.

Table 4.1: WD parameters are collected from the references listed in the table. Throughout this work we group WDs by the dominant element in their atmospheres (H or He-dominated only).

WD	Alternate Name (from MWDD)	Reference	Type	T (K)	log g
G29-38	G29-38	Xu et al. 2014	H	11820	8.15
WD0145+234	WD0145+234	This work	H	12679	8.06
SDSSJ1043+0855	SDSS J104341.53+085558.2	Melis 2016	H	18330	8.05
PG1015+161	PG1015+161	Gänsicke et al. 2012	H	19226	8.04
WD1226+110	WD1226+110	Gänsicke et al. 2012	H	20900	8.15
WD1929+012	WD1929+012	Gänsicke et al. 2012, Melis et al. 2011	H	21200	7.91
PG0843+516	PG0843+516	Gänsicke et al. 2012	H	23095	8.17
SDSSJ0956+5912	GALEX J095645.1+591241	Hollands et al. 2017	He	8100	8.02
WD0446-255	WD0446-255	Swan et al. 2019	He	10120	8.00

WD1350-162	WD1350-162	Swan et al. 2019	He	11640	8.02
WD1232+563	WD1232+563	Xu et al. 2019	He	11787	8.30
SDSSJ1242+5226	SDSS J124231.07+522626.6	Raddi et al. 2015	He	13000	8.00
1013+0259	WD J101347.13 + 025913.82	Izquierdo et al. 2023	He	13158	8.08
SDSSJ2339-0424	GALEX 2667197548689621056	Klein et al. 2021	He	13735	7.93
SDSSJ0738+1835	WD J0738+1835	Dufour et al. 2012	He	13950	8.40
HS2253+8023	HS2253+8023	Klein et al. 2011	He	14000	8.10
WD1425+540	WD1425+540	Xu et al. 2017	He	14490	7.95
WD1145+017	WD1145+017	Fortin-Archambault et al. 2020a	He	14500	8.11
0944-0039	WD J094431.28 - 003933.75	Izquierdo et al. 2023	He	14607	8.76
GaiaJ0218+3625	GaiaJ0218+3625	Doyle et al. 2023	He	14691	7.86
EC22211-2525	EC22211-2525	Doyle et al. 2023	He	14743	7.90
WD2207+121	WD2207+121	Xu et al. 2019	He	14752	7.97
WD1551+175	WD1551+175	Xu et al. 2019	He	14756	8.02
WD1244+498	WD1244+498	Doyle et al. 2023	He	15150	7.97
WD1248+1004	WD1248+1004	Doyle et al. 2023	He	15178	8.11
G241-6	G241-6	Jura et al. 2012	He	15300	8.00
GD40	GD40	Jura et al. 2012, Klein et al. 2010	He	15300	8.00
1516-0040	WD J151642.97 - 004042.50	Izquierdo et al. 2023	He	15448	8.42
GaiaJ1922+4709	GaiaJ1922+4709	Doyle et al. 2023	He	15497	7.95
GD378	GD378	Klein et al. 2021, Desharnais et al. 2008	He	15620	7.93
0859+1123	WD J085934.18 + 112309.46	Izquierdo et al. 2023	He	15717	8.19
0030+1526	WD J003003.23 + 152629.34	Izquierdo et al. 2023	He	15795	8.18
0930+0618	WD J093031.00 + 061852.93	Izquierdo et al. 2023	He	15982	8.18
1627+1723	WD J162703.34 + 172327.59	Izquierdo et al. 2023	He	16134	8.29
1109+1318	WD J110957.82 + 131828.07	Izquierdo et al. 2023	He	16308	8.25
SDSSJ1734+6052	SDSSJ1734+6052	Doyle et al. 2023	He	16340	8.04
0259-0721	WD J025934.98 - 072134.29	Izquierdo et al. 2023	He	16390	8.26
GD424	SDSS J022408.82+750257.4	Izquierdo et al. 2021	He	16560	8.25
1359-0217	WD J135933.24 - 021715.16	Izquierdo et al. 2023	He	16773	8.14
GD61	GD61	Farihi et al. 2013	He	17280	8.20
WD1415+234	WD1415+234	Doyle et al. 2023	He	17312	8.17
SDSSJ2248+2632	SDSSJ2248+2632	Doyle et al. 2023	He	17369	8.02
Ton345	Ton 345	Wilson et al. 2015	He	19780	8.18

4.2.2 Atmospheric Accretion and Settling Model

We adopt the exponential accretion and settling model by Jura et al. (2009). This model assumes the accretion disk of pollution dissipates and accretes onto the WD exponentially

so that the mass of the disk at a given time is $M_{\rm disk}(t) = M_{\rm PB}e^{-t/\tau_{\rm d}}$, where $\tau_{\rm d}$ is the e-folding lifetime of the disk and $M_{\rm PB}$ is the initial mass of the parent-body source of the pollution. Pollution also settles out of the atmosphere of the WD at a rate of $\dot{M}_{\rm Z} = M_{\rm Z}(t)/\tau_{\rm Z}$, where $M_{\rm Z}$ is the mass of element Z in the atmosphere at a given time and $\tau_{\rm Z}$ is a model-derived settling timescale which can vary between days to millions of years for different elements and WD structures (Koester, 2009; Blouin et al., 2018). The fraction of an original body's mass that is in the WD atmosphere at time t is therefore

$$\frac{M_{\rm atm}(Z,t)}{M_{\rm PB}(Z)} = \frac{\tau_{\rm Z}}{\tau_{\rm d} - \tau_{\rm Z}}\left(e^{-t/\tau_{\rm d}} - e^{-t/\tau_{\rm Z}}\right). \tag{4.1}$$

According to Equation 4.1, pollution in the WD atmosphere increases after the onset of accretion, reaches a peak at a steady-state point where the accretion rate and settling timescales equilibrate, and then decreases as the accretion disk is depleted and settling dominates the system. We refer to these three phases as the mass-buildup, steady-state, and mass-settling phases.

Accretion reaches the steady state when $dM_{\rm atm}/dt = 0$. Solving for the steady-state time, $t_{\rm SS}$, gives

$$t_{\rm SS}(Z) = \frac{\tau_{\rm d}\tau_{\rm Z}}{\tau_{\rm d} - \tau_{\rm Z}} \ln\left(\frac{\tau_{\rm d}}{\tau_{\rm Z}}\right). \tag{4.2}$$

The steady-state point does not occur at exactly the same time for all elements, as it is dependent on the relevant settling timescale. However, the different steady-state times are closely spaced, so we choose a steady-state time that is the median of the $t_{\rm SS}$ values for the observed elements for any given WD.

From equation 4.1, we find the *inferred* element ratio of an accreting parent body from an observed abundance ratio to be

Table 4.2: Limits for the ratio of abundances in an inferred parent body relative to the observed abundances from Equation 4.3 for different timescale assumptions.

Timescales	Limit of $\frac{n_1}{n_2}\|_{\rm PB}/\frac{n_1}{n_2}\|_{\rm obs}$
$t \ll \tau_1, \tau_2, \tau_{\rm d}$	1
$t \gg \tau_1, \tau_2, \tau_{\rm d}; \tau_{\rm d} > \tau_1, \tau_2$	$\frac{\tau_2}{\tau_1}$
$t \gg \tau_1, \tau_2, \tau_{\rm d}; \tau_{\rm d} < \tau_1 < \tau_2$	inf
$t \gg \tau_1, \tau_2, \tau_{\rm d}; \tau_{\rm d} < \tau_2 < \tau_1$	0

$$\left.\frac{n_1}{n_2}\right|_{\rm PB} = \left.\frac{n_1}{n_2}\right|_{\rm obs} \frac{\tau_2}{\tau_1}\frac{\tau_{\rm d}-\tau_1}{\tau_{\rm d}-\tau_2}\frac{e^{-t/\tau_{\rm d}}-e^{-t/\tau_2}}{e^{-t/\tau_{\rm d}}-e^{-t/\tau_1}}, \tag{4.3}$$

where τ_1 and τ_2 are the settling timescales for the elements of interest. We use Equation 4.3 throughout this work to calculate the compositions of pollution parent bodies from observed abundances.

Table 4.2 list the various limits of Equation 4.3. For $t \ll \tau_1$, τ_2, and $\tau_{\rm d}$, $\left.\frac{n_1}{n_2}\right|_{\rm PB} \sim \left.\frac{n_1}{n_2}\right|_{\rm obs}$, in other words the observed abundances ratios match those of the parent body at early times. At late times in the accretion process, when $t \gg \tau_1$, τ_2, and $\tau_{\rm d}$, the abundance ratios trend towards the ratio of settling times if the disk timescale exceeds the settling timescales. If the disk timescale is shorter than the relevant settling timescales, then the parent body abundance ratios diverge towards 0 or infinity. Based on typical settling timescales for H-dominated WDs, and the typical range of $\tau_{\rm d}$ estimates of $10^5 - 10^7$yr, most H-dominated stars will fall in the limit of $\tau_{\rm d} > \tau_1, \tau_2$.

4.2.3 Bayesian Analysis of Abundances

As demonstrated by Section 4.2.2, relating observed and parent body compositions requires knowledge of the characteristic timescale for the life of the accretion disk ($\tau_{\rm d}$) and the time t since the onset of accretion at which we observe the WD. We test the effect of selecting

different characteristic timescales on abundances and water fractions in two ways. First, we manually calculate these quantities assuming mass-buildup, mass-settling, and steady-state phases of accretion (results in Section 4.3.2). Separately, we also apply an MCMC approach to explore the most likely timescales for the observed polluted WDs based on the hypothesis that the original bodies were chondritic in composition (Section 4.3.3). This section discusses the details of our MCMC approach.

Multiple studies have found that the material polluting WDs is rocky, and consistent with typical chondritic material in the solar system (Swan et al., 2023; Trierweiler et al., 2023; Doyle et al., 2023), to within typical uncertainties in WD observations. We therefore posit that the lithophile elements in each sample's parent body have the same abundance ratios as a CI chondrite. We assume the rocky portion of each polluting body, adjusted for accretion and settling effects, is restricted to a chondritic composition, and variations in the refractory to volatile abundance ratios in polluting parent bodies are due to variations in rock/ice ratios.

For each WD, we use simulated annealing, as implemented with the dual annealing python package, to perform an initial search for the $\tau_{\rm d}$ and t timescales that best reproduce the observed abundances of lithophile elements, assuming a CI chondrite composition for the parent body that evolves as prescribed by Equation 4.1. In this search, solutions for most WDs occupy a relatively large area in $\tau_{\rm d}$-t space, often spanning several orders of magnitude in one or both dimensions.

We then apply an MCMC to the abundances of the lithophile elements for each WD, using the emcee package (Foreman-Mackey et al., 2013), to find the posterior distributions for the timescales. We carry out the MCMC with both a basic log-likelihood function comparing the CI chondrite-derived model abundances to the data, and an amended log-likelihood function which weights the likelihood by the fraction of parent body mass in the atmosphere at the selected time of observation t (Equation 4.1). The second test is predicated on the assumption

that we are most likely to observe WD pollution during stages of accretion where the mass of pollution in the atmosphere is at a maximum. Finally, from the MCMC results we derive the distributions of parent body abundances for all elements, recovering the siderophile and atmophile/volatile abundances implied under the assumption of a chondritic rock.

In addition to imposing chondritic parent bodies, these tests further depend on the assumption that each sample of WD accretion is made up of a single body, or that the mass observed in the atmosphere is primarily due to a single accretion event. The results of Trierweiler et al. (2022) support this assumption, and show that even when accretion is driven by many smaller objects, such as during the accretion of a debris belt, we are most likely observing the WD soon after the latest accretion event, when a single object still dominates the observable material.

4.2.4 Calculation of Water Mass Fractions

We calculate water abundances based on the assumption that any excess O in the WD pollution is due to water. In calculating water mass fractions, we consider the major elements of Ca, Al, Na, Fe, Si, and Mg, and derive an oxygen budget assuming all elements are present as oxides in the rock. We first check for an O excess in each WD by calculating the moles of O required to transform all other abundances into charge-balanced oxide components. If there is an excess of O, the resulting water mass is the molar mass of H_2O multiplied the moles of excess O. Finally, we report water mass fractions by diving the water mass by the sum of the water mass and mass of the oxides.

To calculate a minimum water mass fraction, we assume all iron is in oxidized form (FeO) as opposed to as metal. Including a core would increase the water mass fractions as more oxygen would be free to make water. Throughout this work, we also calculate water fractions both based on the observed abundances and assuming the relative abundances of all lithophile elements (in this case all elements except O) are CI chondrite.

4.3 Results

4.3.1 Water abundances from observed element ratios

We first calculate water mass fractions using the data as reported and without accounting for any effects of accretion. Figure 4.1 shows the observed abundance ratios for the WDs in our sample, ratioed to Mg and plotted relative to the corresponding abundance in CI chondrites. In order to quantify the comparison between the WDs in this study and CI chondrites, we compare the lithophile element ratios to the composition of CI chondrites with a χ^2_ν goodness of fit test (Trierweiler et al., 2023) based on the CI chondrite composition reported by Lodders (2021). We find 3/7 of H-dominated WDs and 23/36 of the He-dominated WDs have lithophile abundances that are statistically consistent with CI chondrites (Figure 4.1).

In Figure 4.2 we show the smoothed distribution of water mass fractions calculated from the observed element ratios, summed over all of the WDs in our sample. To visually compare the relative number of dry and wet pollution samples we place all water concentrations of 0% at 10^{-4}. Approximately one third of the WDs evidently accreted dry material in that they have no discernible O excesses. Overall, the median water mass fraction inferred for the sample of polluters is 26%; considering only the pollution with non-zero O excesses, the median water concentration is 37%. We notice that the H-dominated stars in the sample tend to not have large O excesses, though it is unclear if this is physical or systematic to observing H-dominated WDs.

We also calculate water mass fractions assuming that all non-O element ratios are chondritic (dotted line in Figure 4.2). We find that this results in a slight decrease in the number of pollution samples with non-zero water abundances, though the effect is quite minimal.

Finally, for each of the He-WDs, we compare the calculated distribution of excess O abundances to the observed H abundances to check for agreement. We calculate both excess O and H relative to Mg, propagating the uncertainties from all elements. We find that 32/36

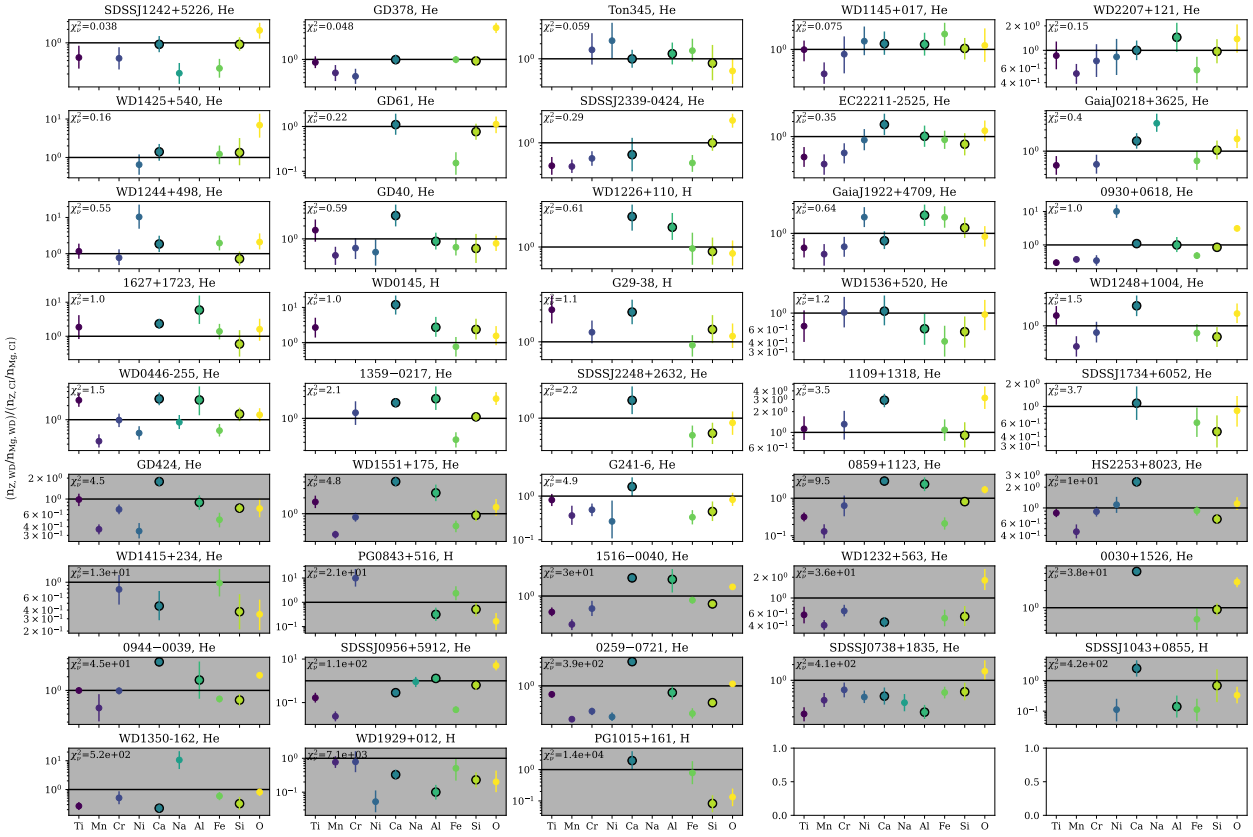

Figure 4.1: Abundances ratioed to Mg and reported relative to CI chondrite, for the WDs in our sample. The χ^2_ν goodness of fit of the abundance ratios to CI chondrite is listed in the upper left corner. Only the lithophile elements (outlined in black) are included in the χ^2_ν fit. WDs with grey backgrounds have lithophile abundance ratios that are statistically distinct from CI chondrite.

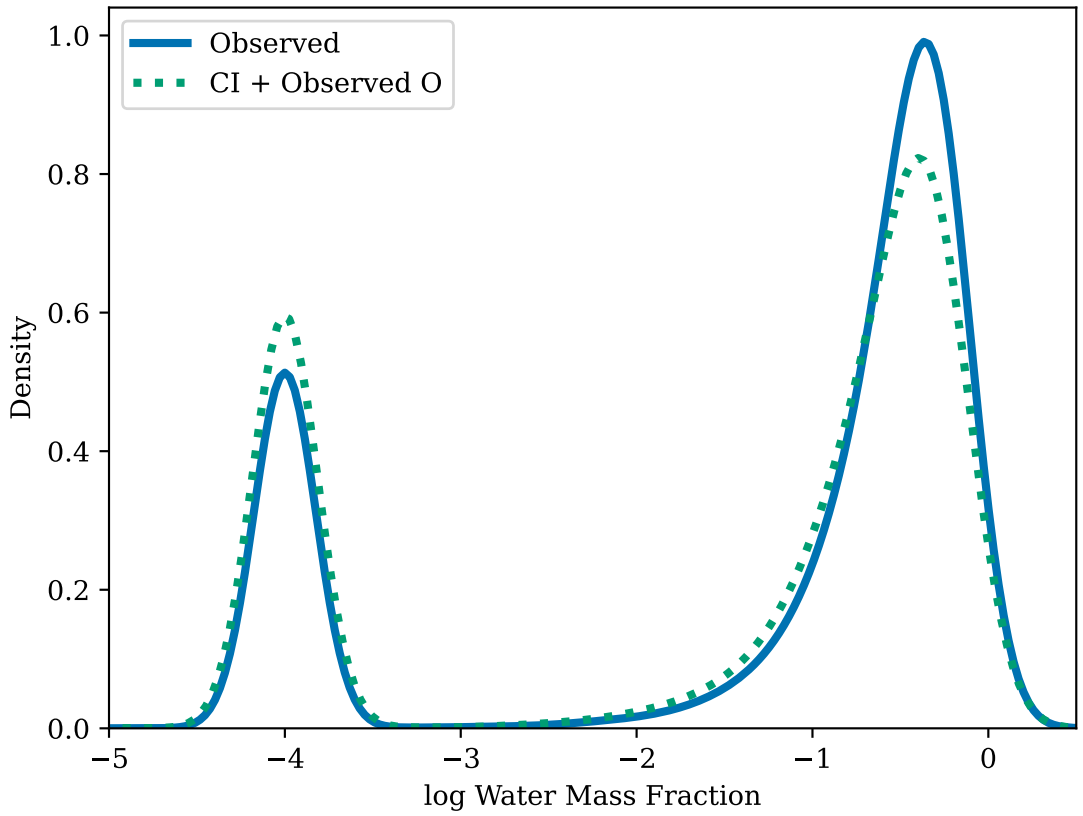

Figure 4.2: The distribution of water mass fractions derived from observed abundances summed over all WDs in our sample. For visualization purposes, WDs with water mass fractions of zero are instead set to 10^{-4}. We shows results both using all available observed elements (solid curve) and using observed O abundances while all other abundance ratios are set to chondritic values (dashed curve, “CI + Observed").

of the He-WDs have distributions of H abundances that are at least large enough to account for all excess O as being due to water.

4.3.2 Applying accretion phases

The parent body relative abundance ratios recovered from the WD data vary with the phase of accretion being observed (see Equation 4.3). In the previous section we calculated water concentrations from the WD abundances as-observed; we now carry out the water calculation accounting for various accretion phases. To understand the influence of different accretion phases on the inferred parent-body compositions, we calculate parent-body abundance ratios and water fractions across all three phases of accretion (mass-buildup, steady-state, and mass-settling), for each WD using Equation 4.3.

Figure 4.3 shows the evolution of the calculated parent body element ratios for two example H and He WDs, for an assumed disk e-folding time of 10^5 yr. The corresponding buildup, steady-state, and settling phases are shown as the different shaded sections of each plot. As discussed in Section 4.2.2, parent body ratios for the mass-settling phase ($t \gg \tau_{\rm d}, \tau_1, \tau_2$) for stars with settling times longer than $\tau_{\rm d}$ will diverge towards 0 or infinity. The relatively long settling times for oxygen leads to O abundances diverging later than most other elements. For visual clarity, we do not show the uncertainties on the abundances, however for the H-WD example, all elements except O remain within the bounds of the observed value for the duration of the times shown in the plot. For the He-WD, abundances ratios are within uncertainty limits until about $1-2$ settling timescales.

To illustrate the net effect of the evolution of abundance ratios with time shown in Figure 4.3 on a population level, we calculate the distribution of element abundances summed across all WDs in our sample at each phase of accretion. For this purpose, we select a diagnostic time within each accretion phase at which to calculate values, though it should be remembered that abundances may change fairly drastically over the full course of each phase. The two

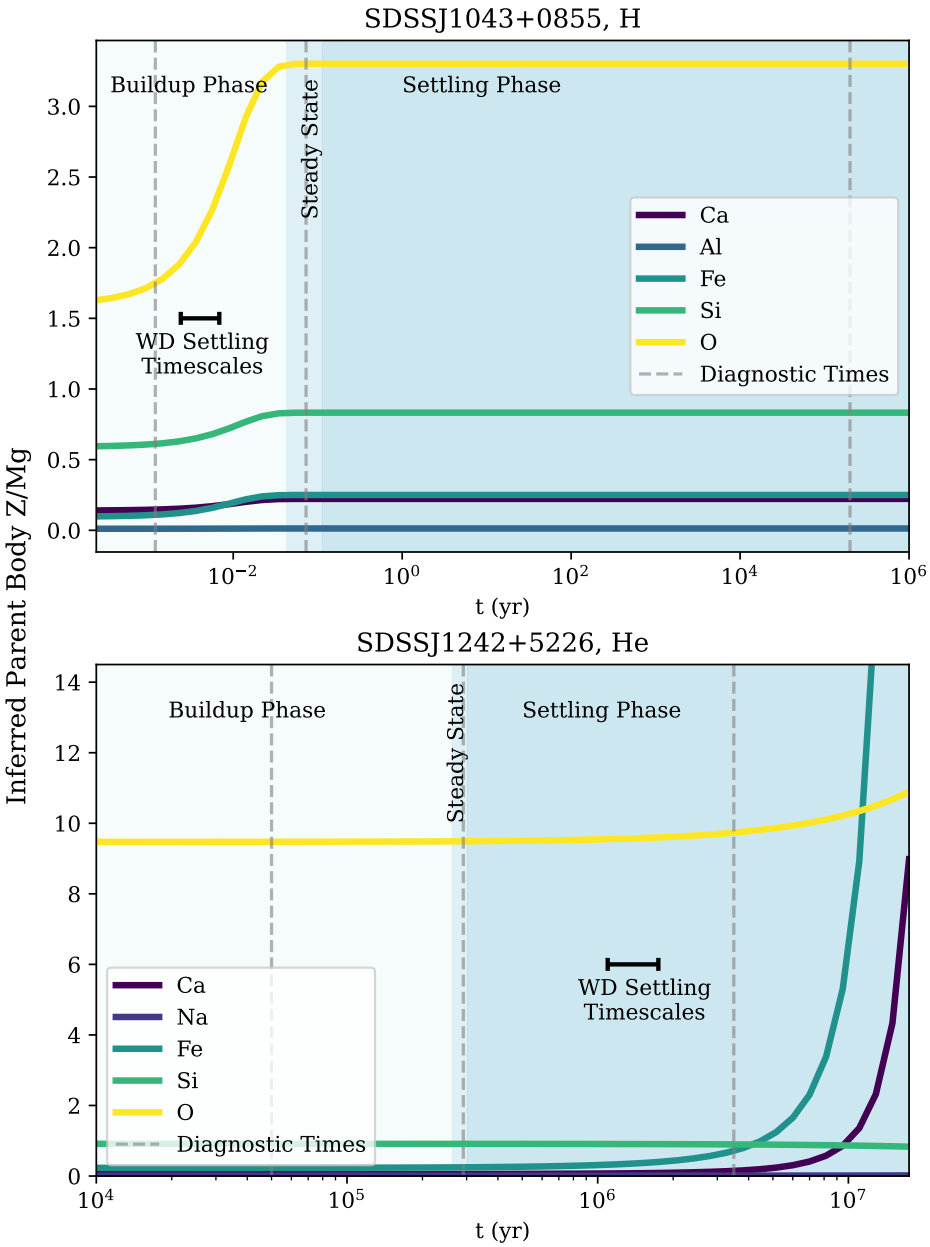

Figure 4.3: Evolution of inferred parent body abundance ratios with time for example H and He-rich WDs, for a $\tau_{\rm d} = 10^5$ yr. The range of settling timescales for each WD are shown by the horizontal bars, and the times at which we sample abundance ratios in the buildup, steady-state, and settling phases are denoted by the vertical lines.

diagnostic times for the mass-buildup and mass-settling phases are $t_{\rm buildup} = 0.5 \times \min(\tau_d, \tau_z)$ and $t_{\rm settling} = 2 \times \max(\tau_d, \tau_z)$, respectively. The steady-state times, $t_{\rm SS}$, are given by Equation 4.2 and are element dependent, so we calculate a steady-state time for each observed element and take the median as our assumed value. The three diagnostic times $t_{\rm buildup}$, $t_{\rm SS}$, and $t_{\rm settling}$ are shown as dashed vertical lines in Figure 4.3.

Figure 4.4 shows the parent body abundance ratio distributions (summed over all WDs) at the buildup, steady-state, and settling diagnostic times with a disk timescale of 10^5 yr. While the buildup and steady-state abundance ratios generally match, the settling phase solutions typically diverge, owing to the sensitivity to the differences in settling timescales (Table 4.2). The peaks of the abundance ratios are drawn somewhat closer to chondritic values in the settling phase, however the spread in the values increases dramatically, reflecting the sensitivity of the settling phase values to the exact observation time considered.

We now convert the relative element abundances to water mass fractions, at the same disk timescale of 10^5 yr. The resulting water concentrations as a function of time for the two example H and He WDs are shown in Figure 4.5. The error bars show the uncertainties in water concentration obtained by propagating the uncertainties in the observed element abundances. As a result of the mathematical limits of the accretion process outlined in Table 4.2, we find that water mass fractions typically stabilize when the disk timescale exceeds the settling timescales, while WDs with disk timescales less than settling timescales will preserve less evidence for accreted water over the course of several settling timescales. For water abundances that stabilize, the resulting values are usually within range of the uncertainties of the water fraction calculated using the observed abundances. For WDs whose pollution eventually appears to be dry at late stages of accretion, the inferred water abundances remain within the uncertainties of the observed water concentration for up to a few settling timescales, and overall can be thought of as upper limits on water fractions of the accreted parent bodies.

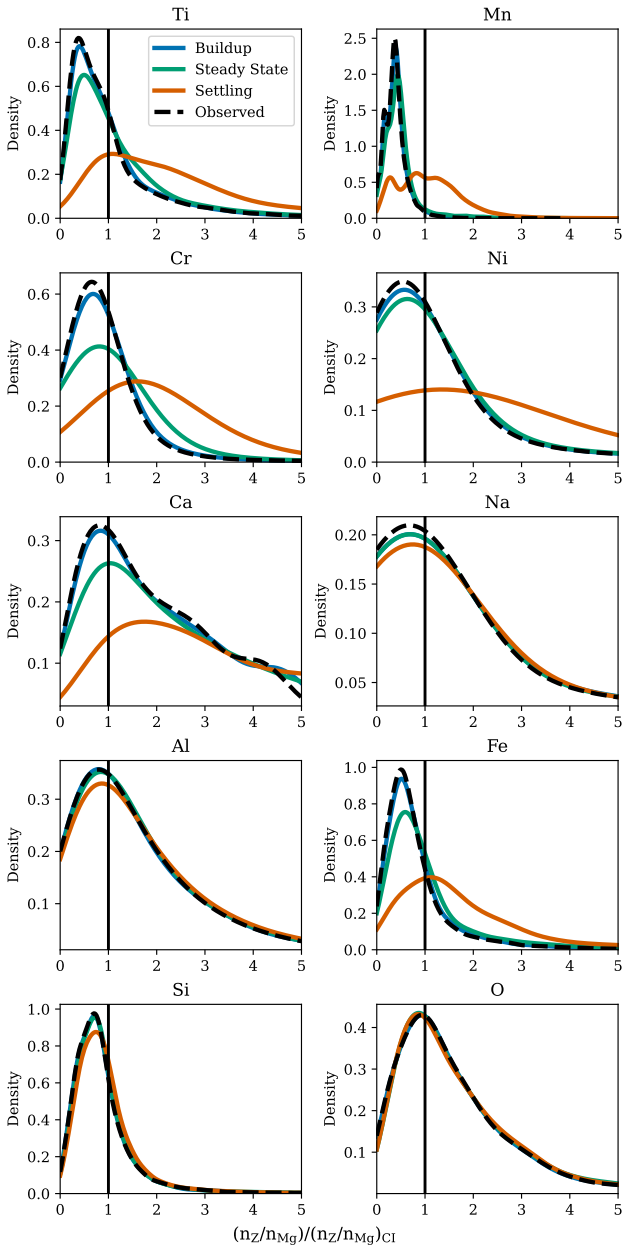

Figure 4.4: The distributions of abundance ratios calculated for the population of WDs in this study at mass-buildup, steady-state, and decreasing times, for a disk timescale of 10^5 yr. The distributions of observed values are shown by the dashed lines, and they generally match the mass-buildup phase values.

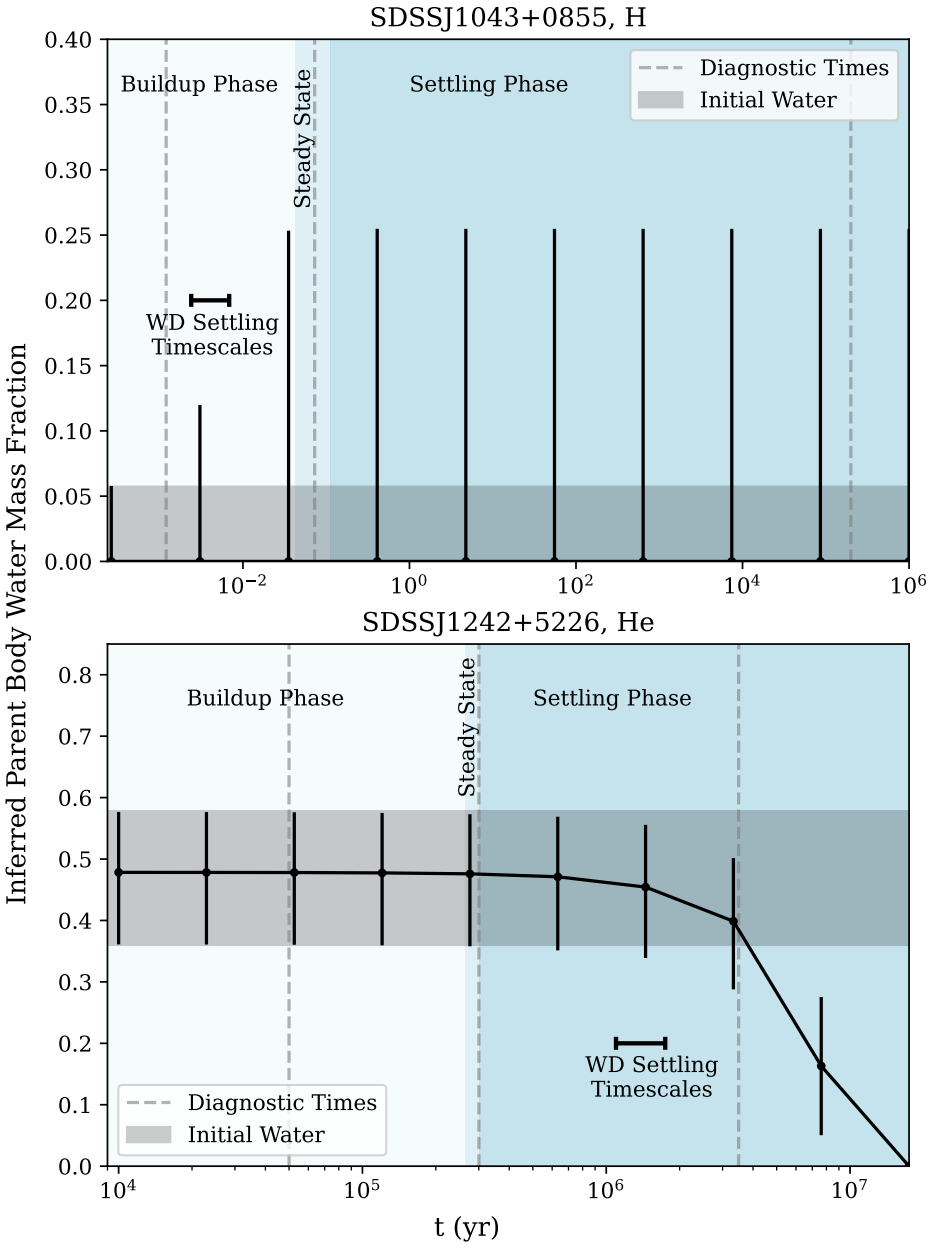

Figure 4.5: Evolution of the inferred water mass fraction calculated over time for two example WDs, for a disk timescale of 10^5 yr. Water fractions with propagated errors are shown at various times during the evolving accretion process. The shaded grey region shows the 1σ water mass fraction calculated from the observed values. The vertical dashed lines show the "diagnostic" times $t_{\rm buildup}, t_{\rm SS}$ and $t_{\rm settling}$ at which we sample water for the buildup, steady state, and settling phases of accretion. The range of settling timescales for each WD are shown by the horizontal bars.

Returning to the full WD sample, we calculate the summed distributions of water mass fractions derived at the three mass-buildup, steady-state, and settling diagnostic times with $\tau_{\rm d} = 10^5$ yr (the relevant times are shown as dashed vertical lines in Figure 4.5). The resulting water distributions for the summed WD sample are shown in panel B of Figure 4.6. As in Section 4.3.1, we emphasize the bimodal distribution defined by "dry" vs "non-dry" accreted bodies by artificially placing pollution with 0% water at 10^{-4}. Inferred water concentrations typically decrease in the mass-settling phase, as relative element settling rates hide any accreted water that may have been present. This is largely due to inferred parent body Fe/Mg increasing exponentially in the mass-settling phase, decreasing O excesses.

Thus far, we have considered a single $\tau_{\rm d}$, and we now allow $\tau_{\rm d}$ to vary to test how disk timescales much longer or shorter than our current estimates of $10^4 - 10^6$ yr would alter inferred water concentrations. While the order of mass-buildup, steady-state, and mass-settling phases will remain the same, the inferred parent body abundances will now vary with both t and $\tau_{\rm d}$ according to Equation 4.3. Panels A and C of Figure 4.6 show the summed distributions of water concentrations across the whole WD sample at each phase of accretion (calculated at the diagnostic times $t_{\rm buildup}, t_{\rm SS}$ and $t_{\rm settling}$) for short and long disk timescales of 10^2 and 10^8 yr, respectively. A short disk timescale leads to more of the pollution appearing dry in the mass-settling phase, though the water concentrations calculated at the mass-buildup and steady-state times tend to be similar to what we found for $\tau_{\rm d} = 10^5$ yr. Conversely, a long disk timescale that exceeds settling timescales and allows element abundance ratios to reach stable limits (Table 4.2) will keep water fractions close to the mass-buildup and steady-state values.

Finally, in panel D of Figure 4.6 we calculate the distribution of water fractions for the whole WD sample setting all non-O elements to CI chondrite ratios ("CI + Observed O"). We find that water fractions do not change as significantly between different disk timescale assumptions when the lithophile elements are restricted to CI chondrite, and therefore only

show an example at $\tau_{\rm d} = 10^5$ yr. We also find that water abundances tend to vary less between different accretion phases. This is because the water concentrations now depend only on the O/Mg ratio, which for most WDs reaches a stable limit or diverges later in the settling phase.

4.3.3 Accretion phases derived from MCMC

As described in Section 4.2.3, we test a variety of MCMC fit procedures for the WD data. For each test, we use Simulated Annealing to find an initial guess for t (the time since the onset of accretion at which the WD is observed) and $\tau_{\rm d}$ (the e-folding timescale of the accretion disk) for the MCMC. We start with generous bounds of 10^{-6} to 10^{10} yr for both timescales in our search. We apply two different likelihood functions, the first calculates a standard log likelihood comparing the observed abundances to the modeled observed abundances based on the timescales and assuming a chondritic parent body. The second likelihood function (referred to hereafter as "weighted") weights the fit by the fraction of the parent body mass that would be in the atmosphere of the WD at the time t. This aims to disfavor solutions which imply very small fractions of the parent body being present, resulting in anomalously high parent body masses. We also run these tests with a prior restricting the disk timescale to $10^3 - 10^7$ yr (within a factor of ten of current disk timescale estimates, Girven et al. 2012).

Without placing strong priors on the disk and observation times, we find that the distribution of best-fitting timescales is usually very broad. This is because abundances typically only vary significantly at late or early times during the accretion process, depending on the relative disk and settling timescales (see Figure 4.1), leading to long periods of time where abundance ratios are relatively constant. Figure 4.7 shows the posterior distributions for t and $\tau_{\rm d}$ for each WD in the MCMC test using a standard log likelihood function and broader $\tau_{\rm d}$ prior. The timescales are transformed to $t/t_{\rm SS}$, where $t_{\rm SS}$ is calculated from $\tau_{\rm d}$ through Equation 4.2. The median value for each distribution is show as the dashed vertical line, with medians to the right of zero indicating that the WD is assigned to the settling phase of accretion and

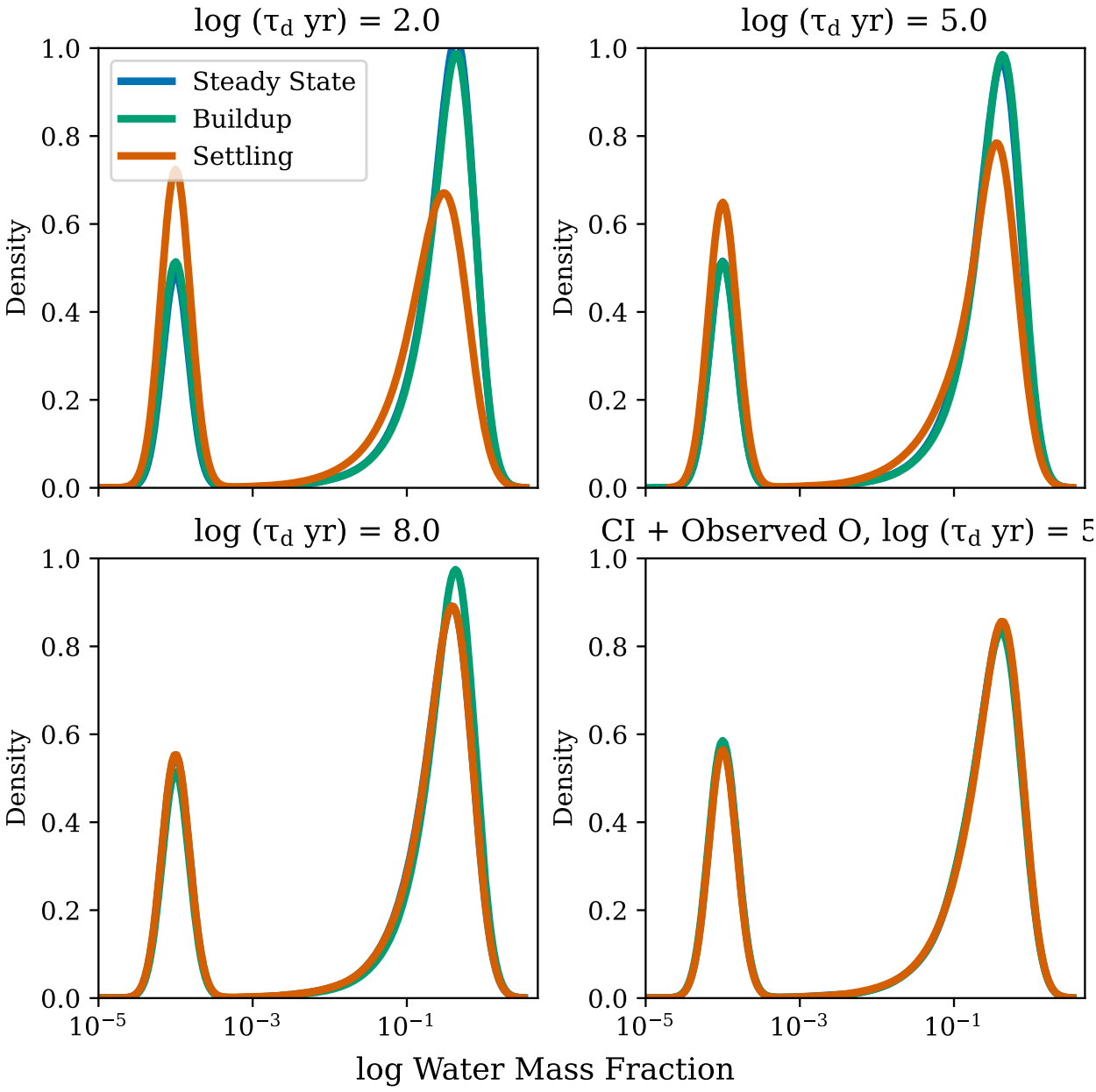

Figure 4.6: Water abundances calculated for mass-buildup, steady-state and mass-settling phase assumptions, at a variety of disk timescales. For visualization, water fractions of zero are inflated to 10^{-4}. The first three panels show water fractions calculated using all observed elements, the last assumes all elements except O are in CI chondrite abundances. Unless the disk timescale is very long compared to the settling timescales, the water abundances in the mass-buildup and steady-state phases are very similar, while the WDs tend to dry out in the mass-settling phase.

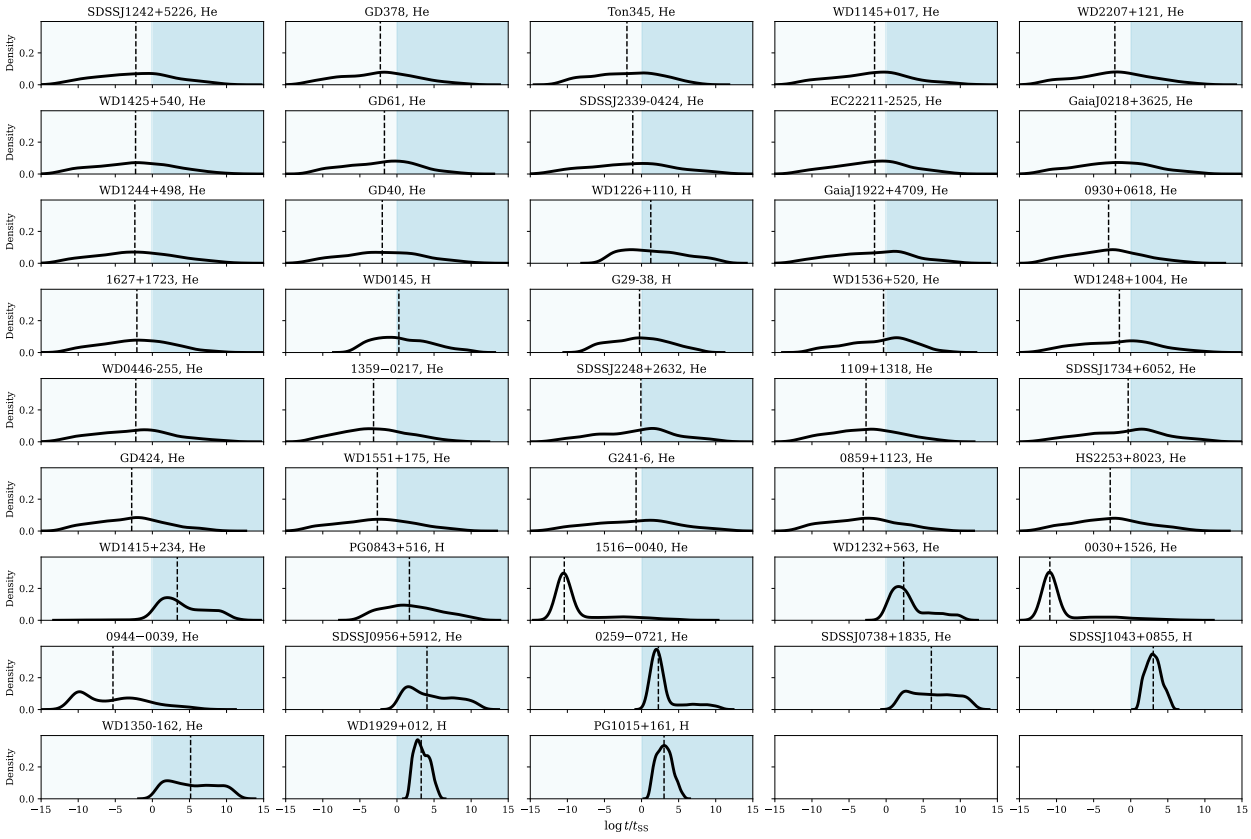

Figure 4.7: The distribution of timescales relative to steady state summed over all WDs in our sample, derived from the posteriors of the MCMC test which uses a standard likelihood function and no strong prior on the disk timescale. Solutions to the left of the vertical line correspond with the mass-buildup phase (light shaded region) while the right is the mass-settling phase (darker shaded region). The median of each WD's distribution is shown as the vertical dashed line. Most WDs have a broad distribution with a peak around steady state.

medians to the left of zero assigned to the buildup phase. Most of the WDs have peaks in posterior probability distributions at or near steady state (peaks close to 1 in Figure 4.7). Interestingly, about half of the H-dominated WDs have a posterior distribution situated fully in the mass-settling phase which is somewhat unexpected as settling is very quick on H-dominated WDs, suggesting it would be unlikely to observed pollution at a later stage. WDs whose observed abundances have poor fits to CI chondrite (WDs towards the bottom of Figure 4.7) tend to have more narrow distributions of $t/t_{\rm SS}$ further away from steady state. As we will discuss later, while deriving parent body abundances from the accretion phases assigned to the WDs that are more constrained in $t/t_{\rm SS}$ does typically improve the fit to CI chondrite, it usually does not provide enough of an improvement to render the sampled polluters statistically indistinguishable from chondrites in the χ^2_ν tests.

To show the effects of the different MCMC procedures, we sum all of the $t/t_{\rm SS}$ distributions across the WD sample for each MCMC test and plot each summed distribution in Figure 4.8. Tests include running the MCMC with the standard and mass-maximizing likelihood functions and with and without a restricted prior on $\tau_{\rm d}$. Applying the weighted likelihood function drives the MCMC solutions towards steady state, as that is when the mass in the atmosphere is at a maximum (Figure 4.8). Amongst the individual WDs, we find that WDs with peaks in the distributions of $t/t_{\rm SS}$ in the settling or near-steady state phases remain the same when the weighted likelihood is applied, but the three WDs with mass-buildup phase solutions in Figure 4.7 move to steady state. Placing a prior on $\tau_{\rm d}$ of $10^3 - 10^7$ yr tends to flatten the distributions in Figure 4.8, with most of the values on the buildup side. Applying the weighted likelihood function in addition to the more restricted prior on $\tau_{\rm d}$ brings the posteriors back to be centered on steady state, again with the exception of any WDs whose distributions peak in the mass-settling phase.

These tests are based on the assumption that the true parent body abundances of each pollution sample are chondritic. To assess that assumption, we use the chain of t and $\tau_{\rm d}$ from

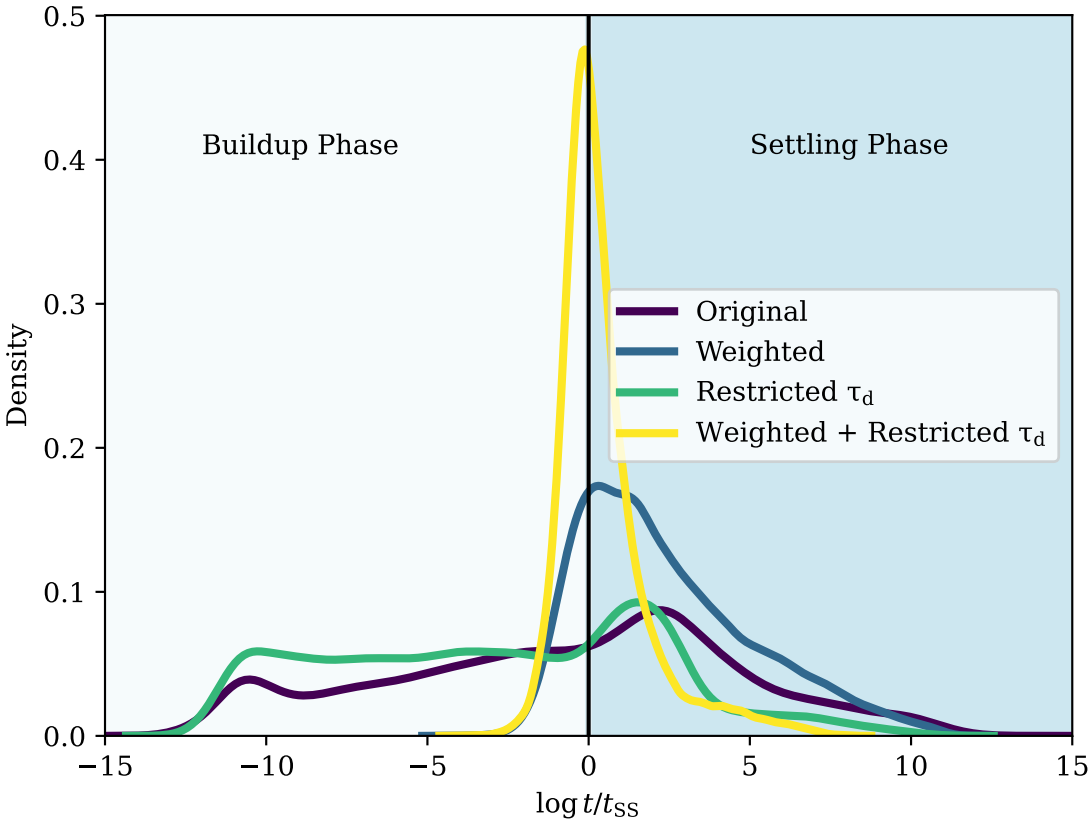

Figure 4.8: The distribution of timescales relative to steady state derived from the posteriors of the MCMC tests. Solutions to the left of the vertical line correspond with the mass-buildup phase while the right is the mass-settling phase. Most of the individual white dwarfs peak around steady state, and have broad distributions. “Weighted" refers to applying a likelihood function that prefers solutions that maximize the mass of pollution in the atmosphere. “Restricted $\tau_{\rm d}$" curves place a restricted prior on the disk timescale of $10^4 - 10^7$ yr, while non-restricted curves allow $\tau_{\rm d}$ to vary freely between 10^{-6} to 10^{10} yr. Applying a weighted likelihood function to prefer solutions that maximize the mass currently in the atmosphere of the white dwarf tends to bring solutions towards the steady-state and mass-buildup phases.

the MCMC and the observed lithophile abundances for the WDs to recover a set of parent body abundances at each draw. We then calculate the χ^2_ν for the fit of these abundances to CI chondrite, and find that 26/41 of the WDs have χ^2_ν distributions for which the majority of the distribution is lower than the critical value for the body passing as chondritic. Applying the weighted likelihood function and/or placing a more restricted prior on $\tau_{\rm d}$ does affect the χ^2_ν distributions, but only moves a handful of WDs from passing to not passing as chondritic, or vice versa.

We use the parent body elemental abundances derived from the MCMC chain to calculate distributions of water mass fractions for each WD. Figure 4.9 shows the individual water distributions for each WD for the MCMC test without a weighted likelihood function or restricted prior on $\tau_{\rm d}$. We find the posterior distributions of parent body water fractions are very broad for most WDs, except for those with no evidence for water ("dry"). Applying a weighted likelihood function minimally changes the shape of the water fraction distributions, and the peaks of the distributions do not change when steady state is preferred by the weighted likelihood. Placing a restricted prior on $\tau_{\rm d}$ similarly has a minimal impact on the water peaks and overall distributions.

We now show the variation in overall water concentrations between the different MCMC procedures by summing over the calculated water distributions for all WDs in each MCMC test (Figure 4.10). As in the previous sections we also calculate water abundances where the lithophile element ratios are set to chondritic abundances, so that the water fraction is driven by the O abundance in the parent body. As before, we find that setting lithophile abundances to chondritic and deriving parent body O ratios from the posterior distributions of t and $\tau_{\rm d}$ does not significantly change the overall distribution. For individual WDs, setting lithophile abundances to CI chondrite ratios has the largest effect on WDs which are placed in the mass-settling phase by the MCMC process, which can inflate parent body Fe/Mg to exceed O/Mg and result in low inferred water fractions.

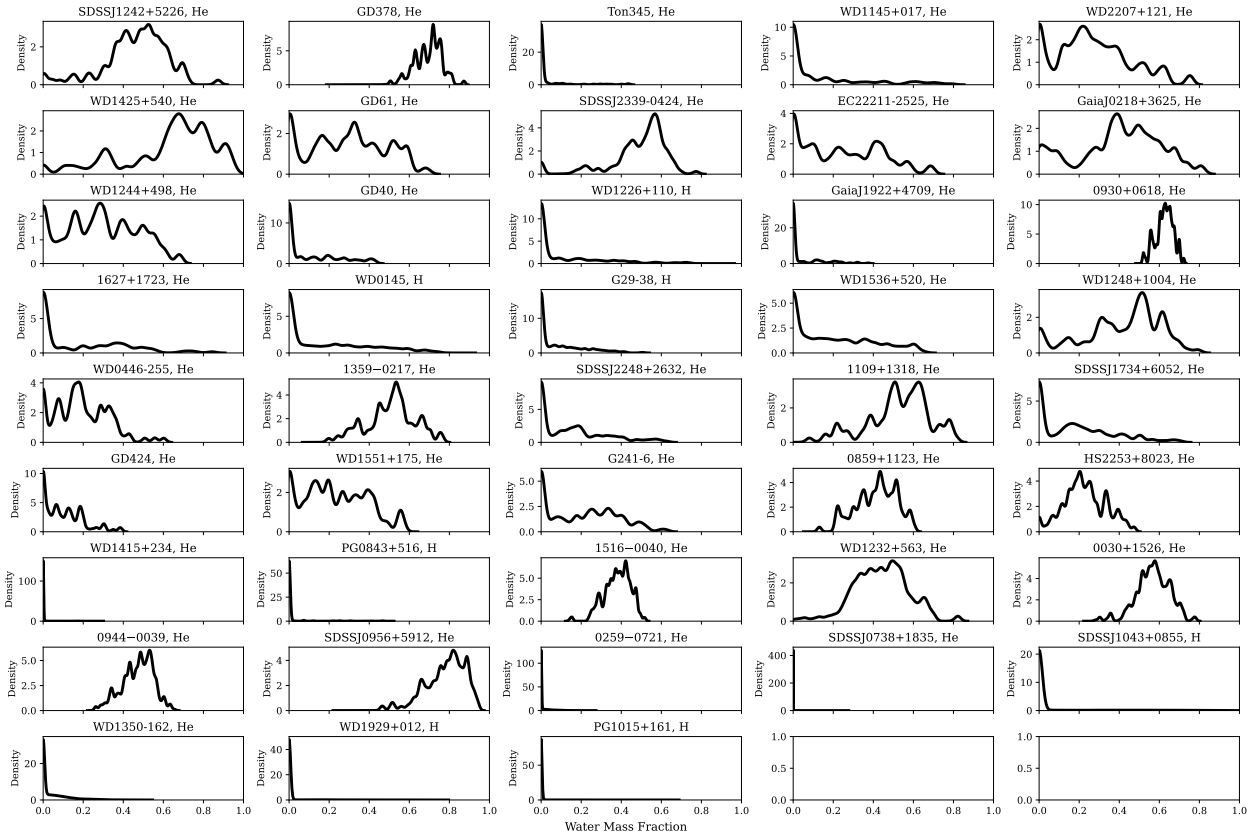

Figure 4.9: The distributions of water mass fractions derived for the WDs, based on the observed abundances and the timescale posteriors of the MCMC test. About a third of WDs are dry, and we typically find a spread of $10-20\%$ in water fractions for wet WDs.

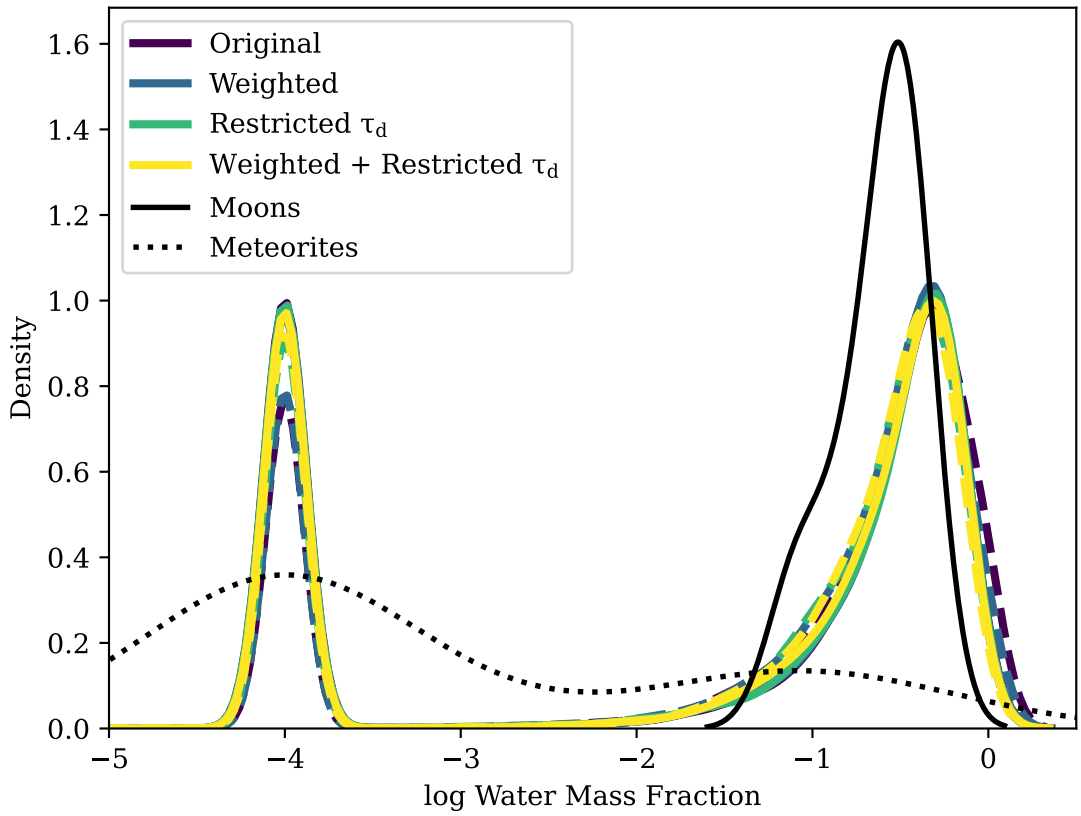

Figure 4.10: The summed water mass fraction distributions for the WDs for each MCMC test. Solid curves derive water mass fractions using observed element ratios and the dashed curve uses observed O with all other elements set to CI chondrite abundances. "Weighted" refers to applying a likelihood function that prefers solutions that maximize the mass of pollution in the atmosphere. "Restricted $\tau_{\rm d}$" curves place a restricted prior on the disk timescale of $10^4 - 10^7$ yr, while non-restricted curves allow $\tau_{\rm d}$ to vary freely between 10^{-6} to 10^{10} yr. The distribution of meteorites is shown in the black dotted curve and largely lacks water while the distribution of solar system moons is shown by the solid black line and is more water-rich.

4.4 Discussion

4.4.1 Implied accretion phases for H and He WDs

In this section we discuss which accretion phases are most likely for H and He-dominated WDs, and as a result what correction factors should be used to recover parent body abundances from observed WDs. Differential settling is the main driver behind changing WD abundance ratios over time. For WDs with short settling times compared to the disk timescale, abundance ratio changes will start early on but quickly reach a stable limit determined by the ratios of settling times. In these cases, if we assume we observe the WD around or after the steady-state point, we should be able to reliably recover parent body compositions. For longer settling timescales, exceeding the disk timescale, recovering true parent body abundance ratios is more complicated as the abundances typically diverge.

H-WDs typically have very short settling timescales, suggesting it is most likely to observed these WDs in the steady-state or mass-settling phase. We test this hypothesis using the H-WDs in our sample. For a disk timescale of 10^5 yr, we do find that the fit to chondrite generally improves after the steady-state point, however for most of the H-WDs the improvement is not enough to bring the abundance ratios into agreement with chondrites. From the MCMC tests, of the 4/7 of the H-WDs whose observed abundances do not pass as chondritic, 3 of these have timescale distributions from the MCMC that favor the settling phase (the fourth favors the steady state, with a tail extending to settling). These 3 H-WDs reach χ^2_ν values in the mass-settling phase that are several orders of magnitude lower than those calculated for the original data. However, these WDs also require incredibly short disk timescales (less than a year) in order to reach chondritic abundances. This would suggest these H-WDs accreted single, massive objects nearly all at once. We do not find similar extremely short disk timescales are necessary to derive the He-WD abundances from CI chondrites. Overall, The H-WDs do support the hypothesis of chondritic bodies in the mass-settling phase, however we would need confidence in the probability of single-body accretion and H-WD

modeling to know which limit, based on disk and settling times, typically applied to H-WDs.

For WDs with longer settling times, such as most He-dominated WDs, systems typically need to reach a mass-settling phase before significant changes are expected in the observed abundance ratios. Of the 23 He-WDs whose observed abundances are a good fit to chondrite, we find that only a few can be forced to fail the χ^2_ν test when it is assumed they are in the mass-settling phase (up to ten times a typical settling time for that WD). In other words, if observed abundances are chondritic, the assumption of a particular accretion timescale does not strongly influence the abundance ratios as long as disk timescales are still shorter than the settling timescales. From the MCMC results, of the 13 He-WDs whose observed abundances are not good fits to chondrite, only a few yield chondritic abundance ratios through the MCMC search, for timescales in the mass-settling phase. Thus, on the assumption of chondritic parent bodies, it does not seem likely that the majority of He-WDs are in a mass-settling phase exceeding more than a few settling timescales. In terms of recovering parent body compositions, the more minor settling adjustments that are made for late phases of accretion less than a few settling timescales do not appear to have a strong influence on abundance ratios. Overall, the relative robustness of abundances until late mass-settling phases, and the extreme sensitivity of late decreasing abundance corrections to assumed time of observation, suggest that He-WD abundances are best used as-observed, with the knowledge that there may be some outlier WDs at late accretion phases.

4.4.2 The distribution of water abundances

Overall, we find a wide range of water mass fractions for the WDs. H-WDs in particular appear to lack significant O-excesses, though this may be explained by asyncrhonous accretion models not considered in this work (e.g. Malamud & Perets, 2016; Brouwers et al., 2023). Our newly presented abundances for WD0145+234 provides somewhat of a counter example, as this WD does have an O excess and a water mass fraction of up to about 25%, however more H-WDs are needed to understand if this is somehow typical. For both H and He-WDs,

we find that the water abundances tend to be robust in the MCMC sampling and selection of different accretion phases. As shown in Figure 4.5, for a given disk timescale, water mass fractions stay within the uncertainty limits of the observed values at least until well past steady state, into the mass-settling phase. The summed water fraction distributions from our different methods vary minimally between different MCMC approaches. Fe abundances appear to have the strongest effect on water fraction, due to the relative abundance of Fe changing especially drastically at late times. Wter fractions calculated with all lithopile abundances set to chondritic values have a negligible difference from those calculated from the observed abundances.

Using the observed values, we find that about a third of the WDs appear to have accreted dry parent bodies, with the rest having accreted rocky bodies with water mass fractions of about 30%, on par with estimates for asteroid 1 Ceres in the solar system, for example (de Sanctis et al., 2015). Figure 4.10 shows the calculated water fraction distributions for the WD population in this study compared to those derived from thermal models for solar system moons by Reynard & Sotin (2023) and those calculated from meteorite abundances (Lodders, 2021). Most of the meteorites are dry, with the exceptions of CI (throughout the paper we remove water for CI chondrites when comparing abundances) and CM which have inferred water mass fractions of $\sim 25\%$ and $\sim 15\%$, respectively, due to the presence of phyllosilicate minerals produced by aqueous alteration. CK and CR chondrites also have non-negligible water abundances of a few percent. While uncertainties for the WD pollution water abundances are typically at least $\sim 10\%$ (Figure 4.5), the overall distribution is consistent with the picture of WD pollution as a mix of dry, rocky material like asteroids and more icy/watery bodies such as KBOs.

While we find a significant fraction of the WDs have accreted dry bodies, most of the WDs in our sample appear to have accreted water-bearing bodies based on O excesses, somewhat contradicting the findings based on H accretion rates that most material is dry

(Jura & Young, 2014). However, we also find that these higher water fractions are supported by corresponding amounts of H in nearly all cases. It is possible that our sample, which represents some of most highly polluted WDs, is simply sampling larger bodies that are either more water rich, or are more efficient at retaining water throughout the post-main sequence and accretion processes, than WDs that are more lightly polluted. This would be consistent with the relatively large parent body masses required to explain most highly polluted WDs (Trierweiler et al., 2022).

4.4.3 Effects of pre-accretion processing on pollution

In this work, we consider effects of accretion and settling on derived parent body abundances. However, there are a few processes prior to accretion that could skew inferred water abundances from the real distribution of exoplanetary material. For example, Malamud & Perets (2017) suggest that evaporation during the post-main sequence evolution of planetary systems could alter water abundances, leading to trends in water concentration with main sequence stellar masses. They argue that more water can be retained by bodies orbiting lower-mass progenitor stars, leading to higher water fractions for low mass WDs. Jura & Xu (2010) suggest water retention rates should also vary with the initial size of the body, with smaller objects drying out more quickly during post-main sequence evolution. Additionally, models for asynchronous accretion of WD pollution suggest water accretion will preferentially occur early times as wet material is sublimated (Malamud & Perets, 2016; Brouwers et al., 2023). As a result of this model, they predict higher temperature WDs, which should cause material to sublimate more quickly, should have lower water abundances.

While we do not find a correlation between water mass fractions and WD mass, we do see a negative correlation between water concentration and WD temperature (Figure 4.11). Calculating the Pearson correlation coefficient, we find a negative correlation of -0.42 with a p-value of 0.005. However, variations in the modeling of WDs can also lead to discrepancies in WD parameters that are temperature or structure dependent (Izquierdo et al., 2023), so

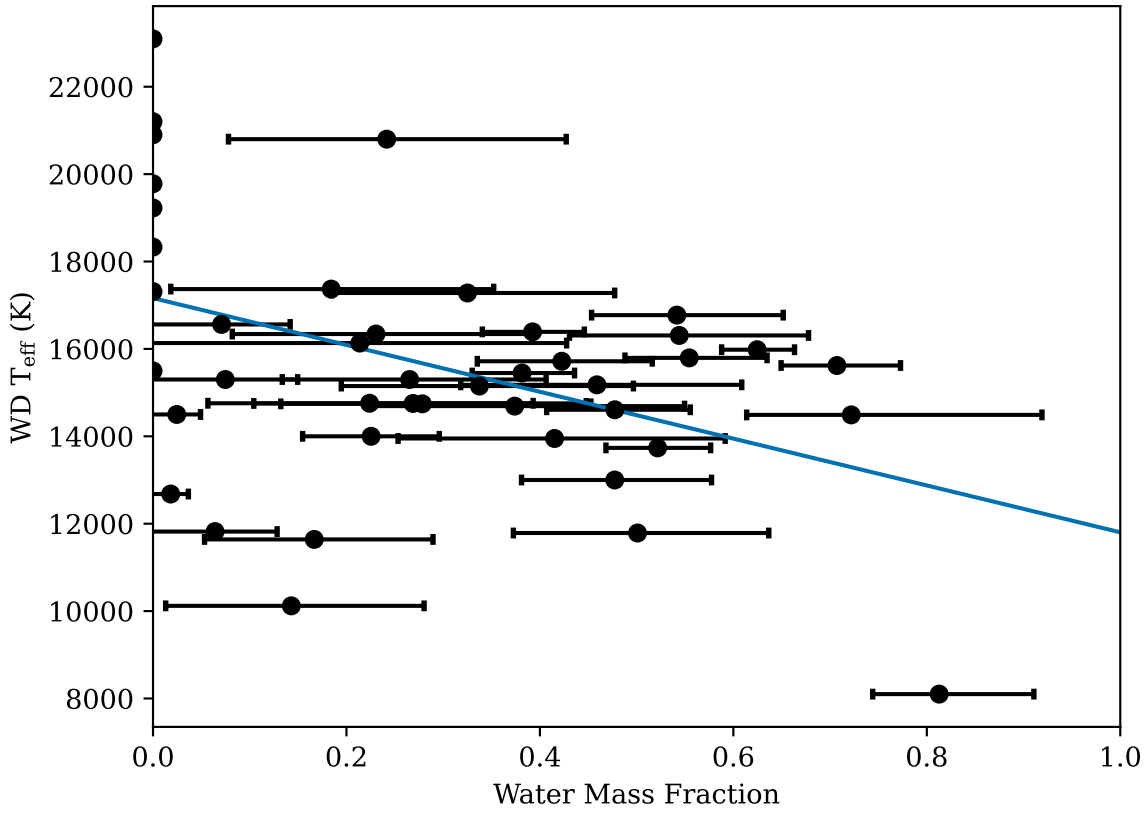

Figure 4.11: We test the correlation between water mass fractions and the temperature of the WD. The blue line shows the best fit line to date, and find a negative correlation of -0.42.

further understanding of modeling systematics should be done before fully attributing low water concentrations to pre-accretion processing. If the effects of asynchronous accretion and post-main sequence sublimation are indeed active, we expect correcting for these effects should shift both the dry and wet ends of the water distribution towards more moderate water fractions, enhancing the peak of the distribution.

4.5 Conclusions

Using a large sample of highly polluted WDs, we infer water mass fractions for exoplanetary material based on excesses of oxygen relative to other rock-forming elements. Overall, the median water content for the polluters in our sample is about 25% by mass, consistent with estimates for typical icy solar system bodies. We find that about a third of the polluting material is dry, and that H-dominated WDs tend to lack significant O excesses compared to He-WDs. Accounting for asynchronous accretion or post-main sequence processing of material may explain the relatively low inferred water abundances for the H-WDs and higher temperature He-WDs.

To explore the impact of different accretion phases and assumed disk timescales on the abundance ratios and resulting water abundances for WDs we applied corrections to the WD data for mass-buildup, steady-state, and mass-settling phases of accretion. We show that inferred abundance ratios and water fractions are usually within range of the observed values through the mass-settling phase, if disk timescale is longer than the settling timescale, or until late times in the mass-settling phase, if disk timescale is less than the settling timescale. For a simple exponential accretion and settling model, correcting abundances for an assumed phase of accretion therefore has a minimal effect except for He-WDs observed after a few settling timescales (assuming typical disk timescales of $10^4 - 10^6$ yr).

Finally, under the hypothesis that WD pollution is typically chondritic in composition, we ran several MCMC tests to outline the distribution of accretion timescales that best explain the observed pollution. From these tests, we find that most WDs are consistent with being in a steady-state or mass-settling phase (including H-WDs). However, we generally find very broad posterior distributions for the disk and observation timescales, a result of abundance ratios being relatively stable except at the very early or very late stages of accretion.

CHAPTER 5

Atmosphere Loss by Aerial Bursts

5.1 Introduction

The initial atmosphere of the Earth and other terrestrial planets was likely established by an interplay of diverse loss and delivery processes. Relevant processes that could deliver volatiles to a planet's atmosphere include, for example, degassing of volatiles during planetesimal impacts (e.g. Abe & Matsui, 1985; Zahnle et al., 1988), volcanic outgassing (e.g. Craddock & Greeley, 2009; Elkins-Tanton, 2012), tectonic activity Zahnle et al. 2007), and accretion of hydrogen-helium gas from the primordial gas disk (e.g. Lammer et al., 2014; Ginzburg et al., 2016).

As volatiles build up in the atmosphere, depending on composition and other planet properties, atmospheric mass may be lost due to high energy radiation from a planet's host stars (e.g. Kulikov et al., 2007; Owen & Wu, 2013), core-powered mass loss (Ginzburg et al., 2018; Gupta & Schlichting, 2019), or impacts (e.g. Melosh & Vickery, 1989; Genda & Abe, 2003; Zahnle et al., 1992; Schlichting et al., 2015; Wyatt et al., 2020).

Observed and inferred evidence for impacts of small planetesimals are plentiful within our own solar system. Impacts can explain variations in atmospheric mass between moons such as Titan, Ganymede and Callisto (Zahnle et al., 1992), and may be responsible for the erosion of Mars' atmosphere (Melosh & Vickery, 1989). Evidence for Earth impacts can be seen in the presence of our Moon (Cameron & Ward 1976, Canup & Asphaug 2001), the cratering

on the Moon and Earth, and the geochemical traces of the late veneer (Warren et al. 1999, Walker et al. 2004, Walker 2009). Aside from atmosphere loss, impacts are important to Earth's history as they are theorized to have delivered volatiles to the surface (Owen & Bar-Nun 1995, Dauphas 2003). They are one possible source of water for our oceans and for organic molecules (Chyba, 1990), though the types of impactors (asteroid, comet, planetary embryo, etc.) that could have delivered this material are still under debate.

When considering atmospheric mass-loss by impacts, it is instructive to distinguish between giant impacts and planetesimal impacts. A giant impact is a planetary scale collision that can lead to global atmospheric mass-loss, whereas a planetesimal impact can only eject mass locally above the tangent plane. Although giant impacts can eject significantly more mass in a single event than a planetesimal impact, planetesimal impacts are more efficient than giant impacts, since they produce more atmospheric loss per impactor mass (Schlichting et al., 2015).

Depending on impactor sizes, impact velocities and impact angles, volatiles may be added to or removed from growing planetary embryos by planetesimal impacts (e.g. Shuvalov, 2009; Schlichting et al., 2015; Wyatt et al., 2020; Sinclair et al., 2020). Past works that have focused on evaluating the collective impact on atmospheric erosion by a population of planetesimal impactors of varying sizes have concentrated on ground explosions (Schlichting et al., 2015; Wyatt et al., 2020), i.e. impactors large enough that they hit the ground. In this paper we focus on planetesimal impactors that are significantly decelerated in the atmosphere (Shuvalov et al., 2014, 2016) and evaluate their contribution to atmospheric loss of terrestrial planets and Neptune-like planets and exoplanets.

To study the role of small impactors in atmospheric loss and evolution, we build on previous work by Schlichting et al. (2015), who derived a simple analytic atmospheric mass-loss model for planetesimal impacts, which successfully captured previous numerical results by Shuvalov (2009). We expand on the work by Schlichting et al. (2015) first by accounting for impactors

which do not reach the ground and instead explode as aerial bursts, and second by including both isothermal and adiabatic atmospheric profiles in our model.

By reasoning that aerial bursts deposit most of their energy at a location in the atmosphere where they reach roughly half of their initial velocity, we calculate the atmospheric properties required for a planet to lose atmospheric mass by aerial bursts. We demonstrate that aerial burst-induced mass loss is only significant for planets with atmospheric densities comparable to the impactor density and quantify the resulting atmospheric mass loss by applying our model to Neptune-like planets and exoplanets.

This paper is structured as follows: In section 5.2 we outline our approach for calculating atmosphere loss by considering a simple impactor explosion model. In section 5.3 we apply our model to aerial bursts and present results for Neptune-like atmosphere in section 5.4. We outline general planet parameters for which mass loss by aerial bursts is important in section 5.5. In section 5.6 we discuss the contributions of aerial bursts to the total atmospheric mass loss. Finally, we summarize our findings in section 5.7.

5.2 Methods

5.2.1 Atmospheric Profiles

Before presenting our mass loss model, we first describe the two atmospheric profiles assumed throughout this work, and the mass loss limits associated with each profile. We consider isothermal and adiabatic atmospheres with the following density profiles:

$$\begin{aligned} \rho(z) &= \rho_o e^{-z/h} \quad \text{(Isothermal)} \\ \rho(z) &= \rho_o \left(1 - \frac{\gamma - 1}{\gamma}\frac{z}{h}\right)^{1/(\gamma-1)} \quad \text{(Adiabatic)} \end{aligned} \tag{5.1}$$

Here $h = \frac{k_B T}{\mu m_p g}$ is the scale height, where k_B is the Boltzmann constant, T is the temperature, μ is the mean molecular weight, m_p is the proton mass, and $g = \frac{GM_p}{R^2}$ is the gravitational acceleration for a planet of mass M_p and radius R. The atmospheric density ρ is a function

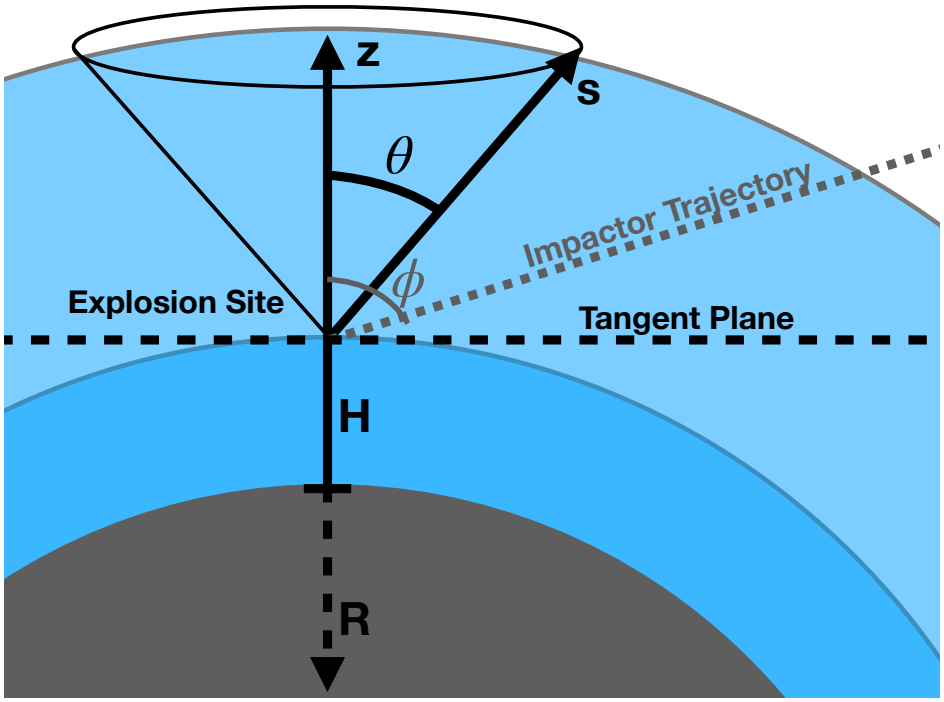

Figure 5.1: Diagram of an aerial burst. The planet has a radius R and an atmosphere with a scale height h. The planetesimal enters the atmosphere along the grey dashed line with an angle ϕ relative to the normal above the explosion site. It explodes as an aerial burst at height H above the ground. From the explosion site, we define z to be the height above the explosion ($z = 0$ at the height H), and s to be a column of atmosphere at an angle of θ from z. For an aerial burst occurring at height H, the maximum mass of atmosphere which can be ejected is roughly the cap of atmosphere out to the tangent plane ($\theta = \pi/2$).

of z, the height in the atmosphere above the ground. ρ_o is the density of the atmosphere at the planet's surface and γ is the adiabatic index. Throughout this work we assume a diatomic atmosphere with $\gamma = 1.4$ so that the adiabatic profile is $\rho(z) = \rho_o \left(1 - \frac{2}{7}\frac{z}{h}\right)^{5/2}$. The atmosphere extends from $z = 0$ to $z = \infty$ for the isothermal profile and to $z = 7h/2$ for the diatomic, adiabatic profile.

Using a coordinate system centered on the impact site (see figure 5.1), and assuming $h \ll R$, we can write our coordinates as $s = \sqrt{R^2 \cos^2\theta + 2zR} - R\cos\theta$ or $z = (s^2 + 2Rs\cos\theta)/2R$. We note that the assumption of $h \ll R$ means that the density of the atmosphere will decrease quickly with height, so that the density profile will be close to zero for heights of

$z \gg R$. All aerial bursts will therefore occur at heights $H \ll R$. An additional benefit of the assumption $h \ll R$ is that the height of the aerial burst H only factors in the density profile, and not in z or s, simplifying many of the following equations.

Assuming $h \ll R$, the total mass in the atmosphere for both the isothermal and adiabatic profiles is well approximated by

$$M_{tot} \simeq 4\pi R^2 \int_0^{z(\rho \to 0)} \rho(z) dz = 4\pi \rho_o h R^2. \tag{5.2}$$

The maximum mass of atmosphere that can be ejected by an aerial burst at height H is roughly the cap of atmosphere above the tangent plane. We call this mass $M_{cap}(H)$, and calculate it as

$$M_{cap}(H) = 2\pi \int_0^{\pi/2} \int_0^{z(\rho \to 0)} \rho(z + H) s^2 \sin(\theta) ds d\theta. \tag{5.3}$$

For an explosion on the ground ($H = 0$), the cap mass for each profile is $M_{cap,Iso} = 2\pi \rho_o h^2 R$ and $M_{cap,Adi} = \frac{14}{9} \pi \rho_o h^2 R$.

5.2.2 Mass Loss Model

We model each aerial burst as an explosion at the height in the atmosphere where drag forces significantly decelerate the body. Specifically, we choose the height where drag forces slow the impactor to half of its initial velocity, such that the impactor's momentum is halved and its kinetic energy is 1/4 of the initial kinetic energy. The assumption that the half velocity height is the explosion height is a reasonable approximation because the atmospheric density increases exponentially (or as a steep power-law in the adiabatic case) as the body approaches the surface such that it experiences most of its deceleration around this half-velocity height.

The direction of the impact trajectory is parameterized by the angle ϕ, which is measured from the normal above the explosion site (see figure 5.1), such that $\phi = 0$ represents a

vertically falling impactor. The impactors' initial velocity is v_∞. We account for impactors approaching the planet at any angle, so that the half-velocity height is a function of both the radius of the impactor and the trajectory angle ϕ. We outline this half velocity calculation in section 5.2.3. Smaller impactors are decelerated to half their initial velocity higher in the atmosphere than larger impactors. Additionally, impactors travelling on nearly horizontal trajectories will pass through more atmosphere than those following vertical trajectories, and so the horizontal impactors will have relatively higher half-velocity heights. Bodies which decelerate to half their initial velocity before hitting ground are referred to as aerial bursts, while those that reach the ground with more than half of their initial velocity are referred to as ground explosions.

At the calculated explosion height, we model the effect of each impactor as a spherically symmetric point explosion. As the impactor travels through the atmosphere, it creates a shock which heats the gas ahead of it (Zel'dovich & Raizer 1967, Vickery & Melosh 1990). When the impactor decelerates, either by hitting the planet's surface or through drag forces, the heated gas expands as a vapor plume. The plume expands in the atmosphere, transferring momentum to the surrounding gas. Any gas in the plume that is accelerated to the escape velocity of the planet is then ejected. This expanding plume can be well modeled by an explosion placed at the point where the impactor deposits most of its energy in the atmosphere (Vickery & Melosh 1990). The explosion is modeled as an isotropic sphere of the same mass as the impactor, expanding at the same velocity. The energy of this expanding mass is then transferred to the surrounding atmosphere.

We note that this point explosion model is a simplified approach to calculating atmosphere loss, and may not capture the nuances of atmosphere loss detailed in fluid and semi-analytical simulations (e.g., Shuvalov, 2009; Shuvalov et al., 2014, 2016; Boslough et al., 1995; Newman et al., 1999). However, we show in section 5.2.4 that we can generally recover the major elements of the more recent simulations, such as explosion height, so that our model provides

a simple and scale-able way to assess aerial-burst induced mass loss for any given atmospheric parameters.

In each explosion, we distribute the energy of the impactor over the full sphere around the half-velocity point. In this model, the atmospheric mass that will be ejected is the cone of atmosphere which can be accelerated by the impactor's explosion to the planet's escape velocity. The remainder of the explosion energy which does not contribute towards atmosphere loss is dissipated into the surrounding gas. We define the maximum angle along which atmosphere can be ejected to be θ_m. Assuming energy conservation, this angle is where the atmospheric mass per solid angle is equal to impactor mass ($M_i = \frac{4\pi}{3} r^3 \rho_i$) distributed over a sphere and scaled by the final and escape velocities:

$$\int_0^{s(\rho \to 0)} \rho(z + H) s^2(\theta_m) ds = \frac{M_i}{4\pi} \frac{v_f^2}{v_e^2}. \tag{5.4}$$

Here v_f is the velocity of the impactor when it reaches the explosion site, v_e is the escape velocity of the planet, and $s(\theta_m) = \sqrt{R^2 \cos^2 \theta_m + 2zR} - R \cos \theta_m$.

We generally assume that the impactors are rocky bodies approaching the planet at $2v_e$, the velocity we would expect for a body such as an asteroid. We also consider comet-like bodies, which have lower densities and expected initial velocities around $5v_e$.

The total mass lost is then found by integrating over the cone of material out to θ_m

$$M_{eject} = 2\pi \int_0^{\theta_m} \int_0^{s(\rho \to 0)} \rho(z + H) s^2 \sin \theta ds d\theta. \tag{5.5}$$

Throughout this work, we will provide both integral forms and approximated analytical solutions where applicable. For all figures, we numerically solve the integrals by quadrature using the SCIPY package.

5.2.3 Half Velocity Heights

In the point explosion model for impactors, we assume the explosion occurs at the height where the impactor is slowed to half its initial velocity by drag forces. To calculate this half velocity height, we calculate the velocity of the body as a function of the height of the impactor above the ground.

Bodies will always approach a planet with at least the escape velocity, and asteroid and comet-like bodies are expected to be travelling at even higher speeds. Because we are considering atmospheres for which $h \ll R$, any significant deceleration the impactor experiences due to gas drag will occur over a relativity short distance compared to R and within heights significantly smaller than R above the ground. As such, in calculating the impactor's velocity we account for the drag force but neglect any additional gravitational acceleration the impactor experiences as it is always either too weak or acting on too short of a timescale to significantly change the body's velocity before the body reaches $1/2v_\infty \geq v_e$. We can verify that this approximation is justified by taking the ratio of the drag force and gravitational force, $(R/r)(\rho_o/\rho_i)(v_\infty/v_e)^2$, and confirming that it is indeed greater than ~ 1, usually much greater, for the atmospheric densities and aerial burst impactor sizes investigated here.

Drag forces will flatten the bodies as they travel through the atmosphere, so we add a parameter α to the area of the body (Area $= \alpha\pi r^2$). While the body should flatten more over the course of its trajectory through the atmosphere, we will set α to be a constant for now. Based on numerical simulations (Shuvalov et al. 2014), assuming an increase in radius of about 3 is reasonable, resulting in $\alpha = 9$. We note that while this flattening is due to fragmentation of the body, the impactor is still expected to continue travelling as a single entity. Smaller fragmenting pieces will fill in the gaps between larger fragments, allowing us to model the impactor as a falling pancake (Hills & Goda, 1993). With the α parameter for flattening, the equation for the drag force acting on the impactor becomes

$$F_d = \frac{1}{2} C \rho(z) \alpha \pi r^2 v^2, \tag{5.6}$$

where $\alpha\pi r^2$ is the impactor's effective cross section, v is the velocity, r is the impactor radius, and C is the drag coefficient. For a sphere, $C = 0.5$, however the flattened shape of the impactor will change the drag coefficient. Coefficients for non-spherical, rough bodies at high speeds can reach 1 or higher, so we will assume $C = 1$.

The equation of motion for the impactor is therefore

$$\frac{v dv}{ds} = -\frac{1}{2} \alpha C \rho(z) \pi r^2 v^2 / M_i. \tag{5.7}$$

We note that the impactor's velocity will depend on the angle ϕ of the impactor's trajectory through the atmosphere, measured relative to the vertical axis z (see figure 5.1). For a given ϕ, we can solve equation 5.7 for the velocity of the body at a height H above the ground, finding

$$\ln\left[\frac{v(H,\phi)}{v_\infty}\right] = -\frac{3}{8}\frac{\alpha C}{r \rho_i} \int_{s(\rho\to 0)}^{0} \rho(z+H) ds, \tag{5.8}$$

where ρ_i is the density of the impactor, $s = \sqrt{R^2 \cos^2\phi + 2zR} - R\cos\phi$, and ϕ is the angle from the vertical along which the impactor moves through the atmosphere.

Finally, defining the height H to be where the velocity of the body slows to half of its initial velocity ($v(H,\phi) = \frac{1}{2} v_\infty$), we find

$$\begin{aligned} \ln(1/2) &= -\frac{3}{8}\frac{\alpha C}{r \rho_i} \int_{s(\rho\to 0)}^{0} \rho(z+H) ds \\ &\text{or equivalently,} \\ \ln(1/2) &= -\frac{3}{8}\frac{\alpha C}{r \rho_i} \int_{z(\rho\to 0)}^{0} \frac{\rho(z+H) R}{\sqrt{R^2 \cos^2\phi + 2zR}} dz, \end{aligned} \tag{5.9}$$

where H is the half velocity height.

For trajectory angles $\phi \ll \pi/2$ (i.e., vertical trajectories close to the z axis), we can approximate the half velocity height in equation 5.9 as a function of the trajectory angle ϕ, and the radius of the body r:

$$\begin{aligned} \frac{H}{h}_{Iso}(r,\phi) &= \ln\left(\frac{3}{8}\frac{\alpha C}{\ln 2}\frac{h}{r}\frac{\rho_o}{\rho_i}\frac{1}{\cos\phi}\right) \\ \frac{H}{h}_{Adi}(r,\phi) &= \frac{7}{2}\left[1-\left(\frac{8}{3}\frac{\ln 2}{\alpha C}\frac{r}{h}\frac{\rho_i}{\rho_o}\cos\phi\right)^{2/7}\right], \end{aligned} \tag{5.10}$$

where h is the scale height, the densities of the atmosphere and impactor are ρ_o and ρ_i, respectively, C is the drag coefficient, and the α is the flattening parameter.

Numerical solutions for the half velocity heights in isothermal and adiabatic profiles, illustrating two different ϕ angles, are found in figure 5.2. These heights are calculated for an Earth-like atmosphere. We see that larger impactors have lower half velocity heights. Comparing the explosion heights for the vertical ($\phi = 0$) and horizontal ($\phi = \pi/2$), and isothermal and adiabatic cases, we see that the heights for horizontal trajectories are higher by up to a factor of two for an Earth-like atmosphere. This difference is because impactors on horizontal trajectories must pass through more atmosphere than those on vertical trajectories. Impactors in an adiabatic atmosphere also have an upper limit on the half velocity height as the atmosphere extends only to $z = 7h/2$.

5.2.4 Comparing analytical and numerical half velocity heights

We compare our derived half velocity heights with those obtained by Shuvalov et al. (2014, 2016) using hydrodynamical simulations (figure 5.3). These works investigated impactors entering two types of atmospheres - one analogous to Earth's current atmosphere ($h = 8$ km, $\rho_o = 1.2$ kg/m^3) and one representing a primordial atmosphere ($h = 40$ km, $\rho_o = 49$ kg/m^3). The two works included simulations for both asteroid and comet impactors, with a variety of assumed initial velocities.

In figure 5.3, we compare the half velocity heights calculated in the numerical simulations

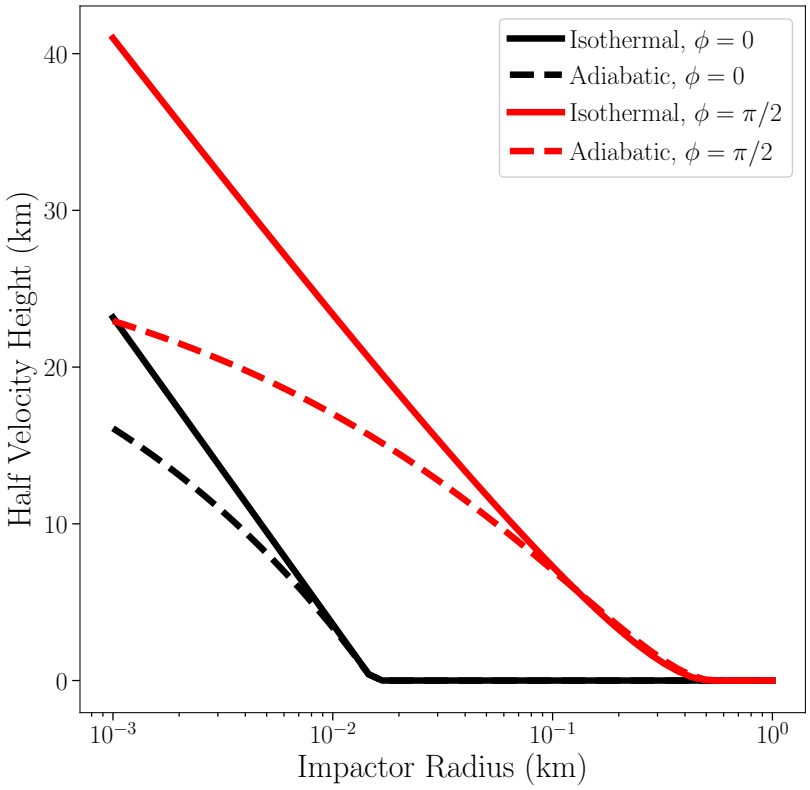

Figure 5.2: Calculated half velocity heights as a function of impactor radius (equation 5.10), for asteroids ($\rho_i = 3300$ kg/m^3, $v_\infty = 2v_e$) impacting an Earth-like atmosphere ($h = 8$ km, $\rho_o = 1.2$ kg/m^3). The solid curves show the isothermal profile, while the dashed curves show the adiabatic profile. The black curve is calculated for a vertical impactor trajectory ($\phi = 0$), and the red curve is for a horizontal trajectory ($\phi = \pi/2$).

(Shuvalov et al., 2014, 2016) to our analytical half velocity heights. The circular points indicate numerical heights calculated for the $h = 8$ km atmosphere while the triangular points represent the numerically calculated heights for the denser, $h = 40$ km atmosphere. Red points represent simulations of comets ($\rho_i = 1000$ kg/m^3) and black points represent asteroids ($\rho_i = 3000$ kg/m^3). Due to the sensitivity of the numerical simulations to initial conditions, some impactor radii have multiple corresponding half velocity heights. For clarity we selected only the 45° data from both Shuvalov studies to show in figure 5.3.

The solid and dashed curves in figure 5.3 are the analytical half velocity heights described by equation 5.10. The solid curves are calculated assuming an isothermal atmosphere, while the dashed curves are for adiabatic atmospheres. The thicker curves are heights calculated for the $h = 40$ km, $\rho_o = 49$ kg/m^3 atmosphere while the thin curves at lower heights are for the $h = 8$ km, $\rho_o = 1.2$ kg/m^3 atmosphere. As with the numerical points, the red curves correspond to half velocity heights for comets while the black curves correspond to the half velocity heights calculated for impactors from the asteroid belt. We find that our analytical expression for the half velocity height is in reasonable agreement with numerical results for both type of atmospheres as well as for cometary and asteroidal impactors.

In our mass loss model described below, we will assume that the half velocity height is the location of the point explosion.

5.3 Mass loss by aerial bursts

The aerial burst atmospheric mass loss regime includes any impactors which can eject atmosphere and which slow to half their initial velocity before reaching the planet's surface. As described in section 5.2, aerial bursts are modeled as explosions at the height H above the ground. At this height, the expanding mass is distributed over the whole sphere around the explosion point.

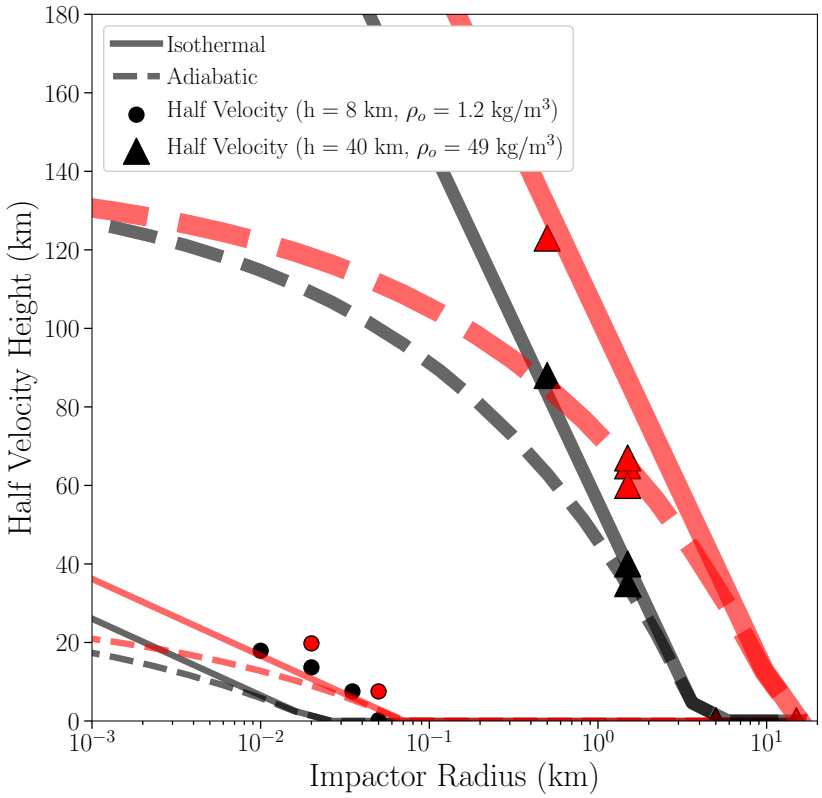

Figure 5.3: Comparison of analytical half velocity heights to those calculated in hydrodynamics simulations. The analytical heights are calculated using equation 5.10 and the simulated heights are from Shuvalov et al. 2014 and Shuvalov et al. 2016. The circular points are from Shuvalov et al. 2016 and correspond to numerical heights calculated for an Earth-like atmosphere ($h = 8$ km, $\rho_o = 1.2$ kg/m^3). The triangular points are from Shuvalov et al. 2014 for a primordial Earth atmosphere ($h = 40$ km, $\rho_o = 49$ kg/m^3). The solid curves are calculated using an isothermal profile while the dashed lines are calculated with an adiabatic profile. The thin curves are the analytical heights for the Earth atmosphere while the thick curves are for the primordial Earth atmosphere. The red curves and points represent impactors with comet properties ($\rho_i = 1000$ kg/m^3) while the black curves and points are asteroid-like impactors ($\rho_i = 3300$ km/m^3). We find that the numerical half velocity heights for both the Earth and primordial Earth atmospheres are in reasonable agreement with the analytical curves, for both comet and asteroid impactors.

To calculate the total mass loss due to aerial bursts, we first pick a height H and trajectory angle ϕ between 0 and $\pi/2$, and then calculate the impactor radius corresponding to this explosion height given the trajecotry angle (equation 5.10). Following the explosion model outlined in section 5.2, we then calculate the maximum angle along which an impactor of the calculated radius can eject atmosphere (θ_m in equation 5.4). Noting that the final velocity of the aerial burst is half of its initial velocity ($v_f = v_\infty/2$), we write equation 5.4 as:

$$\int_0^{s(\rho\to 0)} \rho(z+H, z = s^2/2R + s\cos\theta_m)s^2 ds = \frac{r^3}{12}\rho_i \frac{v_\infty^2}{v_e^2}. \tag{5.11}$$

Using this angle θ_m and equation 5.5, we calculate the mass ejected. This yields mass loss as a function of impactor radius and trajectory angle at a given height. We then sum over the explosion heights in order to find the overall expected mass loss as a function of impactor radius and trajectory angle.

5.3.1 Characteristic Radii

Two limiting impactor radii define the bounds of atmospheric mass loss by aerial bursts. $r_o(\phi)$, which describes the impactor radius corresponding to an explosion height of zero for a given trajectory angle, sets the upper limit for the radius of aerial burst projectiles. At radii larger than $r_o(\phi)$, impactors will result in ground explosions. $r_{min}(\phi)$, the minimum impactor radius that can eject mass from a given trajectory angle, sets the lower radius limit for planetesimals that will result in any mass loss. As such, aerial burst mass loss can occur only when $r_{min} < r < r_o$, where r is the planetesimal radius.

Starting with the equations relating the half velocity height, trajectory angle, and impactor radius (equation 5.10), we solve for the impactor radius where the explosion height is zero. Rewriting equation 5.10 for the case where $r_o(\phi) = r(\phi)|_{H=0}$ gives

$$\frac{r_o}{h}(\phi) = \frac{3}{8}\frac{\alpha C}{\ln 2}\frac{1}{\rho_i}\int_{z(\rho\to 0)}^{0}\frac{\rho(z)R}{\sqrt{R^2\cos^2\phi + 2zR}}dz. \tag{5.12}$$

In the limit where $\phi \ll \pi/2$, we find

$$\frac{r_o}{h}_{Iso,Adi}(\phi) = \frac{3}{8}\frac{\alpha C}{\ln 2}\frac{\rho_o}{\rho_i}\frac{1}{\cos\phi}. \tag{5.13}$$

Note that the approximated form of $r_o(\phi)$ is equivalent for both the isothermal and adiabatic profiles.

r_{min} is calculated by considering the smallest planetesimal that will be able to eject mass from it's associated explosion height. At a given height, the minimum mass that may be ejected in an explosion is the column of atmosphere directly above the explosion site, so we first solve equation 5.4 for the impactor radius required to eject mass along the vertical z axis, or equivalently along $\theta_m = 0$. With the condition that $s(\theta_m = 0) = z$, we can rewrite equation 5.4 as

$$\int_0^{z(\rho\to 0)}\rho(z + H(r_{min},\phi))z^2dz = \frac{\frac{4\pi}{3}\rho_i r_{min}^3}{4\pi}\frac{v_f^2}{v_e^2}, \tag{5.14}$$

where r_{min} is the radius required to eject the column of mass directly above an explosion site at height H, ϕ is the trajectory angle relative to the z axis, ρ_i is the impactor density, v_f is the final velocity of the body at height H, and v_e is the escape velocity of the planet. As defined in section 5.2, the explosion height H depends on both the radius of the planetesimal and the trajectory angle ϕ.

Substituting the expression of half velocity height for H, with a planetesimal radius of r_{min} and a trajectory angle of ϕ ($H = H(r_{min},\phi)$) in equation 5.10, and noting that $v_f = \frac{1}{2}v_\infty$ at the half velocity height, we calculate $r_{min}(\phi)$ for $\phi \ll \pi/2$ as

$$\begin{aligned}
\frac{r_{min}}{h}_{Iso}(\phi) &= \sqrt{64\frac{\ln 2}{\alpha C}\frac{v_e^2}{v_\infty^2}\cos\phi} \\
\frac{r_{min}}{h}_{Adi}(\phi) &= 12^{7/10}\left(\frac{v_e}{v_\infty}\right)^{7/5}\left(\frac{\rho_i}{\rho_o}\right)^{2/5}\left(\frac{8}{3}\frac{\ln 2}{\alpha C}\cos\phi\right)^{11/10}.
\end{aligned} \tag{5.15}$$

We note that for a given total atmospheric mass, $r_{min}(\phi)$ in an adiabatic atmospheric profile will be somewhat lower than the $r_{min}(\phi)$ for the isothermal case. In other words, adiabatic aerial burst mass loss can occur at smaller impactor radii than isothermal aerial burst mass loss.

Finally, using the expression for r_o (equation 5.13) and the equation for the velocity evolution (equation 5.8), we can verify that the half velocity height is a good first order approximation for the location associated with the peak rate of energy deposition by the impactor into the atmosphere in the aerial burst regime. The specific energy deposited at a given height depends on $v\frac{dv}{dz}$. The peak of the energy deposition therefore occurs at the height where $\frac{d}{dz}\left(v\frac{dv}{dz}\right) = 0$. Using the velocity expression from equation 5.8, and considering trajectory angles of $\phi \ll \pi/2$, we derive the peak energy deposition heights H_{peak}. Expressing these heights relative to the half velocity heights of equation 5.10, we find:

$$\begin{aligned}
\frac{H_{peak}}{H_{1/2}}_{Iso}(r,\phi) &= 1 + \frac{\ln(2\ln 2)}{\ln(r_o/r)} \\
\frac{H_{peak}}{H_{1/2}}_{Adi}(r,\phi) &= \frac{1-\left(\frac{5}{14\ln 2}r/r_o\right)^{2/7}}{1-(r/r_o)^{2/7}}.
\end{aligned} \tag{5.16}$$

For aerial bursts, the impactor radius r must be less than the r_o. Under the assumption $r \ll r_o$, $\frac{H_{peak}}{H_{1/2}}_{Iso}$ and $\frac{H_{peak}}{H_{1/2}}_{Adi}$ go to one. Equation 5.16 therefore shows that the half velocity height is a good first order approximation of the height at which the kinetic energy is most quickly dissipated into the atmosphere for aerial bursts, in agreement with the numerical findings of Shuvalov et al. (2016).

5.4 Application to sub-Neptunes

To illustrate the effects of atmospheric mass-loss by aerial bursts, we apply our model to a theoretical sub-Neptune atmosphere (figure 5.4). We assume atmosphere properties similar to Neptune, with a scale height of 19 km, an atmospheric density of $\rho_o \sim 1000$ kg/m^3 at the base of the envelope, and a planetary core radius of $R = 6000$ km. We consider asteroid-like impactors ($\rho_i = 3300$ kg/m^3) with an initial velocity of $v_\infty = 2v_e$. If the impactor density or initial velocity is greater than these values, mass loss would increase in magnitude at all impactor radii.

Figure 5.4 shows the ejected atmosphere per unit impactor mass as a function of the projectile radius r and the trajectory angle ϕ relative to the vertical z axis. For comparison, we also show the approximated forms of $r_o(\phi)$ (solid curve) and $r_{min}(\phi)$ (dashed curve), as derived in section 5.3.1. Aerial burst-induced mass loss occurs for the radii r where $r_{min} < r < r_o$. At radii larger than r_o, impactors result in mass loss through ground explosions instead of aerial bursts (see section 5.6).

A typical sub-Neptune/Neptune like planet has a large range of radii for which aerial burst-induced mass loss occurs, with most aerial bursts resulting in atmospheric mass loss equal to a few percent of the projectile mass. Because projectiles pass through relatively more atmosphere, and therefore slow to half velocity at higher heights, along horizontal ($\phi = \pi/2$) trajectories than vertical trajectories, there is a much larger range of planetesimal radii that can result in aerial burst-induced mass loss at large trajectory angles than at small angles. Due to the differences in atmospheric mass distribution in adiabatic and isothermal atmosphere profiles, aerial burst mass loss begins at relatively lower radii in the adiabatic model than isothermal model.

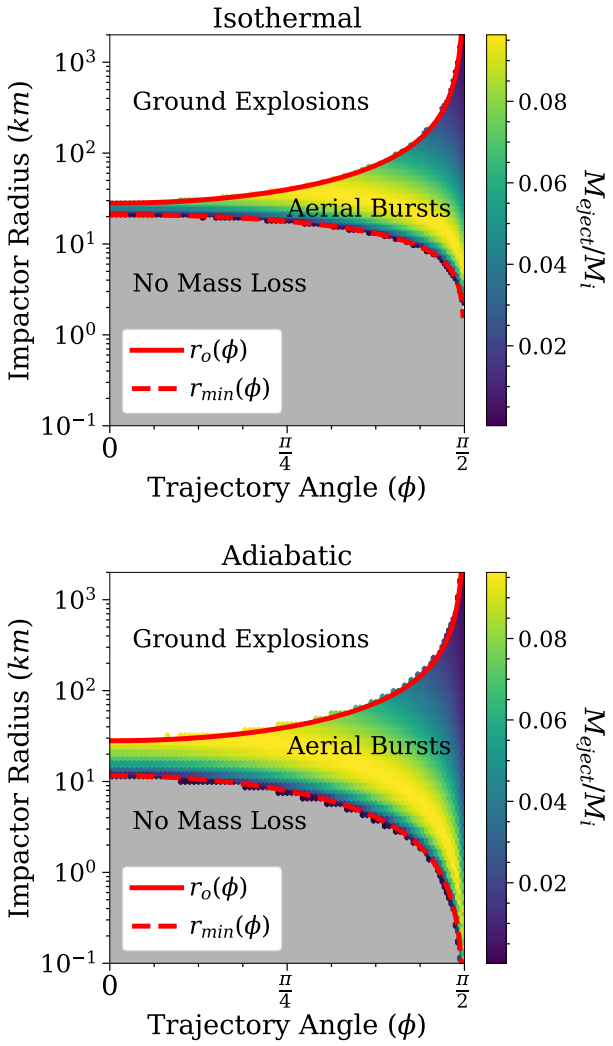

Figure 5.4: Ejected atmospheric mass per impactor mass as a function of the impactor radius and trajectory angle for asteroid-like impactors entering a sub-Neptune/Neptune like atmosphere. The trajectory angle ϕ is measured relative to the vertical z axis (see figure 5.1). The top figure shows mass loss assuming an isothermal atmosphere and the bottom figure shows mass loss for an adiabatic atmosphere. The solid curves show r_o as a function of trajectory angle and the dashed curves show r_{min}. Aerial burst mass loss occurs between r_{min} and r_o. Below r_{min} (below the dashed line) no mass loss can occur. We assume an atmospheric density at the surface of $\rho_o \sim 1000$ kg/m^3 and an impactor density of $\rho_i = 3300$ kg/m^3. Mass loss by aerial bursts can occur at all trajectory angles, and occurs at relatively smaller impactor radii for the adiabatic case than the isothermal case.

5.5 Constraints on the aerial burst Regime

Recall that at a given trajectory angle ϕ, aerial burst-induced mass loss occurs for impactor radii greater than $r_{min}(\phi)$ and less than $r_o(\phi)$. In other words, projectiles must be massive enough to provide adequate energy for mass loss without being so large that they reach the planet surface without decelerating. As shown in section 5.3.1, these radii depend on the atmospheric profile. Therefore, our definitions of r_o and r_{min} can be used to set limits on the properties of atmospheres that may lose mass through aerial bursts. Because aerial burst-induced mass loss occurs for planetesimal radii r where $r_{min} < r < r_o$, for aerial burst mass loss to be possible in an atmosphere with a given atmospheric surface density ρ_o, $r_o(\phi)$ must be greater than $r_{min}(\phi)$ for at least some values of ϕ.

In figure 5.5, we illustrate the range of planetesimal radii that can cause atmospheric-loss by aerial bursts for different atmospheric densities by plotting $r_o(\phi)$ and $r_{min}(\phi)$. In this example, we begin with an earth-like atmosphere, with $\rho_o = 1.22$ kg/m^3 and $h = 8$ km, and show the change in $r_o(\phi)$ as the atmospheric density is increased by consecutive factors of ten. We assume impactor densities of $\rho_i = 3300$ kg/m^3 and initial velocities $v_\infty = 2v_e$.

As calculated in section 5.2.3, the approximated form of the $r_o(\phi)$ curve is equivalent for both the adiabatic and isothermal profiles. $r_o(\phi) \propto \rho_o$, so the upper radius limit of aerial bursts r_o increases with density as bodies must be larger in order to reach the ground before decelerating. $r_{min}(\phi)$ is independent of atmospheric density in the isothermal case, so the minimum radius limit of aerial bursts stays constant with increasing atmospheric density. As the atmospheric density increases, r_o increases, and a larger range of aerial burst radii are able to eject atmospheric mass.

Figure 5.5 shows that for atmospheres with densities close to Earth's current atmospheric density, $r_o < r_{min}$ at all ϕ angles. In other words, only projectiles that reach the planet surface without decelerating will typically provide enough energy to result in atmospheric

mass loss. As a result, for the current earth's atmosphere we find no significant atmospheric loss by aerial bursts.

However, when the atmospheric density is increased by a factor of ten, $r_o > r_{min}$ for trajectories close to the horizontal ($\phi \sim \pi/2$). At this point, some aerial bursts can eject mass if they approach the planet's surface on a nearly horizontal path. Increasing the surface density by a factor of 10^4 allows a range of aerial bursts approaching the planet on any path to eject mass.

While the top panel of figure 5.5 shows the r_{min} curve for an isothermal atmosphere, we note that at high atmospheric densities we expect most atmospheres to be closer to adiabatic than isothermal. The bottom panel of figure 5.5 demonstrates the changes in r_{min} with atmospheric density for an adiabatic profile. As found in section 5.3.1, the r_{min} curve in the adiabatic case depends inversely on density ($r_{min,Adi} \propto \rho_o^{-2/5}$), so it would begin to intersect the r_o curve at lower atmospheric densities than the isothermal r_{min}. This allows for mass loss by aerial bursts at relatively lower atmospheric densities than we found in the isothermal case.

With the knowledge that aerial burst-induced mass loss occurs when $r_o(\phi) \leq r_{min}(\phi)$, we can calculate the minimum surface-level atmospheric density (ρ_o) required to eject mass through aerial bursts at a given trajectory angle (ϕ). Equating the approximated forms of r_o and r_{min} and solving for ρ_o results in

$$\begin{aligned} \frac{\rho_o(\phi)_{min,Iso}}{\rho_i} &= \frac{64}{3}\left(\frac{\ln 2}{\alpha C}\right)^{3/2} \frac{v_e}{v_\infty}\cos(\phi)^{3/2} \\ \frac{\rho_o(\phi)_{min,Adi}}{\rho_i} &= \frac{32\sqrt{2}}{3}\left(\frac{\ln 2}{\alpha C}\right)^{3/2} \frac{v_e}{v_\infty}\cos(\phi)^{3/2}, \end{aligned} \tag{5.17}$$

where $\rho_o(\phi)_{min}$ is the minimum atmospheric density at the planet surface required for mass loss by aerial bursts. Note that the limiting densities have no dependence on the scale height

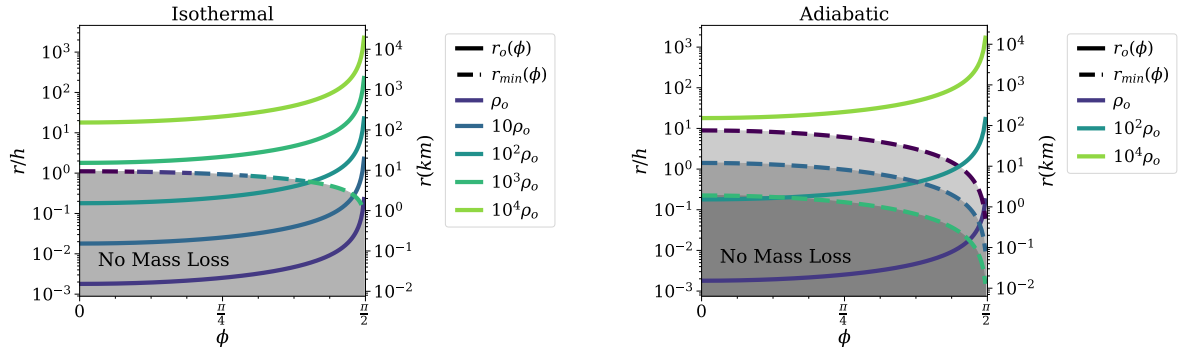

Figure 5.5: Maximum impactor radius that will result in an aerial burst, r_o, as a function of trajectory angle ϕ, for various atmospheric densities (ρ_o). Here $\rho_o = 1.22$ kg/m^3, and we assume an impactor density of $\rho_i = 3300$ kg/m^3 and an initial velocity of $v_\infty/v_e = 2$. The top figure demonstrates the change in characteristic radii for an isothermal profile and the bottom shows the trends for an adiabatic profile. The dashed curves show $r_{min}(\phi)$, the minimum radius needed to eject any mass from a given trajectory angle. Note that r_{min} is independent of atmospheric density in the isothermal case, and varies inversely with density in the adiabatic case. The solid curves show $r_o(\phi)$, the maximum impactor radius that will result in an aerial burst as opposed to a ground explosion. The r_{min} and r_o curves are colored by their corresponding atmospheric density. The regime of mass loss by aerial bursts for a given atmospheric density is found above r_{min} and below $r_o(\rho_o)$. Grey shading shows regions where no mass loss is possible (below r_{min}). Denser atmospheres increase r_o at all trajectory angles, increasing the extent of the aerial burst mass loss regime in both impactor radius and trajectory angle. Because r_{min} in the adiabatic case decreases with increasing atmospheric density, mass loss through aerial bursts can occur at relatively lower densities in the adiabatic atmosphere than in an isothermal atmosphere.

or planet radius in the $h \ll R, \phi \ll \pi/2$ approximation. A weak dependence of the limiting density on scale height and planet radius can be recovered if we evaluate the integral forms of r_o and r_{min} at $\phi = \pi/2$.

Taking the vertical limit as the most conservative indicator of whether aerial burst-induced mass loss is possible, we conclude that consideration of aerial bursts is necessary for atmospheres with densities of $\rho_o/\rho_i \gtrsim 0.4 v_e/v_\infty$.

Figure 5.6 illustrates the minimum densities in equation 5.17 for isothermal and adiabatic atmospheres, assuming $\alpha = 9$, $C = 1$, and $v_\infty = 2v_e$. We also show the approximate ρ_o/ρ_i values for Earth, Venus, and the Neptune/sub-Neptune atmosphere, assuming impactor densities of $\rho_i = 3300$ kg/m^3. As seen in the example in figure 5.5, only denser atmospheres such as that of Venus or Neptune will experience mass loss by aerial bursts for projectiles on more vertical trajectories.

Of particular note are the minimum atmospheric densities at $\phi = \pi/4$, as these trajectories are expected to represent the average collisions angle. We find, to experience mass loss by aerial bursts for impact angles of $\sim \pi/4$, atmospheres must have densities that are at least $\sim 10\%$ of the impactor density.

5.6 Contribution of aerial burst towards total mass loss

At a given trajectory angle, all planetesimals with radii larger than $r_o(\phi)$ (equation 5.13) will not decelerate significantly before reaching the planet surface, and will therefore result in ground explosions. We use the same prescription outlined in section 5.2 to describe ground explosions by simply setting the explosion height (H) in all equations to zero. Because ground explosion impactors do not decelerate significantly in the atmosphere, they will have impact velocities close to their initial velocities ($v_f \sim v_\infty$).

The effects of ground explosions are described in detail in Schlichting et al. (2015); in this

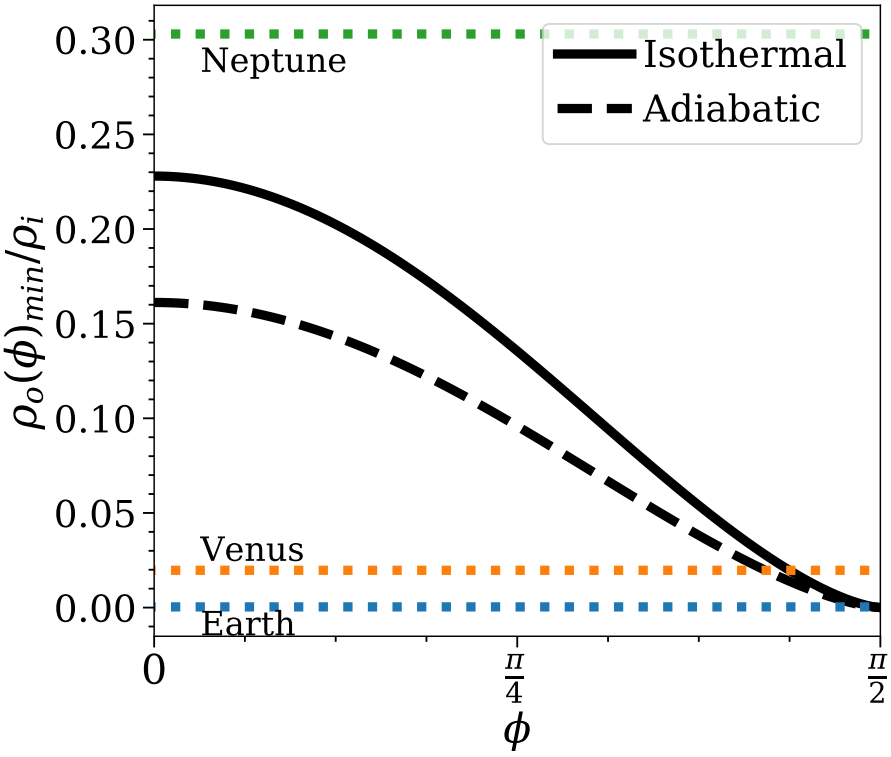

Figure 5.6: Minimum atmospheric density required for the atmosphere to experience mass loss through aerial bursts as a function of trajectory angle, ϕ (equation 5.17). Note, the atmospheric density given on the y-axis is normalized by the impactor density, ρ_i. The solid-black curve represents the isothermal profile, while the dashed-back curve corresponds to the adiabatic profile. Higher atmospheric densities are required for mass to be ejected by aerial bursts in isothermal atmospheres and by projectiles travelling vertically. As reference values, the atmospheric densities for Earth (blue), Venus (yellow) and Neptune (green) are shown as dotted lines.

section we explore how aerial burst-induced mass loss compares to mass loss by ground explosions, and describe the overall differences between the mass loss curves calculated for isothermal versus adiabatic atmospheric density profiles.

5.6.1 Isothermal versus Adiabatic Atmospheres

In figure 5.7 we show the application of both the aerial burst and ground explosion mass loss models to the same sub-Neptunian atmosphere discussed in section 5.4 ($\rho_o = 1000$ kg/m^3, $h = 19$ km), assuming projectiles of density 3300 kg/m^3 with trajectory angles of $\phi = \pi/4$. The curve spans three distinct categories of mass loss: aerial burst-induced mass loss at small impactor radii ($r_{min} < r < r_o$) shaded in yellow, ground explosions at intermediate radii ($r > r_o$) shaded in blue, and a tail at large radii where impactors reach the surface and the impacts are massive enough to eject the full cap of atmosphere above the tangent plane (where $\theta_m = \pi/2$) shaded in red. Note that at radii exceeding ~ 1000 km we may be entering the regime of giant impacts.

As demonstrated in section 5.3.1, figure 5.7 shows that aerial burst-induced mass loss can occur at relatively smaller radii in an adiabatic atmosphere than in an equal mass isothermal atmosphere. This is largely due to the difference in half velocity heights between the two profiles (see figure 5.2), which result in small particles decelerating relatively closer to the ground in adiabatic atmospheres. Because of the dependence on explosion height, the difference between isothermal and adiabatic mass loss is strongest in the aerial burst regime, and we see that projectiles can eject significantly more mass per impactor mass in the adiabatic case than bodies of the same radius in an isothermal atmosphere. Once impactors are large enough to reach the planet surface (the ground explosion regime), the gap between the mass loss curves is significantly reduced, and the two curves converge as we reach the cap ejection regime.

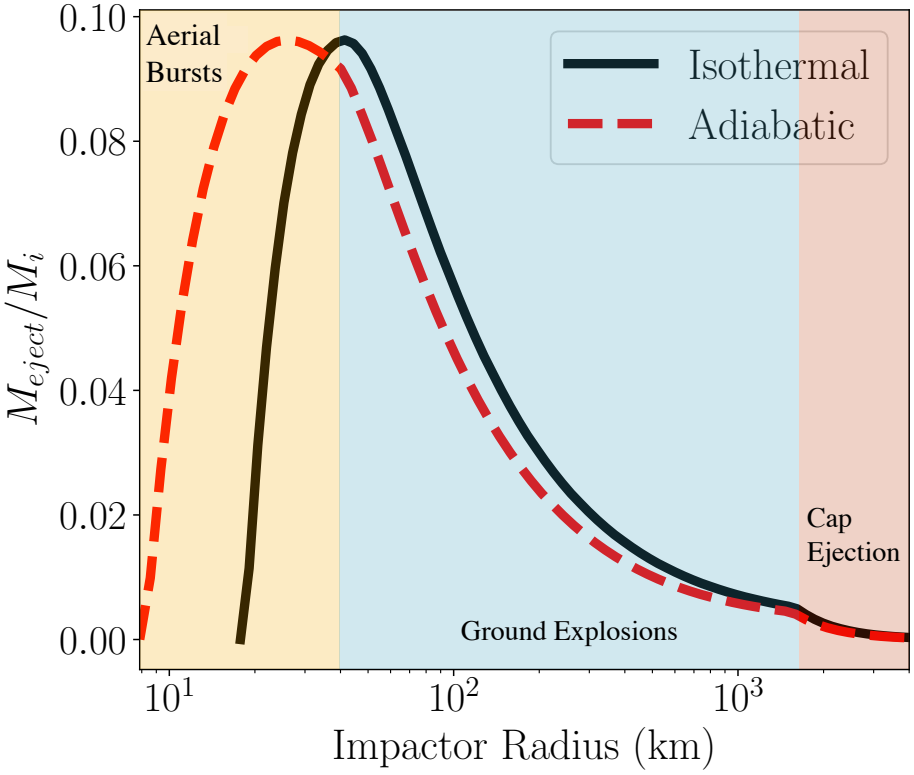

Figure 5.7: Atmospheric mass loss per impactor mass for a sub-Neptune/Neptune like atmosphere ($h = 19$ km, $\rho_o = 1000$ kg/m^3). We assume impactors of density $\rho_i = 3300$ kg/m^3 approaching the planet with trajectory angles of $\phi = \pi/4$. The solid-black curve shows mass loss assuming the atmosphere is isothermal; the dashed-red curve assumes an adiabatic atmospheric profile. Mass loss is separated into three distinct regimes based on the projectile radius: aerial bursts (shaded yellow region), ground explosions (shaded blue region), and ground explosions large enough to eject the full cap of atmosphere above the tangent plane (shaded red region). For sub-Neptune and Neptune-like atmospheres, aerial bursts can contribute significantly to atmospheric mass loss, especially in the adiabatic case and when accounting for the fact that smaller impactors are expected to be far more numerous than larger ones.

5.6.2 Angle-Averaged Mass Loss

Figure 5.8 shows how the atmospheric mass-loss in figure 5.7 changes when the trajectory angle is varied from $\phi = \pi/4$, to $\phi = 0$ and $\phi = \pi/2$. The general shape, progression from aerial burst to ground explosion to cap ejection, and relative difference between the isothermal and adiabatic results remain the same as in the $\phi = \pi/4$ case, with the curve simply extending towards smaller sizes as the trajectory angle increases. As described in section 5.2, this is because projectiles moving horizontally along the tangent plane pass through relatively more atmosphere than those moving vertically, and will therefore decelerate more quickly, broadening the range of impactor radii that result in aerial bursts. This effect can also be seen in section 5.3.1, which shows that r_o, the maximum radius of projectile that results in an aerial bursts, increases with trajectory angle ϕ while r_{min} decreases with ϕ.

In figure 5.9, we show the mass loss expected when we average over all trajectory angles, from $\phi = 0$ to $\phi = \pi/2$, for a sub-Neptune/Neptune-like atmosphere. While the characteristic radii vary with trajectory angle, the peaks in mass loss efficiency for the adiabatic and isothermal curves are both located approximately at the aerial burst/ground explosion transition, similar to figure 5.7. Note that r_{min} only decreases significantly at nearly-horizontal trajectory angles (figure 5.8), so that the range of radii that allow for mass loss is relatively similar at all other angles. As such, in the angle-averaged calculation the distribution of radii that result in the highest overall mass loss efficiencies is relatively narrow, as it is largely dominated by the radii that eject mass in the non-horizontal, $\phi \ll \pi/2$ cases. We therefore see a peak in mass loss efficiency at these radii, accompanied by a tail of low efficiencies corresponding to aerial bursts travelling the closer to the horizontal.

Overall, we find that aerial bursts are able to eject atmosphere with similar maximum efficiencies to ground explosions. These maximum efficiencies are a few to ten percent of atmospheric mass per impactor mass. Because of their smaller size, in a given impact, an aerial bursts will typically eject less mass than a single ground explosion. However, since

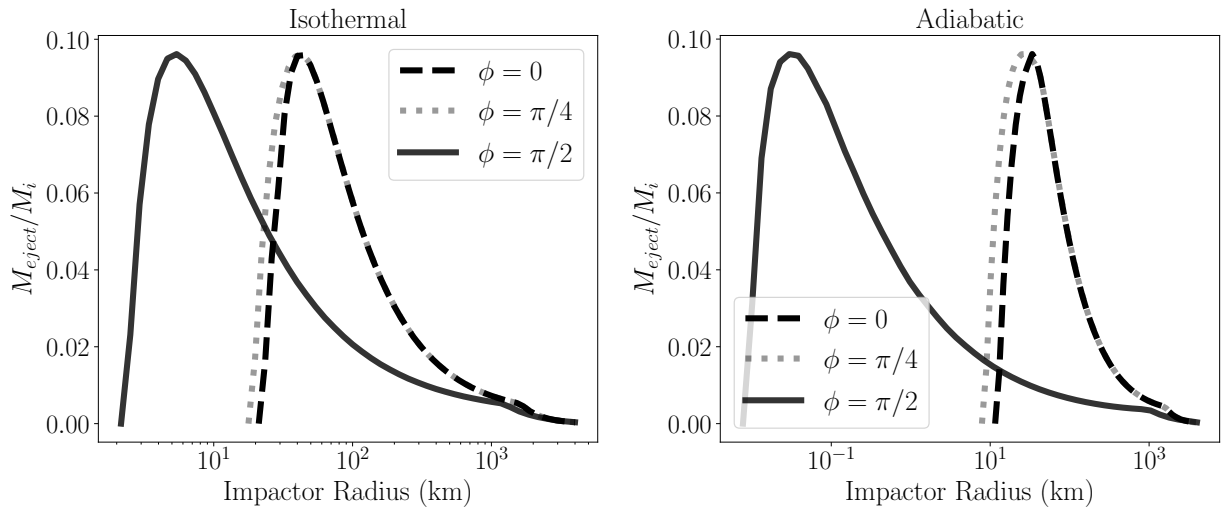

Figure 5.8: Dependence of ejected mass per impactor mass on trajectory angle, ϕ, for $\phi = 0$ (dashed line), $\phi = \pi/4$ (dotted line), and $\phi = \pi/2$ (solid line). We assume an atmosphere profile with $h = 19$ km and $\rho_o = 1000$ kg/m^3, and impactor densities of $\rho_i = 3300$ kg/m^3. Impactors travelling horizontally pass through more atmosphere than those vertically, so they decelerate higher in the atmosphere and result in a larger range of possible impactor radii that can lead to aerial bursts.

smaller bodies are expected to be more numerous, their collective contribution to the overall atmospheric loss likely exceeds that by ground explosions. Assuming an impactor size distribution given by $dN \propto r^{-3.5}dr$ (Dohnanyi, 1969), we find that the more frequent aerial bursts would result in a total atmospheric mass-loss that is larger by a factor of $(r_{\text{ground}}/r_{\text{aerial}})^{0.5}$ compared to ground explosion of similar efficiency.

Therefore, given the cumulative strength of aerial bursts, they should be included in calculations of atmospheric mass-loss for thick atmospheres as defined in section 5.5.

5.7 Discussion and Conclusions

In this work we presented a simple analytical model describing aerial bursts and their associated atmospheric loss. Using this model, we have demonstrated that aerial bursts can lead to significant atmospheric loss for planets with sufficiently dense atmospheres, such as

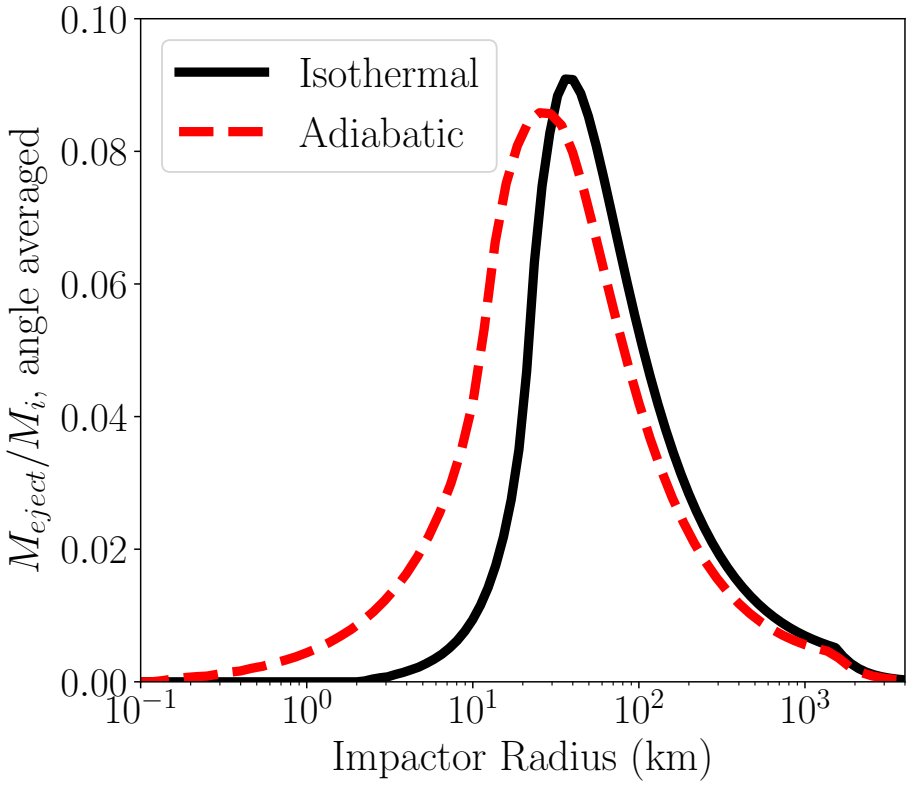

Figure 5.9: Ejected mass per impactor mass averaged over all trajectory angles ($\phi = 0$ to $\pi/2$), for the isothermal and adiabatic profiles. We assume an atmospheric profile with $h = 19$ km and $\rho_o = 1000$ kg/m^3, and impactors of density $\rho_i = 3300$ kg/m^3. The peak in each curve is located at approximately the aerial burst/ground explosion transition, so that mass loss to the left of the peak is largely due to aerial bursts while the right corresponds mainly to ground explosions. The low efficiency tails of both curves at small impactor radii are largely due to the increased range of radii that can eject mass along horizontal trajectories. Meanwhile, the higher efficiency portion of the curve is dominated by the impactor radii corresponding to non-horizontal trajectories.

those expected for sub-Neptunes and Neptune-like planets. For a typical sub-Neptunian atmosphere, we find mass loss efficiencies of up to $\sim 10\%$ of the impactor mass. Specifically, the main conclusions of this paper are as follows:

1. Mass loss from aerial bursts becomes significant when the maximum impactor size that will lead to an aerial burst rather than a ground explosion, r_o, is larger than the minimum impactor size needed to achieve atmospheric loss, r_{min}. For vertical trajectories, which give the most stringent limit, this condition is approximately satisfied when $\rho_o/\rho_i \gtrsim 0.4 v_e/v_\infty$, which implies atmospheric densities need to be comparable to impactor densities for impactor velocities that are a few times the escape velocity of the planet. As a result, aerial bursts are not expected to significantly contribute to the atmospheric mass-loss history of Earth and Earth-like planets, but are expected to play an important role for planets like Neptune with significant atmospheres.

2. The range of impactor radii resulting in aerial burst-induced mass loss, $r_o - r_{min}$, depends on the ratio of the density of the atmosphere to the impactor density, and varies with the trajectory angle, such that the range increases for larger impact angels and larger atmospheric densities.

3. Because adiabatic atmospheres have larger densities for a given height above the ground within in the first scale height compared to isothermal ones, the range of impactor radii that result in aerial burst-induced mass loss is larger in adiabatic atmospheres than isothermal atmospheres of equivalent total mass, scale height, and atmospheric surface density. Similarly, aerial burst impactors of equal size will eject relatively more mass in an adiabatic atmosphere than in the isothermal atmosphere of equivalent total mass and scale height.

4. Increasing the density or initial velocity of impactors will increase the expected mass loss per impactor mass in both the ground explosions and in aerial bursts.

5. The difference between isothermal and adiabatic atmospheric density profiles matters most in the aerial burst-induced mass loss regime. The mass lost per impactor mass is similar for both profiles in the ground explosion regime.

6. For Neptune-like atmospheres, the atmospheric mass ejected per impactor mass by aerial bursts is comparable to that lost by ground explosions. Therefore, for impactors following a Dohnanyi size distribution, overall loss by aerial busts is expected to exceed that by ground explosions by a factor of $(r_{\rm ground}/r_{\rm aerial})^{0.5}$.

In addition to the contributions towards overall atmosphere mass loss discussed thus far, the knowledge that a large number of projectiles will result in aerial bursts as opposed to ground explosions may be important in determining the final compositions of atmospheres.

Because aerial bursts are significantly decelerated high in the atmosphere, they may be useful for depositing volatiles on a planet's surface. In the sub-Neptune atmosphere ($\rho_o \sim 1000$ kg/m^3), we find that impactors with radii up to tens of kilometers could be decelerated before they reach the ground. These objects could therefore reach the surface of the planet without creating a large crater and destroying the majority of the impactor. Hydrodynamical simulations also show that for impactors with the density of asteroids (~ 3300 kg/m^3), little to none of the impactor's own mass will be ejected over the course of its path through the atmosphere (Shuvalov et al. 2014). As such, these aerial bursts could trade small amounts of atmospheric loss for delivery of their own volatiles to the planet.

CHAPTER 6

Conclusions

6.1 Summary

In this dissertation I demonstrate that the exoplanetary material sampled by polluted white dwarfs reflects many of the objects in our own solar system. In Chapter 2, I model the accretion onto white dwarfs to show that white dwarf pollution typically requires parent bodies with masses on par with the largest objects in our asteroid belt or the moons around giant planets. Given the large masses, and motivated by the discovery of beryllium on a white dwarf, I use N-body simulations to show that a few percent of white dwarfs could be accreting moons, a fraction consistent with the fraction of white dwarfs that are most highly polluted. In Chapter 3, I explore compositions more directly by comparing a sample of white dwarfs to different solar system objects, and find that a little over half of white dwarf pollution can be explained by the composition of chondritic material. Furthermore, using elemental abundance measurements for stars, I show that most of the stellar compositions in our local solar neighborhood are consistent with chondrites, the assumed planetary building blocks in our own solar system. In Chapter 4 I calculate oxygen excesses in the element abundances of polluted white dwarfs to show that the majority of highly polluted white dwarfs are accreting water-rich material, with water mass fractions consistent with the icy moons of our solar system. Finally, Chapter 5 contributes towards understanding planet formation in a different way, by analyzing the effects of the accretion of small bodies on atmosphere loss.

6.2 Future Work

The results of this dissertation have inspired three current projects to continue probing exoplanet compositions. First, in Chapter 3's study of stellar abundances as proxies for exo-rock compositions we used the Hypatia Catalog (Hinkel et al., 2014) to collect the compositions of local stars. While the sample from the Hypatia Catalog began to show some variation in abundances due to galactic chemical evolution, the bulk of the stars were still consistent with chondritic composition. This motivates a larger scale study using the much more expansive APOGEE spectroscopic survey (Majewski et al., 2017) to better understand where in the galaxy we should look for planets with drastically different rock compositions. APOGEE provides self-consistently determined element abundances for a massive sample of several hundred thousand stars spanning large swaths of the sky (García Pérez et al., 2016). Stellar population studies have identified many substructures and metallicity trends within the APOGEE data (e.g. Vincenzo et al., 2021; Sit et al., 2024) opening many avenues for testing how core mass fractions, water, and other planetary parameters may shift around the galaxy. In initial tests of the APOGEE data, one of the main challenges in working with this dataset is choosing appropriate abundance uncertainties, a factor that greatly impacts our results. Uncertainties in $[\mathrm{X/H}] = \log(\mathrm{X/H}) - \log(\mathrm{X/H})_\odot$ in the Hypatia catalog were typically around 0.1, determined from the spread in values between different measurements included in the catalog. However, uncertainties reported by APOGEE tend to be closer to 0.05 or lower, and are instead determined by the variation in values between different images of the same star. I am currently collaborating with experts in APOGEE abundances (Jönsson et al., 2018) to determine a path forward with the uncertainty determination. I intend to start by conducting a comparison to chondritic compositions and testing variations in lithophile/siderophile element abundances in main sequence stars in APOGEE overall, with the potential to fold in other composition sources and expand into analyses of specific clusters or other substructures in future works.

One of the important diagnostic parameters of rocky material is oxidation state, which encodes information about where the rock formed (more reduced material is typically attributed to the inner solar system, while more oxidized bodies originate in the outer solar system) and influences the structure, composition, and atmosphere of the planet (e.g. Ehlmann et al., 2016; Wordsworth et al., 2018). Doyle et al. (2019) measured oxidation states of WDs by calculating oxygen fugacities based on oxygen excesses in the observed elemental abundances. However, another way to assess oxidation states is through the relative evaporation rates of Mn and Na. Mn and Na have very similar condensation temperatures of 1158 K and 958 K, respectively (Lodders, 2003), meaning they should begin to evaporate around the same time. However, the volatilities of the two species vary differently as a function of oxygen fugacity so that the relative evaporation of Na to Mn goes as $\frac{\delta_{\mathrm{Na}}}{\delta_{\mathrm{Mn}}} \propto \mathrm{P}_{\mathrm{O}_2}^{\frac{1}{4}}$, where δ is the change in abundance of each species relative to the initial value and P_{O_2} is the partial pressure of O. Because we showed in Chapters 3 and 4 that most WD pollution is chondritic in composition, we can therefore use polluted WDs with Mn and Na abundances to calculate oxygen fugacities on the assumption that the original material was chondritic. I first tested this method by calculating oxygen fugacities for solar system objects based on Mn and Na abundances, including Earth, Mars, and several meteorites. I find that these bodies typically fall along two curves, with Earth and most meteorites having a relatively lower oxygen fugacity than Mars. This is consistent with Earth and the sampled meteorites forming in the more reduced inner solar system, while Mars received some material from the outer disk. While we expect fairly broad uncertainties in the inferred WD oxygen fugacities, applying the Mn/Na model to the WDs will help provide another constraint on where the polluting material originates.

Finally, Chapter 5 discussed how small accreting bodies can facilitate atmosphere loss on planets. One of the implications of the model is that small bodies can be an effective means of removing atmosphere and depositing material on a planet. A collaboration led by Dr. Haolan Tang is now integrating the atmosphere mass loss model with a larger model of pebble accretion to test whether the oxidation and isotopic compositions on planetary

embryos can be significantly impacted by the process of pebble accretion. The model includes atmosphere/magma ocean interactions and tracks water, Fe, Mg, Si, and K. As pebbles enter the atmosphere of a planetesimal they evaporate to create water and deposit Mg, SiO, and K into the atmosphere. The pebble will preferentially lose lighter isotopes, potentially creating an isotopic differences between the Mg and Si in the atmosphere as compared to the heavier remnants that reach the magma ocean. Furthermore, water in the atmosphere will then enter the magma ocean, oxidizing Fe in the core to make FeO and raise the oxidation state of the embryo. This study is important because it would indicate whether bodies in relatively reduced environments (like the inner disk of the solar system) can reach the oxidation states we observe today as a natural side effect of planet formation, or require significant input of material from outer solar system in order to explain their compositions.

Bibliography

Abe, Y., & Matsui, T. 1985, Lunar and Planetary Science Conference Proceedings, 90, C545

Adibekyan, V., Dorn, C., Sousa, S. G., et al. 2021, Science, 374, 330, doi: 10.1126/science.abg8794

Anders, E., & Grevesse, N. 1989, Geochimica Cosmochimica Acta, 53, 197, doi: 10.1016/0016-7037(89)90286-X

Andrae, R., Schulze-Hartung, T., & Melchior, P. 2010, arXiv preprint arXiv:1012.3754

Barlow, R. 2003, arXiv e-prints, physics/0306138, doi: 10.48550/arXiv.physics/0306138

Bauer, E. B., & Bildsten, L. 2019, Astrophysical Journal, 872, 96, doi: 10.3847/1538-4357/ab0028

Bellardini, M. A., Wetzel, A., Loebman, S. R., & Bailin, J. 2022, Monthly Notices of the RAS, 514, 4270, doi: 10.1093/MonthlyNoticesoftheRAS/stac1637

Blouin, S., Dufour, P., & Allard, N. F. 2018, Astrophysical Journal, 863, 184, doi: 10.3847/1538-4357/aad4a9

Boldog, Á., Dobos, V., Kiss, L. L., van der Perk, M., & Barr, A. C. 2024, Astronomy and Astrophysics, 681, A109, doi: 10.1051/0004-6361/202346988

Bond, J. C., O'Brien, D. P., & Lauretta, D. S. 2010, Astrophysical Journal, 715, 1050, doi: 10.1088/0004-637X/715/2/1050

Bonsor, A., Jofré, P., Shorttle, O., et al. 2021, Monthly Notices of the RAS, 503, 1877, doi: 10.1093/MonthlyNoticesoftheRAS/stab370

Boslough, M. B., Crawford, D. A., Trucano, T. G., & Robinson, A. C. 1995, Geophysics Research Letters, 22, 1821, doi: 10.1029/95GL01749

Brouwers, M. G., Bonsor, A., & Malamud, U. 2023, Monthly Notices of the RAS, 519, 2646, doi: 10.1093/MonthlyNoticesoftheRAS/stac3316

Cameron, A. G. W., & Ward, W. R. 1976, in Lunar and Planetary Science Conference, Vol. 7, Lunar and Planetary Science Conference, 120

Canup, R. M., & Asphaug, E. 2001, Nature, 412, 708

Cayrel, R., Hill, V., Beers, T. C., et al. 2001, Nature, 409, 691, doi: 10.1038/35055507

Chakrabarty, A., & Mulders, G. D. 2024, Astrophysical Journal, 966, 185, doi: 10.3847/1538-4357/ad3802

Chyba, C. F. 1990, Nature, 343, 129, doi: 10.1038/343129a0

Coutu, S., Dufour, P., Bergeron, P., et al. 2019, Astrophysical Journal, 885, 74, doi: 10.3847/1538-4357/ab46b9

Cowan, J. J., Sneden, C., Burles, S., et al. 2002, Astrophysical Journal, 572, 861, doi: 10.1086/340347

Craddock, R. A., & Greeley, R. 2009, Icarus, 204, 512, doi: 10.1016/j.icarus.2009.07.026

Cross, W., Iddings, J. P., Pirsson, L. V., & Washington, H. S. 1902, The Journal of Geology, 10, 555, doi: 10.1086/621030

Cummings, J. D., Kalirai, J. S., Tremblay, P. E., Ramirez-Ruiz, E., & Choi, J. 2018, Astrophysical Journal, 866, 21, doi: 10.3847/1538-4357/aadfd6

Cunningham, T., Tremblay, P.-E., Freytag, B., Ludwig, H.-G., & Koester, D. 2019, Monthly Notices of the RAS, 488, 2503, doi: 10.1093/MonthlyNoticesoftheRAS/stz1759

Dauphas, N. 2003, Icarus, 165, 326, doi: 10.1016/S0019-1035(03)00198-2

—. 2017, Nature, 541, 521, doi: 10.1038/nature20830

de Sanctis, M. C., Ammannito, E., Raponi, A., et al. 2015, Nature, 528, 241, doi: 10.1038/nature16172

Dean, R. B., & Dixon, W. J. 1951, Analytical Chemistry, 23, 636, doi: 10.1021/ac60052a025

Debes, J. H., & Sigurdsson, S. 2002, Astrophysical Journal, 572, 556, doi: 10.1086/340291

Desharnais, S., Wesemael, F., Chayer, P., Kruk, J. W., & Saffer, R. A. 2008, Astrophysical Journal, 672, 540, doi: 10.1086/523699

Dobos, V., Charnoz, S., Pál, A., Roque-Bernard, A., & Szabó, G. M. 2021, Publications of the ASP, 133, 094401, doi: 10.1088/1538-3873/abfe04

Dohnanyi, J. S. 1969, Journal of Geophysics Research, 74, 2531, doi: 10.1029/JB074i010p02531

Donor, J., Frinchaboy, P. M., Cunha, K., et al. 2020, Astronomical Journal, 159, 199, doi: 10.3847/1538-3881/ab77bc

Dorn, C., Harrison, J. H. D., Bonsor, A., & Hands, T. O. 2019, Monthly Notices of the RAS, 484, 712, doi: 10.1093/MonthlyNoticesoftheRAS/sty3435

Dorn, C., Khan, A., Heng, K., et al. 2015, Astronomy and Astrophysics, 577, A83, doi: 10.1051/0004-6361/201424915

Dorn, C., & Lichtenberg, T. 2021, Astrophysical Journal, Letters, 922, L4, doi: 10.3847/2041-8213/ac33af

Doyle, A. E., Desch, S. J., & Young, E. D. 2021, Astrophysical Journal, Letters, 907, L35, doi: 10.3847/2041-8213/abd9ba

Doyle, A. E., Klein, B., Schlichting, H. E., & Young, E. D. 2020, Astrophysical Journal, 901, 10, doi: 10.3847/1538-4357/abad9a

Doyle, A. E., Young, E. D., Klein, B., Zuckerman, B., & Schlichting, H. E. 2019, Science, 366, 356, doi: 10.1126/science.aax3901

Doyle, A. E., Klein, B. L., Dufour, P., et al. 2023, Astrophysical Journal, 950, 93, doi: 10.3847/1538-4357/acbd44

Drake, M. J., & Righter, K. 2002, Nature, 416, 39, doi: 10.1038/416039a

Dufour, P., Blouin, S., Coutu, S., et al. 2017, in Astronomical Society of the Pacific Conference Series, Vol. 509, 20th European White Dwarf Workshop, ed. P. E. Tremblay, B. Gaensicke, & T. Marsh, 3. https://arxiv.org/abs/1610.00986

Dufour, P., Kilic, M., Fontaine, G., et al. 2012, Astrophysical Journal, 749, 6, doi: 10.1088/0004-637X/749/1/6

Ehlmann, B. L., Anderson, F. S., Andrews-Hanna, J., et al. 2016, Journal of Geophysical Research (Planets), 121, 1927, doi: 10.1002/2016JE005134

El-Badry, K., Rix, H.-W., & Weisz, D. R. 2018, Astrophysical Journal, Letters, 860, L17, doi: 10.3847/2041-8213/aaca9c

Elkins-Tanton, L. T. 2012, Annual Review of Earth and Planetary Sciences, 40, 113, doi: 10.1146/annurev-earth-042711-105503

Farihi, J., Gänsicke, B. T., & Koester, D. 2013, Science, 342, 218, doi: 10.1126/science.1239447

Farihi, J., Koester, D., Zuckerman, B., et al. 2016, Monthly Notices of the RAS, 463, 3186, doi: 10.1093/MonthlyNoticesoftheRAS/stw2182

Foreman-Mackey, D., Hogg, D. W., Lang, D., & Goodman, J. 2013, Publications of the ASP, 125, 306, doi: 10.1086/670067

Fortin-Archambault, M., Dufour, P., & Xu, S. 2020a, Astrophysical Journal, 888, 47, doi: 10.3847/1538-4357/ab585a

—. 2020b, Astrophysical Journal, 888, 47, doi: 10.3847/1538-4357/ab585a

Gänsicke, B. T., Koester, D., Farihi, J., et al. 2012, Monthly Notices of the RAS, 424, 333, doi: 10.1111/j.1365-2966.2012.21201.x

Gänsicke, B. T., Schreiber, M. R., Toloza, O., et al. 2019, Nature, 576, 61, doi: 10.1038/s41586-019-1789-8

García Pérez, A. E., Allende Prieto, C., Holtzman, J. A., et al. 2016, Astronomical Journal, 151, 144, doi: 10.3847/0004-6256/151/6/144

Genda, H., & Abe, Y. 2003, Icarus, 164, 149, doi: 10.1016/S0019-1035(03)00101-5

Gentile Fusillo, N. P., Gänsicke, B. T., Farihi, J., et al. 2017, Monthly Notices of the RAS, 468, 971, doi: 10.1093/MonthlyNoticesoftheRAS/stx468

Ginzburg, S., Schlichting, H. E., & Sari, R. 2016, Astrophysical Journal, 825, 29, doi: 10.3847/0004-637X/825/1/29

—. 2018, Monthly Notices of the RAS, 476, 759, doi: 10.1093/mnras/sty290

Giorgini, J. D., Yeomans, D. K., Chamberlin, A. B., et al. 1996, in AAS/Division for Planetary Sciences Meeting Abstracts, Vol. 28, AAS/Division for Planetary Sciences Meeting Abstracts #28, 25.04

Girven, J., Brinkworth, C. S., Farihi, J., et al. 2012, Astrophysical Journal, 749, 154, doi: 10.1088/0004-637X/749/2/154

Goździewski, K., & Migaszewski, C. 2020, Astrophysical Journal, Letters, 902, L40, doi: 10.3847/2041-8213/abb881

Gupta, A., & Schlichting, H. E. 2019, Monthly Notices of the RAS, 487, 24, doi: 10.1093/MonthlyNoticesoftheRAS/stz1230

Harrison, J. H. D., Bonsor, A., & Madhusudhan, N. 2018, Monthly Notices of the RAS, 479, 3814, doi: 10.1093/MonthlyNoticesoftheRAS/sty1700

Hayden, M. R., Holtzman, J. A., Bovy, J., et al. 2014, Astronomical Journal, 147, 116, doi: 10.1088/0004-6256/147/5/116

Hayden, M. R., Bovy, J., Holtzman, J. A., et al. 2015, Astrophysical Journal, 808, 132, doi: 10.1088/0004-637X/808/2/132

Hill, V., Plez, B., Cayrel, R., et al. 2002, Astronomy and Astrophysics, 387, 560, doi: 10.1051/0004-6361:20020434

Hills, J. G., & Goda, M. P. 1993, Astronomical Journal, 105, 1114, doi: 10.1086/116499

Hinkel, N. R., Timmes, F. X., Young, P. A., Pagano, M. D., & Turnbull, M. C. 2014, Astronomical Journal, 148, 54, doi: 10.1088/0004-6256/148/3/54

Hinkel, N. R., & Unterborn, C. T. 2018, Astrophysical Journal, 853, 83, doi: 10.3847/1538-4357/aaa5b4

Hollands, M. A., Gänsicke, B. T., & Koester, D. 2018, Monthly Notices of the RAS, 477, 93, doi: 10.1093/MonthlyNoticesoftheRAS/sty592

Hollands, M. A., Koester, D., Alekseev, V., Herbert, E. L., & Gänsicke, B. T. 2017, Monthly Notices of the RAS, 467, 4970, doi: 10.1093/MonthlyNoticesoftheRAS/stx250

Hollands, M. A., Tremblay, P. E., Gänsicke, B. T., & Koester, D. 2022, Monthly Notices of the RAS, 511, 71, doi: 10.1093/MonthlyNoticesoftheRAS/stab3696

Horta, D., Schiavon, R. P., Mackereth, J. T., et al. 2022, Monthly Notices of the RAS, doi: 10.1093/MonthlyNoticesoftheRAS/stac3179

Hoskin, M. J., Toloza, O., Gänsicke, B. T., et al. 2020, Monthly Notices of the RAS, 499, 171, doi: 10.1093/MonthlyNoticesoftheRAS/staa2717

Hurley, J. R., Pols, O. R., & Tout, C. A. 2000, Monthly Notices of the RAS, 315, 543, doi: 10.1046/j.1365-8711.2000.03426.x

Izquierdo, P., Gänsicke, B. T., Rodríguez-Gil, P., et al. 2023, Monthly Notices of the RAS, 520, 2843, doi: 10.1093/MonthlyNoticesoftheRAS/stad282

Izquierdo, P., Toloza, O., Gänsicke, B. T., et al. 2021, Monthly Notices of the RAS, 501, 4276, doi: 10.1093/MonthlyNoticesoftheRAS/staa3987

Jönsson, H., Allende Prieto, C., Holtzman, J. A., et al. 2018, Astronomical Journal, 156, 126, doi: 10.3847/1538-3881/aad4f5

Jura, M. 2003, Astrophysical Journal, Letters, 584, L91, doi: 10.1086/374036

Jura, M., Muno, M. P., Farihi, J., & Zuckerman, B. 2009, Astrophysical Journal, 699, 1473, doi: 10.1088/0004-637X/699/2/1473

Jura, M., & Xu, S. 2010, Astronomical Journal, 140, 1129, doi: 10.1088/0004-6256/140/5/1129

—. 2012, Astronomical Journal, 143, 6, doi: 10.1088/0004-6256/143/1/6

Jura, M., Xu, S., Klein, B., Koester, D., & Zuckerman, B. 2012, Astrophysical Journal, 750, 69, doi: 10.1088/0004-637X/750/1/69

Jura, M., & Young, E. D. 2014, Annual Review of Earth and Planetary Sciences, 42, 45, doi: 10.1146/annurev-earth-060313-054740

Kempton, E. M. R., Lessard, M., Malik, M., et al. 2023, Astrophysical Journal, 953, 57, doi: 10.3847/1538-4357/ace10d

Kipping, D. 2021, Monthly Notices of the RAS, 507, 4120, doi: 10.1093/MonthlyNoticesoftheRAS/stab2013

Klein, B., Jura, M., Koester, D., & Zuckerman, B. 2011, Astrophysical Journal, 741, 64, doi: 10.1088/0004-637X/741/1/64

Klein, B., Jura, M., Koester, D., Zuckerman, B., & Melis, C. 2010, Astrophysical Journal, 709, 950, doi: 10.1088/0004-637X/709/2/950

Klein, B. L., Doyle, A. E., Zuckerman, B., et al. 2021, Astrophysical Journal, 914, 61, doi: 10.3847/1538-4357/abe40b

Kobayashi, C., Karakas, A. I., & Lugaro, M. 2020, Astrophysical Journal, 900, 179, doi: 10.3847/1538-4357/abae65

Kobayashi, C., & Nakasato, N. 2011, Astrophysical Journal, 729, 16, doi: 10.1088/0004-637X/729/1/16

Koester, D. 2009, Astronomy and Astrophysics, 498, 517, doi: 10.1051/0004-6361/200811468

Koester, D., Gänsicke, B. T., & Farihi, J. 2014, Astronomy and Astrophysics, 566, A34, doi: 10.1051/0004-6361/201423691

Koester, D., Kepler, S. O., & Irwin, A. W. 2020, Astronomy and Astrophysics, 635, A103, doi: 10.1051/0004-6361/202037530

Koester, D., Rollenhagen, K., Napiwotzki, R., et al. 2005, Astronomy and Astrophysics, 432, 1025, doi: 10.1051/0004-6361:20041927

Kulikov, Y. N., Lammer, H., Lichtenegger, H. I. M., et al. 2007, Space Science Reviews, 129, 207, doi: 10.1007/s11214-007-9192-4

Lammer, H., Stökl, A., Erkaev, N. V., et al. 2014, Monthly Notices of the RAS, 439, 3225, doi: 10.1093/MonthlyNoticesoftheRAS/stu085

Lodders, K. 2003, Astrophysical Journal, 591, 1220, doi: 10.1086/375492

—. 2019, arXiv e-prints, arXiv:1912.00844, doi: 10.48550/arXiv.1912.00844

—. 2021, Space Science Reviews, 217, 44, doi: 10.1007/s11214-021-00825-8

Lodders, K., Palme, H., & Gail, H. P. 2009, Landolt Börnstein, 4B, 712, doi: 10.1007/978-3-540-88055-4_34

Madhusudhan, N., Lee, K. K. M., & Mousis, O. 2012, Astrophysical Journal, Letters, 759, L40, doi: 10.1088/2041-8205/759/2/L40

Majewski, S. R., Schiavon, R. P., Frinchaboy, P. M., et al. 2017, Astronomical Journal, 154, 94, doi: 10.3847/1538-3881/aa784d

Malamud, U., & Perets, H. B. 2016, Astrophysical Journal, 832, 160, doi: 10.3847/0004-637X/832/2/160

—. 2017, Astrophysical Journal, 849, 8, doi: 10.3847/1538-4357/aa8df5

Maldonado, R. F., Villaver, E., Mustill, A. J., & Chávez, M. 2022, Monthly Notices of the RAS, 512, 104, doi: 10.1093/MonthlyNoticesoftheRAS/stac481

Manser, C. J., Gänsicke, B. T., Koester, D., Marsh, T. R., & Southworth, J. 2016, Monthly Notices of the RAS, 462, 1461, doi: 10.1093/MonthlyNoticesoftheRAS/stw1760

Marois, C., Macintosh, B., Barman, T., et al. 2008, Science, 322, 1348, doi: 10.1126/science.1166585

Marois, C., Zuckerman, B., Konopacky, Q. M., Macintosh, B., & Barman, T. 2010, Nature, 468, 1080, doi: 10.1038/nature09684

McDonough, W. F. 2003, Treatise on Geochemistry, 2, 568, doi: 10.1016/B0-08-043751-6/02015-6

Melis, C. 2016, in Young Stars & Planets Near the Sun, ed. J. H. Kastner, B. Stelzer, & S. A. Metchev, Vol. 314, 241–246, doi: 10.1017/S1743921315006638

Melis, C., & Dufour, P. 2017, Astrophysical Journal, 834, 1, doi: 10.3847/1538-4357/834/1/1

Melis, C., Farihi, J., Dufour, P., et al. 2011, Astrophysical Journal, 732, 90, doi: 10.1088/0004-637X/732/2/90

Melosh, H. J., & Vickery, A. M. 1989, Nature, 338, 487, doi: 10.1038/338487a0

Michel, A., Haldemann, J., Mordasini, C., & Alibert, Y. 2020, Astronomy and Astrophysics, 639, A66, doi: 10.1051/0004-6361/201936916

Monson, N. N., Morris, M. R., & Young, E. D. 2017, Astrophysical Journal, 839, 123, doi: 10.3847/1538-4357/aa67e6

Mustill, A. J., Villaver, E., Veras, D., Gänsicke, B. T., & Bonsor, A. 2018, Monthly Notices of the RAS, 476, 3939, doi: 10.1093/MonthlyNoticesoftheRAS/sty446

Newman, W. I., Symbalisty, E. M. D., Ahrens, T. J., & Jones, E. M. 1999, Icarus, 138, 224, doi: 10.1006/icar.1999.6076

Nielsen, E. L., De Rosa, R. J., Macintosh, B., et al. 2019, Astronomical Journal, 158, 13, doi: 10.3847/1538-3881/ab16e9

O'Connor, C. E., Teyssandier, J., & Lai, D. 2022, Monthly Notices of the RAS, 513, 4178, doi: 10.1093/MonthlyNoticesoftheRAS/stac1189

Owen, J. E., & Wu, Y. 2013, Astrophysical Journal, 775, 105, doi: 10.1088/0004-637X/775/2/105

Owen, T., & Bar-Nun, A. 1995, Icarus, 116, 215, doi: 10.1006/icar.1995.1122

Payne, M. J., Veras, D., Gänsicke, B. T., & Holman, M. J. 2017, Monthly Notices of the RAS, 464, 2557, doi: 10.1093/MonthlyNoticesoftheRAS/stw2585

Payne, M. J., Veras, D., Holman, M. J., & Gänsicke, B. T. 2016, Monthly Notices of the RAS, 457, 217, doi: 10.1093/MonthlyNoticesoftheRAS/stv2966

Piette, A. A. A., Gao, P., Brugman, K., et al. 2023, Astrophysical Journal, 954, 29, doi: 10.3847/1538-4357/acdef2

Pu, B., & Wu, Y. 2015, Astrophysical Journal, 807, 44, doi: 10.1088/0004-637X/807/1/44

Putirka, K. D., & Rarick, J. C. 2019, American Mineralogist, 104, 817, doi: 10.2138/am-2019-6787

Putirka, K. D., & Xu, S. 2021, Nature Communications, 12, 6168, doi: 10.1038/s41467-021-26403-8

Raddi, R., Gänsicke, B. T., Koester, D., et al. 2015, Monthly Notices of the RAS, 450, 2083, doi: 10.1093/MonthlyNoticesoftheRAS/stv701

Rein, H., & Liu, S. F. 2012, Astronomy and Astrophysics, 537, A128, doi: 10.1051/0004-6361/201118085

Rein, H., & Spiegel, D. S. 2015, Monthly Notices of the RAS, 446, 1424, doi: 10.1093/MonthlyNoticesoftheRAS/stu2164

Reynard, B., & Sotin, C. 2023, Earth and Planetary Science Letters, 612, 118172, doi: 10.1016/j.epsl.2023.118172

Rogers, J. G., & Owen, J. E. 2021, Monthly Notices of the RAS, 503, 1526, doi: 10.1093/MonthlyNoticesoftheRAS/stab529

Rudnick, R. L., & Gao, S. 2003, Treatise on Geochemistry, 3, 659, doi: 10.1016/B0-08-043751-6/03016-4

Santos, N. C., Adibekyan, V., Mordasini, C., et al. 2015, Astronomy and Astrophysics, 580, L13, doi: 10.1051/0004-6361/201526850

Schaller, G., Schaerer, D., Meynet, G., & Maeder, A. 1992, Astronomy and Astrophysics Supplement, 96, 269

Schlichting, H. E., Sari, R., & Yalinewich, A. 2015, Icarus, 247, 81, doi: 10.1016/j.icarus.2014.09.053

Schlichting, H. E., & Young, E. D. 2022, Planetary Science Journal, 3, 127, doi: 10.3847/PlanetaryScienceJournal/ac68e6

Schulze, J. G., Wang, J., Johnson, J. A., et al. 2021, Planetary Science Journal, 2, 113, doi: 10.3847/PlanetaryScienceJournal/abcaa8

Shuvalov, V. 2009, Meteoritics & Planetary Science, 44, 1095, doi: 10.1111/j.1945-5100.2009.tb01209.x

Shuvalov, V., Kührt, E., de Niem, D., & Wünnemann, K. 2014, Planetary Space Science, 98, 120, doi: 10.1016/j.pss.2013.08.018

Shuvalov, V. V., Popova, O. P., Svettsov, V. V., Trubetskaya, I. A., & Glazachev, D. O. 2016, Solar System Research, 50, 1, doi: 10.1134/S0038094616010056

Sinclair, C. A., Wyatt, M. C., Morbidelli, A., & Nesvorný, D. 2020, Monthly Notices of the RAS, 499, 5334, doi: 10.1093/MonthlyNoticesoftheRAS/staa3210

Sit, T., Weinberg, D. H., Wheeler, A., et al. 2024, arXiv e-prints, arXiv:2403.08067, doi: 10.48550/arXiv.2403.08067

Stephan, A. P., Naoz, S., & Zuckerman, B. 2017, Astrophysical Journal, Letters, 844, L16, doi: 10.3847/2041-8213/aa7cf3

Swan, A., Farihi, J., Koester, D., et al. 2019, Monthly Notices of the RAS, 490, 202, doi: 10.1093/MonthlyNoticesoftheRAS/stz2337

Swan, A., Farihi, J., Melis, C., et al. 2023, Monthly Notices of the RAS, 526, 3815, doi: 10.1093/MonthlyNoticesoftheRAS/stad2867

Taylor, G. J. 2013, Chemie der Erde / Geochemistry, 73, 401, doi: 10.1016/j.chemer.2013.09.006

Teachey, A., & Kipping, D. 2021, Monthly Notices of the RAS, 508, 2620, doi: 10.1093/MonthlyNoticesoftheRAS/stab2694

Thiabaud, A., Marboeuf, U., Alibert, Y., Leya, I., & Mezger, K. 2015, Astronomy and Astrophysics, 580, A30, doi: 10.1051/0004-6361/201525963

Timmes, F. X., Woosley, S. E., & Weaver, T. A. 1995, Astrophysical Journal, Supplement, 98, 617, doi: 10.1086/192172

Trierweiler, I. L., Doyle, A. E., Melis, C., Walsh, K. J., & Young, E. D. 2022, Astrophysical Journal, 936, 30, doi: 10.3847/1538-4357/ac86d5

Trierweiler, I. L., Doyle, A. E., & Young, E. D. 2023, Planetary Science Journal, 4, 136, doi: 10.3847/PlanetaryScienceJournal/acdef3

Trierweiler, I. L., & Schlichting, H. E. 2022, Monthly Notices of the RAS, 514, 3650, doi: 10.1093/MonthlyNoticesoftheRAS/stac1509

Unterborn, C. T., Desch, S. J., Hinkel, N. R., & Lorenzo, A. 2018, Nature Astronomy, 2, 297, doi: 10.1038/s41550-018-0411-6

Vanderburg, A., Johnson, J. A., Rappaport, S., et al. 2015, Nature, 526, 546, doi: 10.1038/nature15527

Veras, D., & Gänsicke, B. T. 2015, Monthly Notices of the RAS, 447, 1049, doi: 10.1093/MonthlyNoticesoftheRAS/stu2475

Veras, D., & Hinkley, S. 2021, Monthly Notices of the RAS, 505, 1557, doi: 10.1093/MonthlyNoticesoftheRAS/stab1311

Veras, D., Mustill, A. J., Gänsicke, B. T., et al. 2016, Monthly Notices of the RAS, 458, 3942, doi: 10.1093/MonthlyNoticesoftheRAS/stw476

Veras, D., & Rosengren, A. J. 2023, Monthly Notices of the RAS, 519, 6257, doi: 10.1093/MonthlyNoticesoftheRAS/stad130

Vickery, A. M., & Melosh, H. J. 1990, in Global Catastrophes in Earth History; An Interdisciplinary Conference on Impacts, Volcanism, and Mass Mortality (Geological Society of America), doi: 10.1130/SPE247-p289

Vincenzo, F., Weinberg, D. H., Miglio, A., Lane, R. R., & Roman-Lopes, A. 2021, Monthly Notices of the RAS, 508, 5903, doi: 10.1093/MonthlyNoticesoftheRAS/stab2899

Walker, R. J. 2009, Chemie der Erde / Geochemistry, 69, 101, doi: 10.1016/j.chemer.2008.10.001

Walker, R. J., Horan, M. F., Shearer, C. K., & Papike, J. J. 2004, Earth and Planetary Science Letters, 224, 399, doi: 10.1016/j.epsl.2004.05.036

Warren, P. H., Kallemeyn, G. W., & Kyte, F. T. 1999, Geochimica Cosmochimica Acta, 63, 2105, doi: 10.1016/S0016-7037(99)00156-8

Wasson, J. T., & Kallemeyn, G. W. 1988, Philosophical Transactions of the Royal Society of London Series A, 325, 535, doi: 10.1098/rsta.1988.0066

Weiss, L. M., Marcy, G. W., Petigura, E. A., et al. 2018, Astronomical Journal, 155, 48, doi: 10.3847/1538-3881/aa9ff6

Wilson, D. J., Gänsicke, B. T., Koester, D., et al. 2015, Monthly Notices of the RAS, 451, 3237, doi: 10.1093/MonthlyNoticesoftheRAS/stv1201

Wordsworth, R. D., Schaefer, L. K., & Fischer, R. A. 2018, Astronomical Journal, 155, 195, doi: 10.3847/1538-3881/aab608

Wyatt, M. C., Kral, Q., & Sinclair, C. A. 2020, Monthly Notices of the RAS, 491, 782, doi: 10.1093/MonthlyNoticesoftheRAS/stz3052

Xu, S., Dufour, P., Klein, B., et al. 2019, Astronomical Journal, 158, 242, doi: 10.3847/1538-3881/ab4cee

Xu, S., Jura, M., Klein, B., Koester, D., & Zuckerman, B. 2013, Astrophysical Journal, 766, 132, doi: 10.1088/0004-637X/766/2/132

Xu, S., Jura, M., Koester, D., Klein, B., & Zuckerman, B. 2014, Astrophysical Journal, 783, 79, doi: 10.1088/0004-637X/783/2/79

Xu, S., Zuckerman, B., Dufour, P., et al. 2017, Astrophysical Journal, Letters, 836, L7, doi: 10.3847/2041-8213/836/1/L7

Young, E. D., Shahar, A., & Schlichting, H. E. 2023, Nature, 616, 306, doi: 10.1038/s41586-023-05823-0

Zahnle, K., Arndt, N., Cockell, C., et al. 2007, Space Science Reviews, 129, 35, doi: 10.1007/s11214-007-9225-z

Zahnle, K., Pollack, J. B., Grinspoon, D., & Dones, L. 1992, Icarus, 95, 1, doi: 10.1016/0019-1035(92)90187-C

Zahnle, K. J., Kasting, J. F., & Pollack, J. B. 1988, Icarus, 74, 62, doi: 10.1016/0019-1035(88)90031-0

Zel'dovich, Y. B., & Raizer, Y. P. 1967, Physics of shock waves and high-temperature hydrodynamic phenomena (New York: Academic Press)

Zhang, Y., Liu, S.-F., & Lin, D. N. C. 2021, Astrophysical Journal, 915, 91, doi: 10.3847/1538-4357/ac00ae

Zuckerman, B., Koester, D., Dufour, P., et al. 2011, Astrophysical Journal, 739, 101, doi: 10.1088/0004-637X/739/2/101

Zuckerman, B., Melis, C., Klein, B., Koester, D., & Jura, M. 2010, Astrophysical Journal, 722, 725, doi: 10.1088/0004-637X/722/1/725